SOLAR ENERGY POTENTIAL ASSESSMENT ON FAÇADES USING GEO-REFERENCED DIGITAL ELEVATION MODELS

Naveed ur Rehman

A thesis submitted to

Auckland University of Technology

in fulfilment of the requirements for the degree of

Doctor of Philosophy (PhD)

2020

School of Engineering, Computer and Mathematical Sciences

*Dedicated to my late father, **Attiq ur Rehman**, who unfortunately didn't stay in this world long enough to see his son become a doctor.*

ATTESTATION OF AUTHORSHIP

I hereby declare that this submission is my own work and that, to the best of my knowledge and belief, it contains no material previously published or written by another person nor material which to a substantial extent has been accepted for the qualification of any other degree or diploma of a university or other institution of higher learning.

Naveed ur Rehman
December, 2020

ABSTRACT

In modern city centres, which are comprised of tall buildings with limited rooftop space, installing solar energy technologies on the facades can effectively respond to the current barriers to their deployment on rooftops. However, since there is a dearth of efficient façade solar potential assessment models, feasibility analysis of such projects within a reasonable computation time has become a major challenge.

Area-based geographic solar potential assessment models are commonly employed in such environments. They use Digital Elevation Models (DEM) that contain the precise geo-referenced elevation. A comprehensive literature review has shown that these models use an approach that first requires disintegration of the façades into a large number of virtual surfaces. Then, each of these surfaces is analyzed, involving a large amount of computation time. Also, these models do not use skymaps (pre-processed solar radiation data) and the management of computational processes together. These two approaches combined were found to be very useful in reducing the analysis time in models for rooftop solar potential assessment.

This research gap in the literature indicated a need to develop a façade solar potential assessment model that completely avoids façade disintegration and incorporates skymaps and management of computational processes. Hence, this research focused on developing such a novel model and comparing its performance with the existing model.

For the purpose, the proposed model was broken down into four sub-models. The first was the discretization-independent scanning algorithm, which takes into account the DEM and the sun position and provides details of shadows on the facades. The results from this sub-model were compared with results obtained from a 3D geometric model developed in the Google SketchUp program and were found to be in good agreement with each other. Then, these results were fed into

the other three sub-models, which evaluated the beam, diffuse and anisotropic diffuse solar potential, respectively.

On analyzing a hypothetical layout to yield results at various levels of detail, the performance of the developed model in terms of accuracy and speed was found to be far better than the existing model. Also, incorporation of scalable architecture using multi-processing and cloud-computing drastically improved the speed. The results showed very close agreement when the AUT city campus, 80,000 m^2 in area, was analysed. The use of the proposed model to identify suitable locations for installing solar energy technologies on the facades of AUT buildings was also presented.

In summary, the proposed model has shown remarkable performance in terms of speed when compared with the conventional model. With the help of this model, solar potential assessments for façades can be performed at much faster speeds than existing models.

ACKNOWLEDGEMENTS

All praise to the **Almighty Allah**, the most beneficent and the most merciful, who granted me the strength and ability to achieve this task.

This thesis would not have been possible without the generous support of the wonderful people around me, particularly the help, support and patience of my Supervisor **Dr. Roy Nates** and **Dr. Tim Anderson** throughout these four years. The knowledge, skills and encouragement I have received from both supervisors have been of enormous value and I attribute the completion of my thesis to their influence.

I extend my gratitude to the **Auckland University of Technology (AUT)** and the **School of Engineering, Computer and Mathematical Sciences** for providing me with the comfortable working space and facilities to conduct this research. I would also like to thank the **Southern Institute of Technology (SIT)**, which I recently joined as a full-time Engineering Tutor, for providing me the necessary resources while I was wrapping up my thesis and for funding my trip to Auckland for my final Doctoral oral examination.

I am also very thankful to my research colleagues **Dr. Uzair Riazuddin**, **Dr. Sulaiman**, **Dr. Asif** and **Dr. Mehardad** for their valuable suggestions throughout the research. I would like to thank to my mother, **Surriya Parveen Attiq**, and my brother **Naeem ur Rehman**, who always supported and encouraged me during my difficult times. To **Adnan** and **Salman**, best friends forever, I say thank you for keeping my spirits high through it all.

Finally, my heartfelt thanks to my wife **Aisha Naveed** and my children, **Aliza Naveed** and **Muhammad Ahmad Naveed**, for patiently putting up with me during the hardship of these four years. I could not have done it without them.

LIST OF CONFERENCES

1. Naveed ur Rehman, Timothy Anderson, Roy Nates: Diffuse Solar Potential of Facades in an Urban Context under Different Sky Conditions. 2018 Asia-Pacific Solar Research Conference, Sydney, Australia; 12/2018
2. Naveed ur Rehman, Timothy Anderson, Roy Nates: Solar Potential Assessment of Facades in an Urban Context: An Algorithm for 2.5D Digital Surface Models. 2017 Asia-Pacific Solar Research Conference, Melbourne, Australia; 12/2017
3. Naveed ur Rehman, Timothy Anderson, Roy Nates: Solar Potential Assessment of Facades in an Urban Context: An Algorithm for 1.5D Digital Surface Models. 2017 Asia-Pacific Solar Research Conference, Melbourne, Australia; 11/2016

TABLE OF CONTENTS

LIST OF TABLES

LIST OF FIGURES

GLOSSARY

Incidence angle (degrees) is the angle between the direction of the beam radiation and the normal to the receiving surface.

Irradiance (W/m^2) is the rate of solar energy received per unit area of receiving surface. It can also be defined as the radiant flux received by a surface per unit area.

Irradiation (J/m^2) is the amount of solar energy received per unit area of receiving surface. It depends upon the time span over which the irradiances were summed up.

Radiance ($W/m^2.sr$) can be defined as the rate of solar energy received per unit area of receiving surface, originating from a single solid angle.

Radiant energy (J) is the energy of electromagnetic radiation.

Radiant flux (W) is the radiant energy emitted, reflected, transmitted or received, per unit time.

NOMENCLATURE

Abbreviations

BRT	Backward Ray Tracing
DEM	Digital Elevation Model
DSF	Diffuse Sky Factor
DSM	Digital Surface Model
DTM	Digital Terrain Model
FRT	Forward Ray Tracing
LOS	Line of Scan
SVF	Sky View Factor

Operators

∧	Minimum operator
∨	Maximum operator
"."	Vector dot product

Symbols

A	m^2	Area of radiation receiving surface
A_l	m^2	Lit area of radiation receiving surface
A_s	m^2	Area of shadow on radiation receiving surface
A_{sp}	m^2	Area of sky behind the panel in Siraki and Pillay's sky view factor model.
DSF_{aniso}	-	Diffuse Sky Factor for anisotropic sky
DSF_{iso}	-	Diffuse Sky Factor for isotropic sky
d	m	Distance between two features in 1.5D DEM
$\hat{F}$	-	Unit vector of normal to the façade
f_{BH}	-	Factor considered by Brunger and Hooper model
H	m	Height of façade receiving shadow in benchmark model
H_b	kJ	Radiant beam energy of a façade stripe
$H_{d,iso}$	kJ	Radiant isotropic diffuse energy of a façade stripe
H_o	m	Height of façade casting shadow in benchmark model
h	m	Height of a façade stripe
h_i	m	Height of the i^{th} feature in 1.5D DEM
I	W	Radiant flux
I''	W/m^2	Radiance
$\hat{I}_b$	-	Unit vector of the beam
I_b	kJ/hr	Beam radiant flux
I_b''	$kJ/hr.m^2$	Theoretical beam solar irradiance
$I_{b,hor}''$	$kJ/hr.m^2$	Theoretical beam solar irradiance on horizontal surface
$I_{b,tilt}''$	$kJ/hr.m^2$	Geometric beam solar irradiance on tilted surface
$I_{d\ q}''$	W/m^2	Diffuse irradiance approaching from q^{th} sky element in benchmark model

I'_{d_q}	Watt	Fraction of diffuse radiant flux from qth sky element in benchmark model
$I_{d,aniso}$	kJ/hr	Anisotropic diffuse radiant flux
$I_{d,iso}$	kJ/hr	Isotropic diffuse radiant flux
$I'_{d,iso}$	kJ/hr	Fraction of diffuse radiant flux
I''_d	kJ/hr.m^2	Theoretical diffuse solar irradiance
$I''_{d,hor}$	kJ/hr.m^2	Theoretical diffuse solar irradiance on horizontal surface
$I''_{d,tilt}$	kJ/hr.m^2	Geometric diffuse solar irradiance on tilted surface
i	-	Numberth of feature in 1.5D DEM
i_o	-	Total number of features in 1.5D DEM
j	-	Numberth of LOS in 2.5D DEM
j_o	-	Total number of LOS in a 2.5D DEM
k	-	Solar diffuse fraction
k_t	-	Atmospheric clearness index
L	m	Length of façade receiving shadow in benchmark model
L_o	m	Length of façade casting shadow in benchmark model
l	m	Total height of the façade stripe
l_b	m	Lit height of a stripe (when analyzing beam radiation)
l_d	m	Lit height of a stripe (when analyzing diffuse radiation)
l_i	m	Lit height of the ith feature in 1.5D DEM
M		Current number of multi-process in operation
M_{max}		Maximum permissible number of multi-process
$\widehat{N}$	-	Unit vectors of the surface normal
n	-	Number of elements in sky
P	-	Number of sections in a decomposed stripe
p	-	Numberth of section in a decomposed stripe

Q	-	Total number of sky elements
q	-	Numberth of sky element
R	W/m^2.sr	Radiance approaching from sky element
R_{aniso}	kJ/hr.m^2.sr	Radiance in an anisotropic radiant sky
R_{iso}	kJ/hr.m^2.sr	Radiance in an isotropically radiant sky
s_i	m	Shadow height of the ith feature in 1.5D DEM
t_i	m	Terrain height of the ith feature in 1.5D DTM
u	m	Elevation of a hyperpoint
v	-	Binary function
W	m	Width of the façade cell in DEM
$X \times Y$	-	Size of 2.5D DEM matrix
(x, y)	-	Spatial location of a cell in x-y plane in DEM
(x_o, y_o)	-	Coordinates of façade corner casting shadow in benchmark model
(x', y')	-	Coordinates of shadow corner in benchmark model
Z	m	Distance between the two façades in benchmark model
α_b	degree	Altitude angle of beam or sun
α_e	degree	Altitude angle of sky element
$\Delta\alpha_e$	degree	Altitudinal dimensions of a single sky element at the base of the vault
α_G	degree	Altitude angle of an illumination source or ray
β	degree	Tilt angle of receiving surface
γ	degree	Azimuth angle of receiving surface
γ_b	degree	Azimuth angle of beam or sun
γ_{bN}	degree	Azimuthal position of the sun, measured counter-clockwise from the x-axis
γ_e	degree	Azimuth angle of sky element

$\Delta\gamma_e$	degree	Azimuthal dimensions of a single sky element at the base of the vault
γ_G	degree	Azimuth angle of an illumination source or ray
γ_N	degree	Angle of true north measured counter-clockwise from the x-axis
δ_b	-	Incidence effect factor when analyzing beam radiation
δ_d	-	incidence effect factor when analyzing diffuse radiation
ϵ_e	degree	Complementary angle of sky element's altitude angle
θ	degree	Incidence angle
θ_b	degree	Incidence angle (when analyzing beam radiation)
θ_e	degree	Incidence angle (when analyzing diffuse radiation)
θ_Z	degree	Sun's zenith angle (or complementary angle of sun's altitude angle)
ρ_H	points/meter	Hyperpoint density
ρ_S	degree	Sky discretization resolution
τ	hr	Hour of the typical year
ψ	degree	Angle between the sky element and sun
ω_e	Steradian	Solid angle associated with the sky element

1

INTRODUCTION

1.1 Overview

Energy is crucial in sustaining human life; it is an essential part of the economic and social fabric of any society. Growth in the human population, along with urbanization and an overall rise in living standards, has drastically increased energy demands in recent years. For a long time, fossil fuels (coal, oil and gas) have played a dominant role in the global energy system. However, growing concern over the depletion of these resources and their adverse effects on the global climate has led many countries to try to mitigate their use by switching to renewable and clean energy sources. Among the different renewable energy-based solutions, including hydro, tidal, wind and biomass, solar energy has been found to be a very promising alternative in providing both heat (thermal energy) and electricity, especially in modern urban centres, where most energy is consumed. Additionally, the feasibility of owning such systems has been significantly improved due to technological advancements that have led to a substantial drop in the price of solar energy systems. Therefore, large-scale deployment of building integrated solar energy systems at both the residential and commercial scales is expected in the near future.

1.2 Solar Energy

Solar energy is the largest inexhaustible source of clean energy in the world. It is estimated that the earth receives nearly 4 million EJ of solar energy annually, of which 50,000 EJ (1.39×10^{16} kWhr) is claimed to be harvestable [1]. This is 350 times more than the world's projected net electricity generation in 2040 [2, 3]. For the last couple of decades, considerable research has been done to develop solar energy harvesting and utilization. A primary goal of this research has always been the transformation of solar energy into more concentrated and useful forms of energy, such as heat and electricity, so that the issues associated with energy security, sustainability, climate change and clean transportation can be alleviated.

Solar energy harvesting technologies can be classified broadly into passive and active technologies [4] as shown in Figure 1. The former involves the accumulation and direct use of solar energy, without converting it into any other form [5]. The applications of passive technologies range from space heating/cooling [6] to providing efficient daytime lighting [7]. In contrast, the active technologies involve the collection and conversion of solar energy by means of mechanical and/or electrical equipment. Examples include solar photovoltaic (PV), which directly converts solar energy into electric energy by means of semiconductors [8]. The prediction is that solar PV systems will dominate renewable capacity growth within the next six years [9]. Also, of the 575 GW of expected new solar-based capacity that will become operational over that period, 45% of it will be installed on consumers' sites as decentralized (or distributed) systems. Other examples of active solar technologies are the solar thermal (ST) systems that harness the heat from solar energy so it can be used in residential, commercial and industrial applications such as cooking, heating, cooling, drying, desalination and power generation [10, 11, 12]. The devices include flat-plate collectors, parabolic and paraboloid concentrators, and power towers etc. The accumulated in-operation solar thermal capacity by the end of 2017 was 472 GWth, which is more than seven times what it was in 2000.

Also, the annual thermal energy yield in 2017 was 388 TWh, which correlates to savings of 41.7 Mton of oil [13].

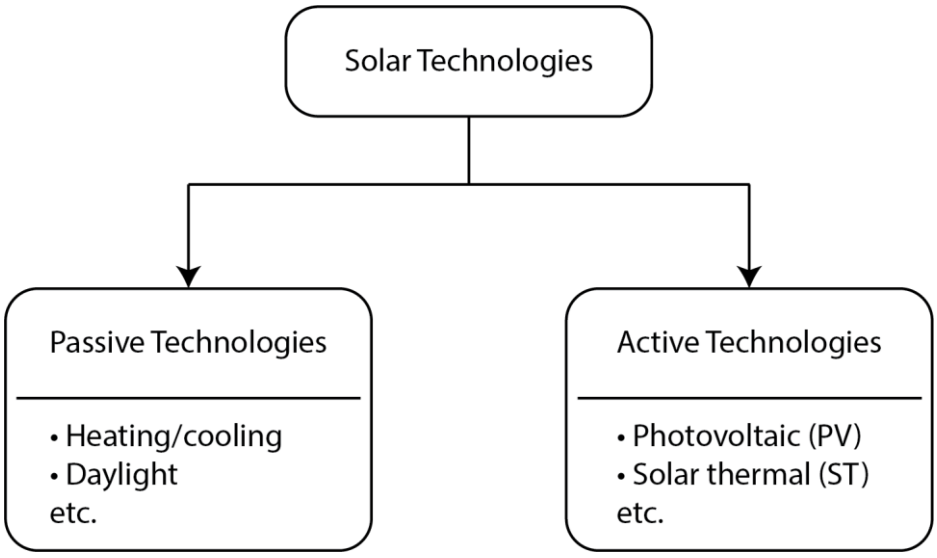

Figure 1: Types of solar energy harvesting technologies

1.3 Solar Potential Assessment

1.3.1 Solar Potential

It is essential to realise that harnessing solar energy effectively requires detailed knowledge about the accessibility of solar radiation at the region of interest – *Solar potential* is the term applied. Hoogwijk [14] provided a well-founded hierarchical methodology for describing the potential of several renewable energy sources, as shown in Figure 2. For solar energy, this hierarchy comprises five stages: (i) theoretical potential, which is the theoretical limit of terrestrial solar energy reaching the earth; (ii) geographic potential, which is the potential, reduced to incorporate only the energy-receiving areas that are considered available and suitable for conversion; (iii) technical potential, which is the geographic potential reduced due to the inefficiency of the conversion systems; (iv) economic potential, which is the amount of technical potential derived at cost levels that are

competitive with alternative energy applications; and (v) implementation potential, which is the amount of technical potential that is implemented in the energy system. It depends upon subsidies and policies as well as social barriers.

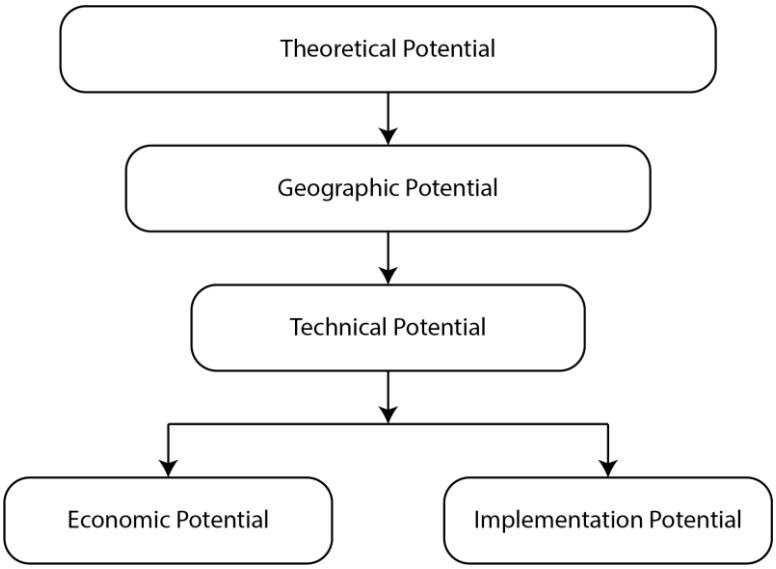

Figure 2: Stages of solar potentials [14]

The theoretical potential of solar energy reaching the ground in earth's atmosphere has two components; beam (or direct) radiation and diffuse radiation, as illustrated in Figure 3. Beam radiation is received directly from the sun without being scattered by the atmosphere [15]. In contrast, diffuse radiation reaches the surface through scattering, reflection from ground and other urban features, and absorption by atmospheric constituents [16]. Diffuse radiation further consists of the sky, circumsolar and horizon-brightening radiation subcomponents. If the sky is isotropic, diffuse radiation is received uniformly from the entire celestial sky vault [17]; the circumsolar component is received from onward dispersion of solar radiation and concentrated in the section of the sky around the sun [18]; and the horizon brightening component is concentrated near the horizon and is most obvious in clear skies [19]. The latter two subcomponents are considered only when the sky is assumed anisotropic which is a more realistic assumption [20]. The sum of the beam and diffuse solar radiation received at a horizontal surface is known as *global solar radiation*.

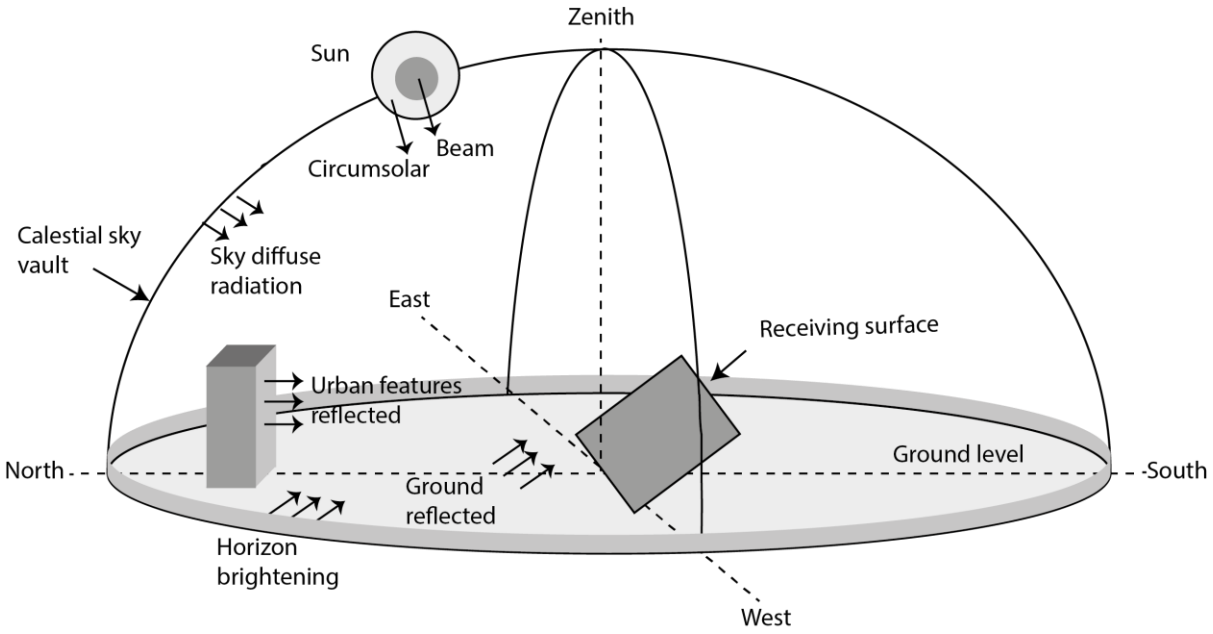

Figure 3: The composition of solar radiation

Two approaches have been identified for estimating the theoretical solar potential [21]. The first approach is the radiative transfer method, which estimates the incoming radiation based on its physical interactions with atmospheric constituents [22]. These methods incorporate the effects of air molecules, the amount of water vapour, cloud cover, optical depth, ozone column, and aerosol optical depth [23, 24]. These methods are generally considered complex and data-intensive and hence, there are several limitations to their practical use [25]. The other approach is a set of empirical methods based on statistical regression techniques [26]. There are several linear [27], quadratic [28, 29], cubic [30, 31] and exponential models [32] that can correlate the incoming radiation with the clearness index (the ratio of global radiation to extra-terrestrial radiation). The advanced models use sunshine duration [33], precipitation [34], air temperature [35, 36] and relative humidity [37]. As long-term meteorological data are often available, a common approach is to either select some suitable model for the desired location [38, 39] or to use geolocation-tied databases and visual maps of solar radiation [40, 41, 42, 43, 44, 45, 46, 47, 48].

1.3.2 Geographic Solar Potential

As described earlier, the geographic potential is less than the theoretical potential due to the limited number of energy-receiving areas that are suitable for the conversion, as illustrated in Figure 4. When designing both active and passive solar energy systems, evaluating this potential is crucial as it provides the radiation data for the site in appropriate spatial and temporal resolutions. To obtain the geographic potential, the orientation of the receiving surfaces and the effects of surrounding elevations (e.g. natural features and urban architectures) are the two key aspects that must be considered.

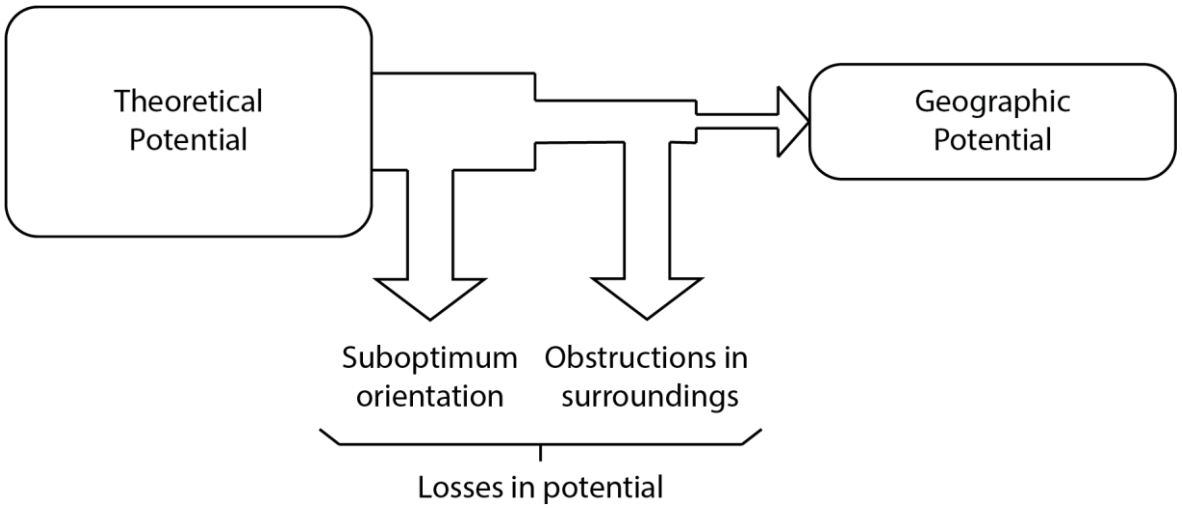

Figure 4: Reduction of theoretical potential to geographic potential

In an unobstructed sky, modifying the orientation from horizontal (i.e. tilting and rotating the surface) alters the magnitude of the received beam and diffuse radiation due to the change in the apparent area of the receiving surface. These effects have been extensively discussed in the literature [49]. In fact, the basic aim of these studies is to optimize the orientation of stationary receiving surfaces by the use of prudent algorithms [50, 51, 52, 53]. Tilting the surface adds another component to the incoming radiation, commonly known as reflected radiation [54]. In the situation where there are no other objects around the surface, this reflected radiation comes only from the ground and therefore depends

upon the reflectivity of the ground. The sum of the beam, diffuse and reflected radiation on the surface is known as the *total solar radiation*.

When the entire view of the surroundings is assumed to be unobstructed, there are several mathematical models that can aid in transforming the theoretical potential to the geographic potential of the inclined surfaces. For beam radiation, the calculations are straightforward and have been described in many publications [55, 56, 57]. The most widely employed geometrical model is the one in which the beam component on a tilted surface ($I''_{b,tilt}$) can be obtained by considering the two incidence angles, as shown in Figure 5. The first, θ_Z (also known as zenith angle), is measured when the surface is lying horizontally. The other, θ_b, is the angle when the surface is inclined (e.g. at an angle β). Then, the beam potential on an inclined surface can be obtained by multiplying the theoretical potential on the horizontal ($I''_{b,hor}$) by the ratio between the cosine of θ_Z and cosine of θ_b, as given in Eq. (1) [15].

$$I''_{b,tilt} = I''_{b,hor}\left(\frac{\cos\theta_z}{\cos\theta_b}\right) \qquad \textbf{(1)}$$

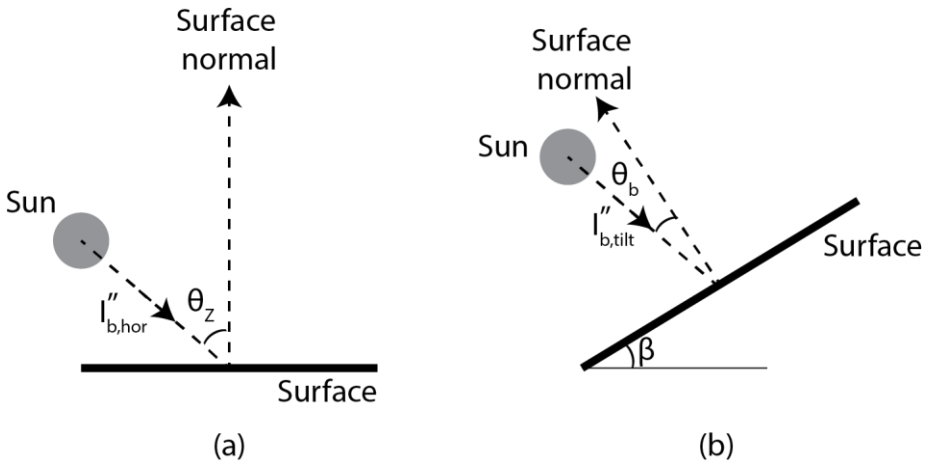

Figure 5: Incidence angles for horizontal and inclined surfaces

The estimation of diffuse potential on an inclined surface is treated differently to the beam potential. This is because, unlike beam radiation, diffuse radiation comes from all points of the sky. Several models have been proposed in the literature for obtaining this potential. Depending upon the assumptions about the radiating sky, these models have been classified into two groups.

In the first group, the sky is assumed isotropic; i.e., the circumsolar and horizon brightening subcomponents are ignored. These analytical models require multiplying the horizontal diffuse radiation by a factor, known as *Sky View Factor* (SVF), which is generally described as the fraction of sky that can be "seen" from a point on receiver, given in Eq. (2). For example, the SVF of a point on an unshaded horizontal surface would be 100% and for a vertical surface, it would be 50%, as shown in Figure 6.

$$I''_{d,tilt} = I''_{d,hor}\, SVF \qquad \textbf{(2)}$$

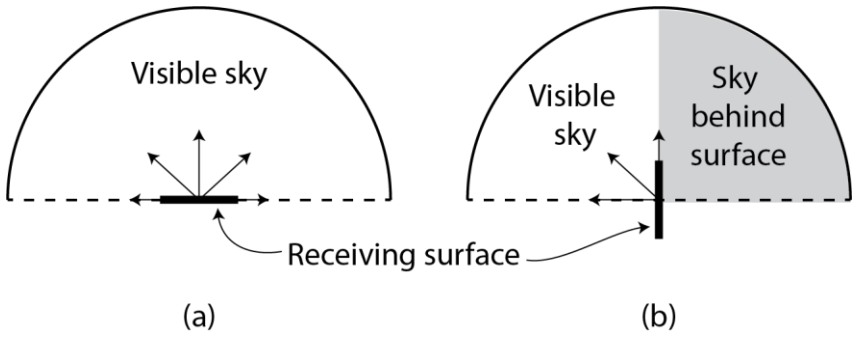

Figure 6: SVF for (a) horizontal surface (b) vertical surface

As the diffuse isotropic radiation doesn't depend on the position of the sun in the sky, these models depend only on the tilt angle of the surface. The model proposed by Liu-Jordan [58] is so far the most extensively used. The discussion on the different existing SVF models is presented in Table 1.

Table 1: Sky View Factor (SVF) models

SVF Models	Mathematical Relation	Discussion
Liu-Jordan model [58]	$SVF = \frac{1 + \cos\beta}{2}$	This is so far the most extensively used model among others.
Tian model [55]	$SVF = \frac{180° - \beta}{180°}$	This model has been appreciated as a more appropriate model in terms of geometrical aspects [59]. However, full investigation of the concept has found this model inconsistent with the fundamental theory of radiation [60].
Siraki and Pillay model [61]	$SVF = 1 - \frac{1}{\pi^2} A_{sp}$	Here, A_{sp} (m^2) is the area of sky behind the panel. This was an attempt to improve the Liu-Jordan model by utilizing the technique based on dividing the sky into number of patches so that it could be used under obstructed sky conditions as well. However, the base model they presented for the unobstructed sky conditions was found to ignore a couple of underlying concepts [60].
Badescu model [62]	$SVF = \frac{3 + \cos 2\beta}{4}$	This model has been used in numerous studies [63, 64, 65, 66] and has been discussed in several reviews [67, 68, 69]. Some of the recent references include [70, 71, 49]. However, an in-depth analysis of this model presented in [72] and [73] indicates that it is

		mathematically incorrect and may lead to significant errors. After removing the error, the results were equal to those from the Liu-Jordan model [58].
Rakovec and Zaksek model [59]	$SVF = \frac{1 + \cos^2 \beta}{2}$	This is as same as the Badescu model [62] but with different (though equivalent) trigonometric identities.

The second group of models used for estimating the diffuse potential on inclined surfaces assume the radiant nature of the sky is anisotropic. Some of these models consider only the circumsolar subcomponent together with the isotropic subcomponent [74], while others consider horizon brightening together with the other two subcomponents. The models of Hay [75], Hay and Davies [76], HDKR [77], Perez [78] and Brunger and Hooper [79] are among those commonly used analytical models in this group.

The obvious advantage of all the analytical models discussed so far is their ease of use; however, in environments where the sky is partially obscured, questions arise about their applicability. The elevations around the surface (e.g. hills, trees and buildings) affect the geographic solar potential in several ways. These elevations may obscure the sun from the surface and thus reduce the access of beam and circumsolar radiation. They may also obstruct some part of the sky, hence diminishing the available diffuse radiation. They may also act as reflectors, eventually increasing the reception of reflected radiation.

This limitation has led to the development of methods that can work in built environments. Fu and Rich [80] categorized such models into two groups: (i) point-specific; and (ii) area-based. Models in the former group, based upon the surface orientation, can assess the potential of a specific point only.

The local effects of topography are generally accounted by the mathematical relations [81, 82, 83], visual estimations [84, 85], or fisheye photographs [86, 87, 88]. The models in the latter group are able to compute potential over large areas, calculating surface orientation and horizon and shadow effects using geographic-information systems (GIS) [89, 90, 91, 92, 93] and satellite imagery [94, 95].

The advanced form of area-based models considers Digital Elevation Models (DEM) that contain the precise geo-referenced elevation. The two types of DEM include the Digital Terrain Model (DTM), which describes the elevation of terrain measured from some fixed datum, and the Digital Surface Model (DSM), which describes the height of the urban fabric measured from the terrain. The dataset in the DEM contains the single height value (in the z direction) for every discrete x-y point (known as *cells*) on the x-y plane, as illustrated in Figure 7. Since this representation of the data cannot describe the details of vertical terrain or urban features, they are commonly known as "2.5D" models rather than truly "3D" models [96] [97]. It can be generated via methods such as photogrammetry, Light Detection and Ranging (LiDAR) and Interferometric Synthetic Aperture Radar (IfSAR) [98, 99].

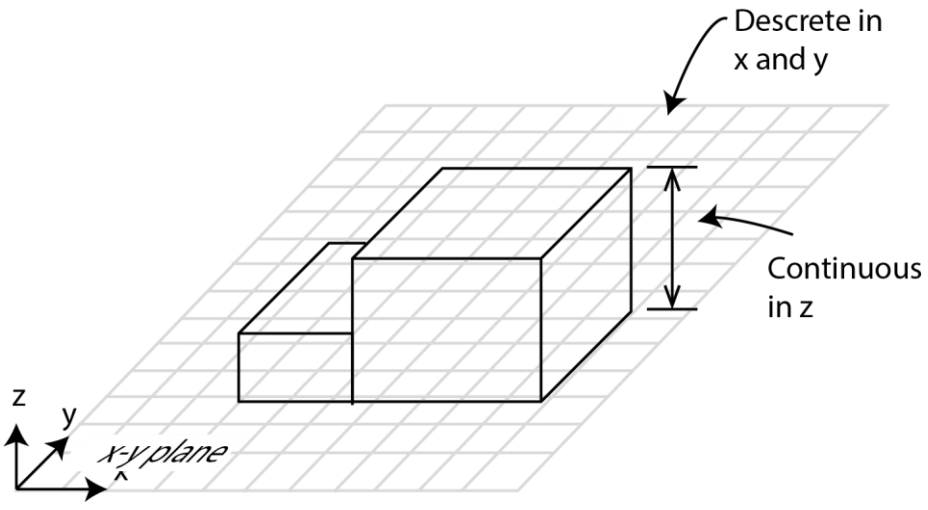

Figure 7: Illustration of 2.5D DEM

The first model that showed the ability to assess solar potential using a DTM was SOLARFLUX, proposed by Hetrick et al. [89]. It was implemented in ARC/INFO and GRID-GIS as an Arc Macro

language (AML) program. The model calculates the beam and diffuse radiation, duration of beam sunlight and SVF. For each interval of time, the model calculates the position of the sun in the sky and the shadow on every cell, using the HILLSHADE function. The main limitation of this function is that it only considers the elevations of neighbouring cells and thus does not account for the shadows cast from elevated points that are more than a single cell away.

Fu and Rich [80] attempted to mitigate the problems associated with the HILLSHED function by introducing the concept of *viewshed*, and proposed the SolarAnalyst program as an extension, developed for the ArcGIS platform. Viewsheds provide a representation of the angular distribution of sky obstructions, calculated for each cell in the DEM. The algorithm for calculating the viewsheds was based on searching to the edge of the DEM in the specified set of directions around each cell to find the maximum angle of sky obstruction. These angles were compared with the sun's altitude angles to determine whether a cell was in shadow or not. The number of scanning directions was proportional to the accuracy of the model but for greater accuracy, more computation time was required. To mitigate this issue, they pre-processed beam solar radiation data into *skymaps*, in which the number of scans were reduced, from each sun position in the year to a few patches in the sky that represented the accumulated beam radiation coming from them throughout the year.

The r.sun, proposed by Hofierka and Suri [100], is another model that evaluates solar potential at geographic scales by using the DTM. It is implemented in the GRASS GIS program and an attempt was made to analyse the potential of very large geographic areas, covering several different climatic zones, by setting the percentage of beam and diffuse irradiation as spatially resolved data rather than a fixed value, as was done in SOLARFLUX and SolarAnalyst. Since the viewshed algorithm used was the same as discussed above and the model was not capable of using skymaps, it showed no improvement in computation speed. It was also limited to assessing the potential of only a single hour or day.

1.3.3 Urban Solar Potential

Improving living conditions in the world's overcrowded cities has become a major concern. Currently, nearly 50% of the world's population lives in urban areas and the forecast is that almost all population growth over the next several decades will take place in such areas [101]. Therefore, high-quality energy management in urban areas is of the utmost importance and the reliable supply of the energy to the residential and commercial buildings has been highlighted as a key aspect in this regard [102]. Among the other renewable energy technologies, solar energy has been underlined as the main energy source that can be used in buildings to improve their overall energy sustainability [103].

Nowadays, modern urban areas are generally comprised of high-rise buildings and skyscrapers as such constructions have become a more common choice due to concerns about land costs and available space, along with architectural evolution, advancement in construction technologies and modernism [104]. To improve the overall energy efficiency of these buildings, roofs, facades, balconies and awnings have been identified as excellent locations for the mounting of solar energy systems [105]. These systems can partially, if not fully, offset the overall thermal requirements [106], including the heating/cooling and hot water [107] for the occupants. Buildings can potentially reach near-zero energy status with recent research and development in smart grid systems and advancement in energy policies related to net-metering [108] and thermal energy storage systems [109, 110].

However, the assessment of solar potential in such densely built-up environments is complicated, as dwellings and other buildings receive very uneven solar radiation compared to non-urban areas. This irregularity is mainly due to the dynamic mutual shading and sky blocking of urban features. Therefore, urban potential assessment requires carefully designed methods and models that are strongly coupled with the complex problems of the urban environment [111].

There are several models that can perform point-specific urban solar potential assessment. A typical procedure involves determining the position angles of exposed corners and edges of all urban features

around the installation site as a first step. These are expressed in terms of azimuthal (horizontal) and altitude (vertical) angles, viewed from a chosen point. Several tools can be used for this kind of survey, including manual and digital inclinometers [112], Solar Pathfinder [113, 114], image processing-based models, software [115, 116] and mobile-camera applications [117, 118]. In the second step, these position angles are projected on to a sun-path diagram (or solar positioning curve) [119], forming polygons overlaid on sun trajectories and sky, as shown in Figure 8. These diagrams or their numerical equivalents are used as an input to the models.

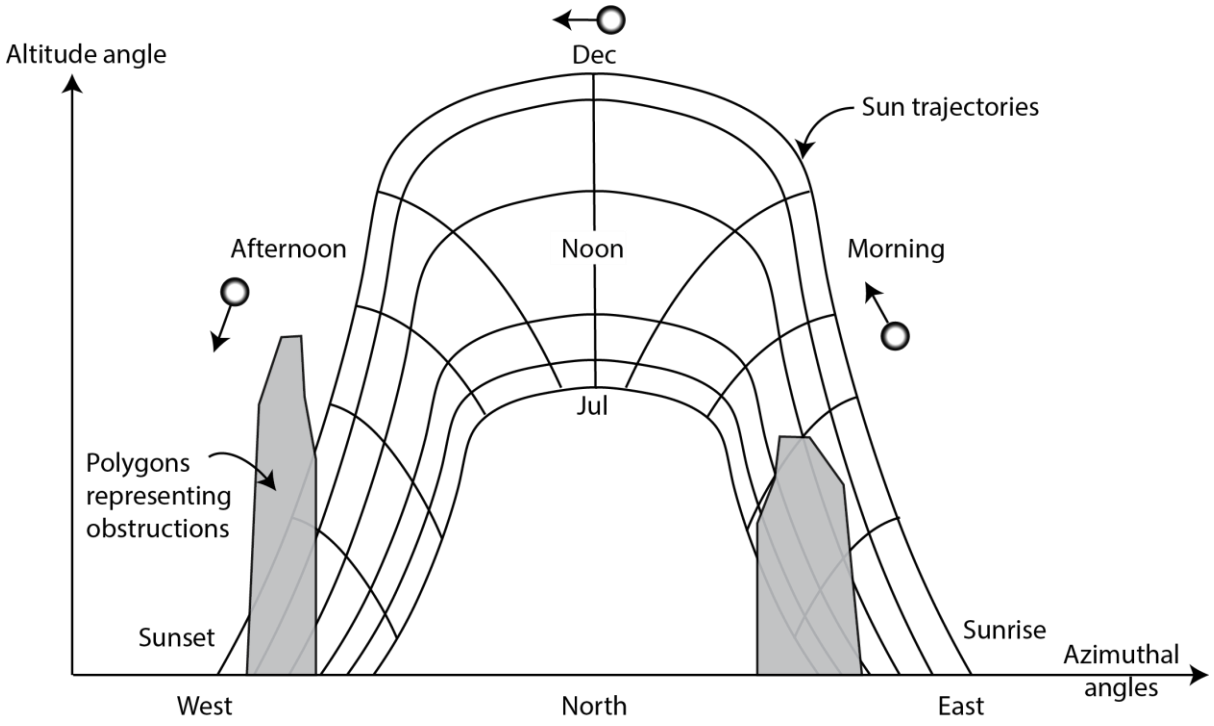

Figure 8: Illustration of a sun-path diagram with the obstructions overlaid as polygons (somewhere in southern hemisphere)

The beam component in these models is dealt with in a very similar manner to the geometrical model discussed previously. However, the hourly value is multiplied by a shading factor, which correlates with the view of the sun from that point. Therefore, in the sun-path diagrams, if the polygons overlay the position of sun during that hour, the beam radiation will be totally or partially reduced, and the potential losses can be estimated [120, 121].

In contrast, the models for estimating the point-specific diffuse potential under isotropic sky work in a different way compared to the tilt-angle dependent analytical models that were relying only on SVF, as discussed earlier. Some analytical models exist in the literature [122, 123, 124], but their applications are limited to less complex surroundings only. The modern form of these models [125, 126, 127] is based on a *sky discretization technique*, in which the sky vault around the receiving surface (or point) is divided into number of radiating elements, as shown in Figure 9. One widely employed discretization method was proposed by Tregenza and Sharples [128]. In this approach, the vault was divided into 145 elements to save computational time. However, such an approach cannot give accurate results in all situations because of the large size and limited number of elements [129]. More recently, Siraki and Pillay [61] used a discretization scheme where the vault was divided into 324 elements with a constant angular area of $10° \times 5°$. Initially, the discretised hemispherical sky vault was projected onto a two-dimensional plane. Then, the urban features were plotted onto this plane. Finally, SVF was calculated by knowing the number of elements that were blocked by these features, out of the total number of elements. The two major limitations associated with this model were: first, it was only able to determine the SVF for surfaces facing true south; and second, it ignored the effects of incidence angles, yielding overestimated results. To overcome these limitations, Rehman and Siddiqui [130] presented a model that considers the distinct directions of radiances coming from all over the celestial sky vault. The vault was subdivided into a fine mesh of 32k elements having angular areas of $1° \times 1°$. The effect was quantified based upon the incidence angle and the dilation of elements' areas (which is the expansion of an element's area, from the zenith to the base of the sky vault). For an obstacle-free site, comparison shows that the proposed model was in excellent agreement with Liu-Jordan [58] for all the values of tilt angles. Additionally, the model provided insight into the solar potential reaching the surface from different elements, which is useful in analysing sites with obstructed sky.

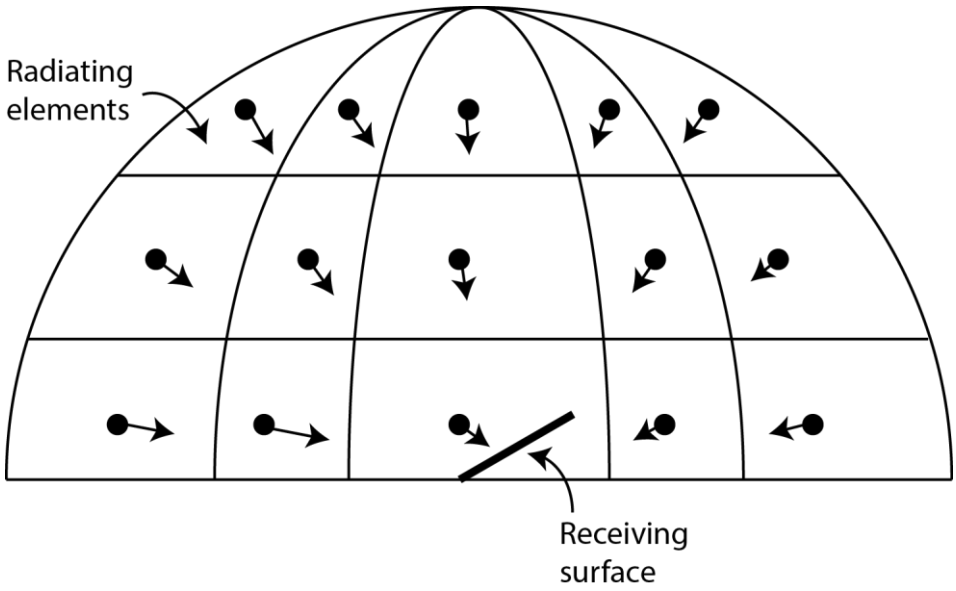

Figure 9: Illustration of a discretized sky vault around the surface for assessing the diffuse solar potential

On the other hand, the first area-based urban solar potential assessment model that used the DEM was proposed by Carneiro et al [131]. It assumed an anisotropic sky, as represented by Hay's model [75]. The codes were written in the MATLAB programming environment [132]. The facades were sliced into 3m heights and the viewsheds were calculated for every roof and façade cell. However the representation of data was limited, as the radiation values were averaged over the associated areas.

The v.sun [133] model was developed to process vector-based GIS data to analyse the solar potential on roofs and facades of buildings. For diffuse radiation, the anisotropic sky presented in [100] by the same authors was considered. The urban fabric was discretised into a large number of small 3D volumes. The shadowing effects of surrounding objects were considered using a unique vectoral shadowing algorithm that accounted for every 3D volume in the relief.

Tabik et al [134] demonstrated the combined use of skymaps and GPU-CPU heterogeneous parallel computing architecture for speeding up the calculations. The sky was assumed isotropic. However,

the proposed model is only able to assess the solar potential of rooftops (or near-horizontal surfaces), which is a major limitation.

The model presented by Jakubiec and Reinhart [135] uses a detailed Perez all-weather sky model [136] along with parameters to simulate the output of PV devices. It was an advancement on the v.sun model as the urban fabric was discretised into 2D simplified triangular surfaces rather than volumes. The calculation engine was based on RADIANCE/Daysim [137], which discretised the celestial sphere into 145 coarse elements, sighted from every point of the DEM.

The model named SOL, proposed by Redweik et al. [138], also demonstrated the ability to perform potential assessments of building surfaces. The facades were discretised into a mesh of the same resolution as the given DEM (i.e. 1m). An isotropic sky was assumed for evaluating the diffuse solar radiation. For this, the sky was discretised into 1081 equally spaced elements. The SVF was determined by counting the number of radiances reaching the cell, out of the total radiances. However, the incidence angles of the radiances with the receiving surfaces were ignored.

The SURFSUN3D model, proposed by Liang et al. [139] used the r.sun engine to calculate the potential of urban surfaces, which were pre-discretized into a mesh of 2D triangular network. For diffuse radiation, the sky was assumed isotropic and the model was implemented in GPU-based parallel computing architecture for faster results.

Lingfors et al. [140] presented a model that was capable of rooftop solar potential assessment only. It assumed an isotropic sky and demonstrated the efficient use of skymaps.

The model presented by Desthieux et al. [141] performed rooftop and façade solar potential assessment, considering various anisotropic sky models. However, the sky was discretized into 137 elements only and skymaps were not used at all. For faster processing, the codes were deployed in a high-processing cloud computing environment.

Oh and Park [142] proposed a model that used two different DEMs, one with a fine grid for near distances and the other with a coarse grid, subsampled from the actual DEM, for far distances. For diffuse radiation, an isotropic sky was assumed and skymaps were used for faster computation. However, the model can perform rooftop potential assessments only.

The model proposed by Kapoor and Garg [143] demonstrated the application of commercial high-speed cloud computing setup for assessing the rooftop solar potential of a given urban relief. The sky was assumed isotropic and no skymap was used.

1.3.4 Solar Potential of Façades

The traditional location for installing solar energy systems is rooftops. The idea developed from the underlying assumption that on a rooftop, solar collection devices can receive radiation from the entire radiating sky as well as from the sun at any time of the day. However, with tall skyscrapers and slender buildings, the problem arises of limited rooftop area, which is a significant constraint to the installation of solar energy systems.

Perhaps façades can be another potential location for the solar installations. With the advent of the solar architecture revolution, the facades are now designed for providing both passive and active solar energy to the building, including, but not limited to, providing hot water and absorption cooling, electricity generation and daylighting [144, 6].

In any high-rise building, the area covered by the façade may be several times larger than the rooftop area. However, not all façades of a building receive the same amount of solar radiation, for two main reasons: (i) the path of sun during the year (for example, sun remains toward the north in places located in the southern hemisphere); and (ii) the shadowing effects of neighbouring objects. Installing active solar energy systems (PV or ST) on façades involves several advantages and disadvantages when compared with rooftop installations, as elaborated in Table 2.

Table 2: Advantages and disadvantages of installing solar active systems on façades

	Advantages	Disadvantages
Maintenance [145]	Being vertical, the PV and ST systems may be less prone than roofs to accumulate snow, dirt, dust, leaves, pollen, and bird droppings, which result in power loss and damage to the health and life of the system.	Cleaning may be very difficult if the devices are not easily accessible; e.g., if they are installed away from the windows. This may add to the operating costs in terms of hiring professional cleaners.
Seasonal effects [146]	Due to the lower trajectory of the sun in winter, the performance of ST systems, e.g. for producing hot water, may be very good.	Due to the high trajectory of the sun in summer, the output from PV and ST systems may be considerably reduced. This may affect the performance of electric or heat-operated cooling systems.
Daily effects [147]	Solar system installations will produce more output during early and late hours of the day, especially in summer.	If the façade is not oriented properly, the installed solar system may lose the opportunity to generate maximum possible yield.

The models discussed in the previous section – including Carneiro et al [131], v.sun [133], Jakubiec and Reinhart [135], SOL [138], SURFSUN3D [139] and Desthieux et al [141] – have shown the potential to be used in assessment of façades.

1.4 Challenges in Façade Solar Potential Assessment

The DEMs of modern cities are larger and denser because of the increase in built-up areas. According to Tabik et al. [134], obtaining acceptable solar potential assessments within a reasonable computation time, using such DEMs, has become a major challenge.

The computation speed becomes more crucial when such assessments have to be done frequently. For example, Lobaccaro and Frontini [148] used a generative modeling approach to perform sustainable urban planning. The method required training of the algorithm, for which the solar potential assessment model must run several times. However, limitations in computer processing speed led to the choice of mono-parametric optimization. Similarly, Kämpf and Robinson [127] used evolutionary algorithms to optimize the building form for solar energy utilization. Achieving the results in a reasonable time without compromising excessively on accuracy was one of the difficulties encountered.

Probst and Roecker [149] found that a slow execution speed, which is one of the barriers to the adoption of Building Integrated Photovoltaic (BIPV) technologies [148], caused delays in the whole process of communicating the solar potential to stakeholders, and as a result, opportunities for promoting facade-integrated solar technologies to consumers, architects, engineers, auditors and building owners can be lost. Likewise, according to Koo et al. [149], the lack of such information affects regional energy policy making as well; for example, in terms of choosing ideal areas in the city for PV system installation, or establishing long-term energy supply and demand strategies. Moreover, Littlefair [150] and, more recently, Hachem et al. [111] note that there will be a high and frequent

demand for solar potential analysis in developing cityscapes because new buildings are able to harness solar energy more conveniently than existing buildings.

In mitigating this challenge at the level of modelling, two bottlenecks have been identified in recent studies. The first is the approach of *scanning*, which deals with computing the shadows and obscured portions of the sky. Freitas et al. [151] stressed that scanning is the most time-consuming part of the whole analysis and its optimization can improve overall performance. The second limitation relates to the *management of computational processes* in the existing models. Tabik et al. [134] emphasized that the implementation of existing models is not computationally scalable, as they have been developed to work in sequential environments. Hence, they take considerable time to process DEMs, even at low temporal resolutions. Therefore, if the computational processes involved are managed to work under a multi-processing architecture, the computation time can be greatly reduced.

A brief summary of the existing façade solar potential assessment models, showing how they treat the façades, and their capabilities and limitations, is provided in Table 3. It can be seen that no model exists that can perform the calculations without discretizing facades into cells, represented by either a 2D surface or a 3D volume. Oh and Park [142] highlighted this as a serious concern and concluded that since the scanning has to be performed for each discretized cell of the DEM in existing models, the computation time of these models massively depends upon the buildings' height and density in the area. Freitas et al. [151] reached similar conclusions and noted that in such models, if hourly values of radiation over an year had been used, the computation time would be in the order of several days. For mountainous terrains, Ruiz-Arias et al. [152] reported that increasing the resolution of the DEM from 0.01 cells/m^2 to 0.05 cells/m^2 on horizontal plane increased the computation time by 10 to 300 times in different models. However, no study quantified the relationship between the number of façade cells and the computation time. Also, no study included anisotropic sky, skymaps and management of the computational process.

Table 3: A brief summary of façade solar potential assessment models in terms of their façade treatment, capabilities and limitations

Work		Façade Treatment	Anisotropic Sky Assumption	Use of Skymap	Management of Computational Processes
Model	**Year**				
Carneiro et al [131]	2010	Facades are sliced at 3m.	✓	×	×
v.sun [133]	2012	All the urban volumes (including façades) are converted into 3D voxels of 2.5m each.	✓	×	×
Jakubiec and Reinhart [135]	2013	All surfaces (including façades) are converted into 2D triangulated surfaces.	✓	×	×
SOL [138]	2013	Facades are sliced at the resolution of the DEM. An example using 1m is shown.	×	×	×
SURFSUN3D [139]	2015	All surfaces (including façades) are converted into 2D triangulated surfaces.	×	×	✓
Desthieux et al [141]	2018	All surfaces (including façades) are converted into 2D irregular triangulated surfaces.	✓	×	✓

1.5 Research Question

From the literature review, it can be concluded that despite the work undertaken, there is still a gap in terms of researching and developing a façade solar potential assessment model that does not depend on discretizing the façades into cells. If such a model is developed, its performance can be compared with the existing models to see if it performs faster in complex urban reliefs. The developed model

should also be able to consider an anisotropic sky for more realistic results and be capable of using skymaps and optimizing through computational process management.

Therefore, the research question in this study was:

"How can we develop a façade solar potential assessment model that does not have façade discretization, uses skymaps, and has computational process management; and will such a model perform faster than existing models in densely built-up environments?"

2

DEVELOPMENT OF DISCRETIZATION-INDEPENDENT SCANNING ALGORITHM

2.1 Introduction

The solar energy, accumulated by a surface over the given span of time, depends upon the direction and magnitude of incident irradiation as well as the lit area of the receiving surface. In a situation where the surface is surrounded by the obstructions, the shadowing and sky blocking effects dynamically changes its lit area over the time. In the area-based geographic solar potential assessment models, the *scanning algorithm* is utilized to quantify the lit area of urban surfaces, when they are

provided with the information about the position of illumination source in sky and the details of the surrounding elevations in the form of DEM [80].

Freitas et al. [151] described that the existing scanning algorithms use the technique where the illumination source is sighted from the building surfaces. Such a technique is known as *Backward Ray-Tracing,* hereafter referred to as *BRT*. A typical BRT technique for the points on a rooftop has been well explained by Fu and Rich in [80]. It begins with the meshing of the available surface area into small cells, which in the case of 2.5D DEM, is already available for horizontal surfaces. From each of these cells, the surroundings (horizon) are searched in all directions to obtain information about the sky and sun path obstructions. BRT has shown good accuracy for assessing rooftops as the cells corresponds to the discrete (x, y) points in a DEM that has information about their absolute heights [138].

For the façades, the existing literature has suggested that a virtual mesh should be generated to divide a façade into a number of vertical cells, as discussed in the previous chapter (see the summary in Table 3). In this study, the centre points of these cells, from where the surroundings are searched, are termed as *hyperpoints* and the number of hyperpoints per unit height of façade is termed as *hyperpoint density*. The horizon searching in the BRT technique when applied on the facades works in the same way as it works for the rooftops and is illustrated in Figure 10.

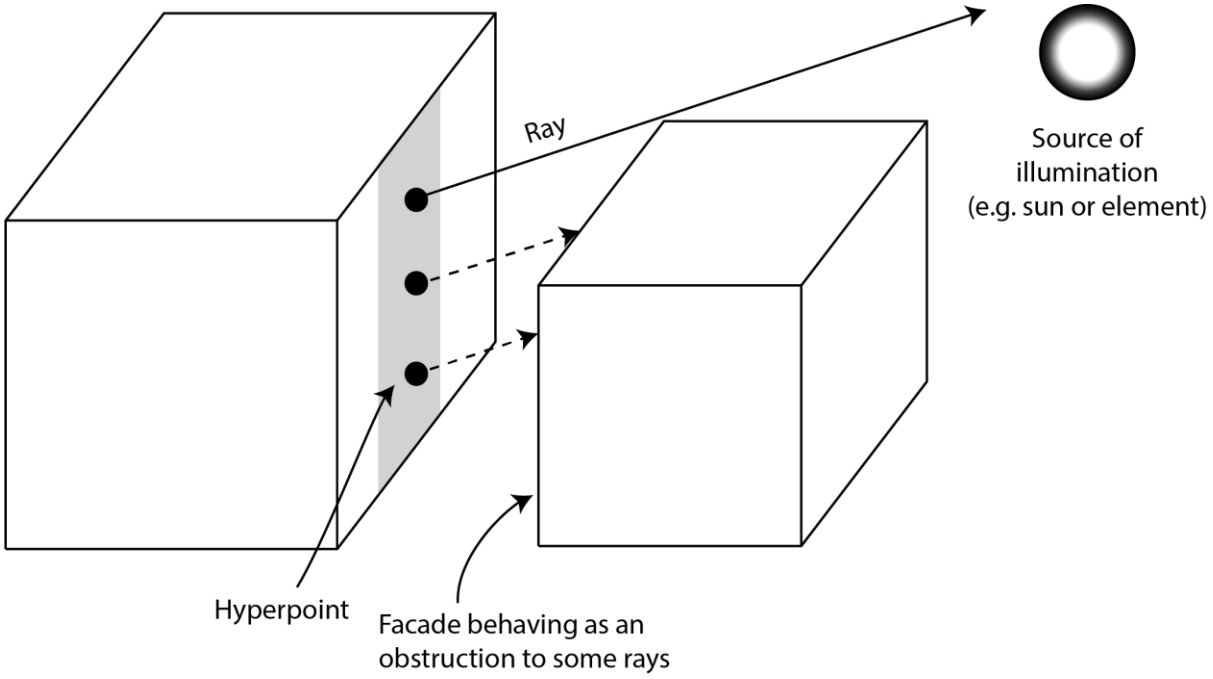

Figure 10: Illustration of backward ray-tracing for façades

According to Freitas et al [151], the accuracy of the results obtained for the façade, by the scanning algorithm based on BRT technique, hereafter referred to as the *BRT algorithm*, is highly sensitive to the hyperpoint density. This can be explained by an example, illustrated in Figure 11. Let's say that the actual height of shadow on the 10m façade is 3m. The BRT technique, when applied, results in 5m, 3.33m and 3m shadow heights when 0.2, 0.3 and 1.0 points/m of hyperpoint densities are chosen. These values correspond to 40% and 10% error in the first two scenarios whereas, the accurate results are obtained in the last scenario which corresponds to comparatively high hyperpoint density. Kokalj et al [153] provided a general rule of thumb that, smaller scanning areas, lowering the hyperpoint density and a lesser number of illuminating points in the sky for scanning lead to faster results but at the cost of accuracy. In other words, when assessing large urban areas with very large numbers of façades (e.g. modern city centres), choosing a high hyperpoint density for highly accurate results may involve a tremendous amount of computation time.

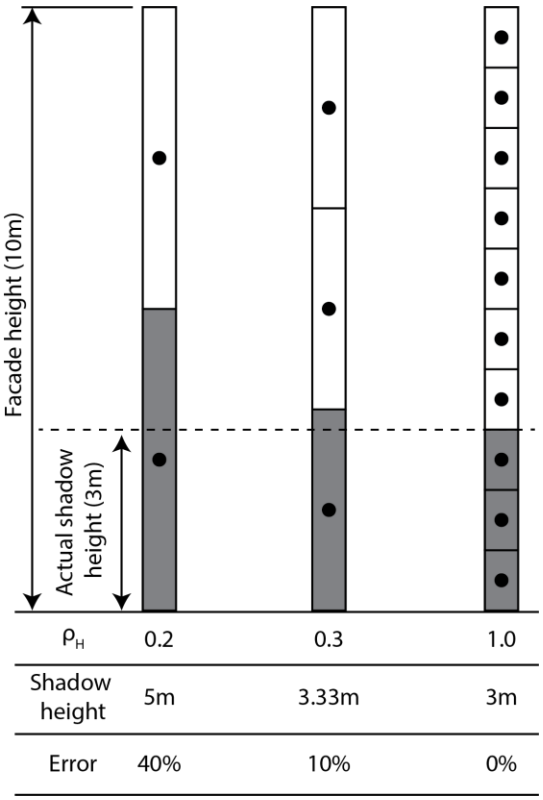

Figure 11: Effect of hyperpoint density in calculating shadow heights when using a BRT algorithm

The reversed technique to BRT is known as *Forward Ray-Tracing*, hereafter referred to as *FRT*. In this technique, the rays are traced in the forward direction, starting from the source of illumination, towards the receiving surfaces. Boer [154], while developing the indoor illumination model, noted that since the ray in FRT begins from the illumination source rather the surface, at the time of initiation the technique does not rely on the geometry of surfaces. Semlitsch [155] also appreciated this characteristic of FRT while performing simulations of thermal radiation in fluids.

Considering this advantage of FRT, a scanning algorithm based on this technique, hereafter referred to as the *FRT algorithm*, is developed for analyzing the façades and validated in this chapter. Finally, this algorithm is compared with the BRT algorithm in terms of performance.

2.2 FRT Algorithm

2.2.1 FRT Sub-Algorithms

The proposed FRT algorithm comprises two sub-algorithms: The first, termed the *Preliminary sub-algorithm*, deals with the 1.5D DEM and gives the lit heights of facades, represented as thin features. The second, termed the *Advanced sub-algorithm*, deals with the 2.5D DEM and uses the preliminary sub-algorithm to produce results.

2.2.2 Preliminary Sub-algorithm

To develop the preliminary sub-algorithm based on FRT, a typical 1.5D DEM was used as a key input describing urban features of a relief, as shown in Figure 12. This DEM consists of a number (i_o) of infinitely thin vertical features, each denoted by i, all intentionally aligned and are located on a flat terrain. The distance between each feature is d and the height is h_i, respectively. Mathematically, such a DEM is represented by a one-dimensional matrix, with each of its cells representing the height of the associated feature (i.e. for the ground, the value is zero, while for a vertical feature, it is its height).

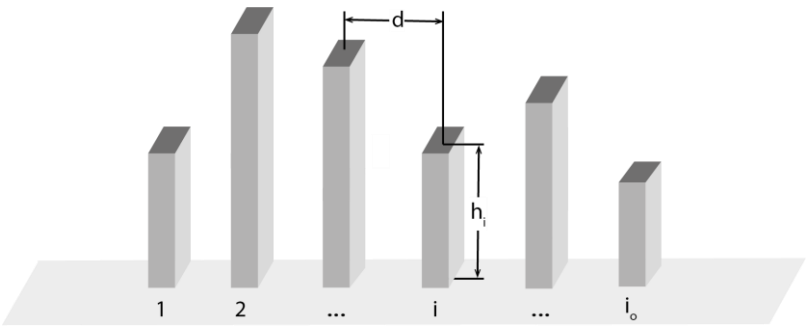

Figure 12: 1.5D DEM describing urban features of a relief

A single ray coming from a light source arrives at an altitude angle of α_G, relative to the horizontal. Considering the vertical features in the DEM and the altitude angle, the height of the shadow on the i^{th} feature due to the $(i-1)^{\text{th}}$ feature can be obtained by considering the trapezoid $abcd$, shown in Figure 13. Thus s_i is the height of the shadow, given by Eq. (3):

$$s_i = h_{i-1} - d \tan \alpha_G \qquad \textbf{(3)}$$

However, Eq. (3) is valid only as long as the height of the shadow on the $(i-1)^{\text{th}}$ feature, due to the feature located prior to it, is less than or equal to the height of that feature, i.e. $s_{i-1} \leq h_{i-1}$. As an example, feature "e" in Figure 13, has shadow height more than its own height.

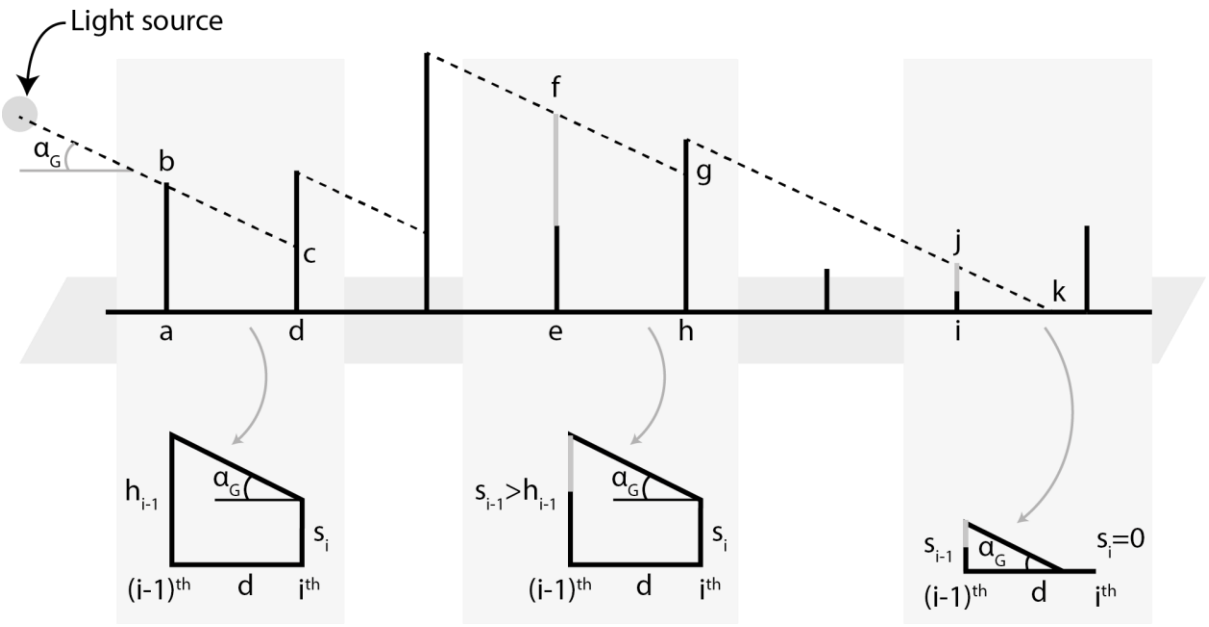

Figure 13: Shadow casting on features in 1.5D DEM

To account for a situation where the height of the shadow at the preceding feature is more than the height of the feature itself, i.e. $s_{i-1} > h_{i-1}$ ($efgh$ in Figure 13), Eq. (3) requires the modification shown in Eq. (4):

$$s_i = (h_{i-1} \vee s_{i-1}) - d \tan \alpha_G \quad \textbf{(4)}$$

Where "∨" is the maximum operator, which implies the need to pick either the height of the preceding feature, or the height of the shadow at the preceding feature, whichever is greater. For the first feature, the shadow height is assumed to be $s_1 = 0$.

In circumstances where the length of the shadow cast by a feature is not long enough to reach the following feature, Eq. (4) results in a negative value, as illustrated by triangle ijk in Figure 13. To accommodate such a situation, Eq. (4) can be modified to yield a minimum value of zero, as mathematically given by Eq. (5):

$$s_i = [(h_{i-1} \vee s_{i-1}) - d \tan \alpha_G] \vee 0 \quad \textbf{(5)}$$

where the "∨" operator physically implies that there would be no shadow on the façade if the calculated shadow height is negative.

So far, it was assumed that the lay of the land (or terrain) was flat. However, to respond to a situation where the terrain is not flat, consider a typical layout where both the terrain and surface elevations are available with reference to a common datum, as shown in Figure 14. The terrain elevation at the ith element is given by t_i and for the same element, the surface elevation is given by h_i. And so, the following modification to Eq. (5) is proposed:

$$s_i = [(h_{i-1} \vee s_{i-1}) - d \tan \alpha_G] \vee t_i \quad \textbf{(6)}$$

This modification ensures that the shadow height is at least equal to the terrain elevation, because any value of the first argument below t_i will result in a shadow below the ground, which is not realistic.

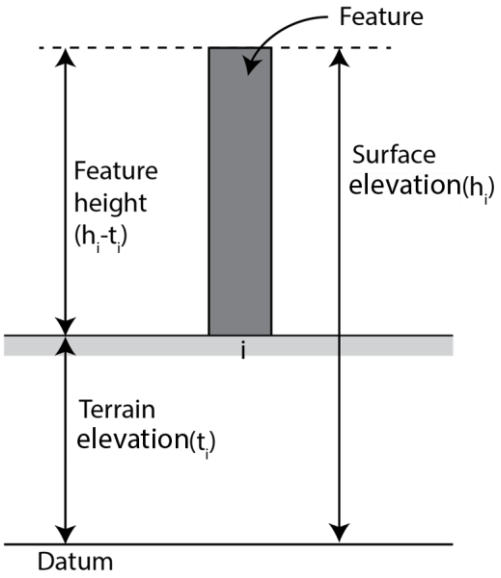

Figure 14: A typical layout where the terrain and surface elevations are available

After obtaining the heights of the shadows on every feature, the height of the lit portions of these features (l_i) can be obtained. Two cases should be considered: firstly, if the height of feature is less than or equal to the shadow height, then the whole feature is in shadow; and secondly, if the shadow height on that feature is less than the height of the feature, the difference between the heights will be the lit height. Mathematically, both cases can be expressed in a single equation as given by Eq. (7):

$$l_i = h_i - (h_i \wedge s_i) \quad \textbf{(7)}$$

Where "∧" is the minimum operator and implies taking the smaller value of the two arguments.

The value of the cells in the output represents the lit height of the vertical features. The flow chart of the preliminary sub-algorithm is shown in Figure 15.

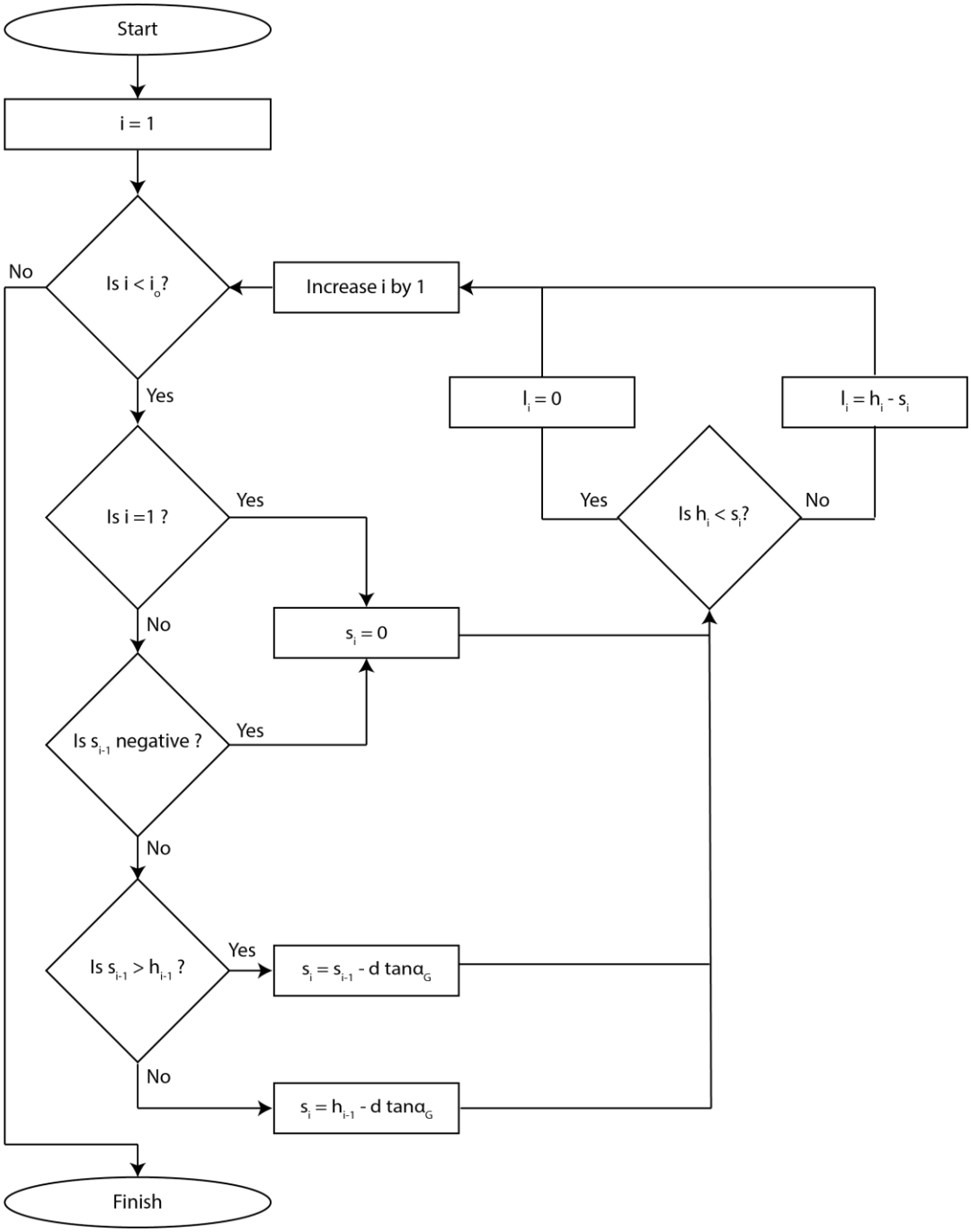

Figure 15: Flow chart representing the preliminary sub-algorithm

2.2.3 Advanced Sub-algorithm

For the advanced sub-algorithm, urban features are regarded as being composed of several vertical stripes, each associated with a cell which has a unique spatial location (x, y). Mathematically, such a

DEM is represented by an $X \times Y$ matrix, with each of its cells representing the height of the associated feature (i.e. for the ground, the value is zero, and for vertical features, e.g. façades or rooftops, it is the height of that feature). The boundaries of the DEM are marked as right, top, left and bottom. Lastly, the position of the light source in sky is defined by the altitude angle (α_G) as well as the azimuth angle (γ_G). Such a setting is illustrated in Figure 16.

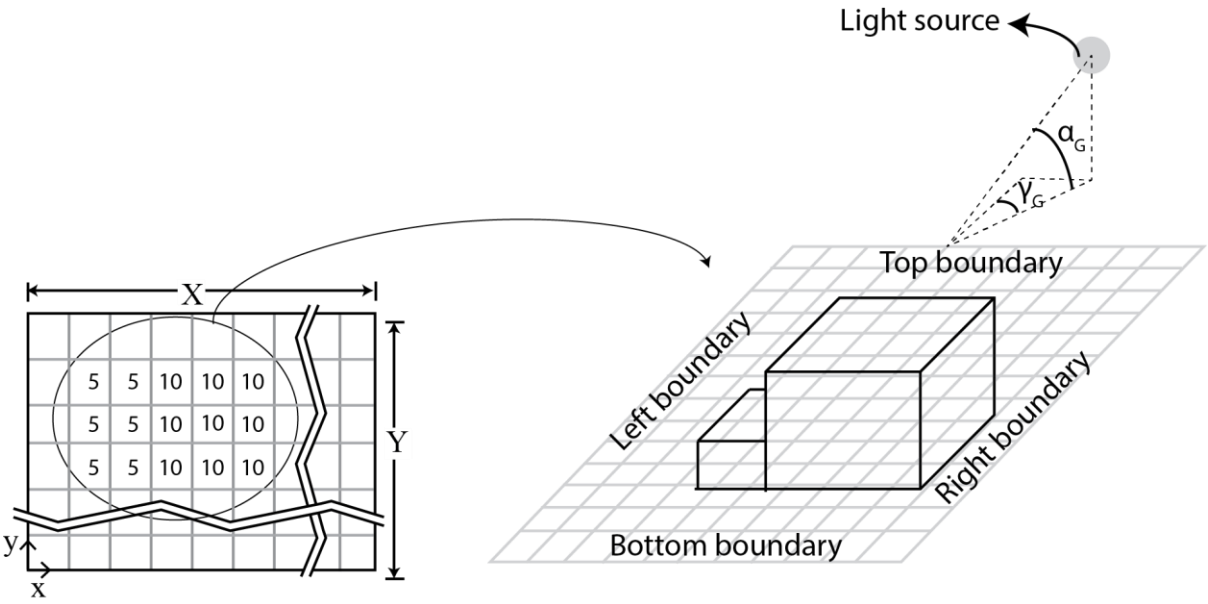

Figure 16: Illustration of a setting of a 2.5D DEM in the advanced sub-algorithm

The advanced sub-algorithm proposed here breaks down the DEM matrix into j_o number of one-dimensional matrices, each along the unique lines-of-scan ($LOS(j, \gamma_G, \alpha_G)$), which are parallel to the direction of γ_G. Extracting the LOS matrices from the DEM is a two-step procedure. Firstly, based on the value of γ_G, the initial boundaries of the DEM are selected as according to Table 4. The number of cells along these boundaries represents the total number of LOS matrices (i.e. j_o). Then, for each cell j on the boundary, a one-dimensional matrix for LOS is generated by picking the cells from the given 2.5D DEM and storing them in a virtual 1.5D DEM, starting from the boundary, and moving to the last cell, in the direction γ_G. This is illustrated in Figure 17.

Table 4: Selecting the initial boundaries in a 2.5D DEM for extracting the line-of-scan (LOS) matrices

Azimuth angle of light source (γ_G)	**Initial boundaries of 2.5D DEM**
0°	Right
$0° < \gamma_G < 90°$	Top and Right
90°	Top
$0° < \gamma_G < 180°$	Top and Left
180°	Left
$180° < \gamma_G < 270°$	Left and Bottom
270°	Bottom
$270° < \gamma_G < 360°$	Bottom and right

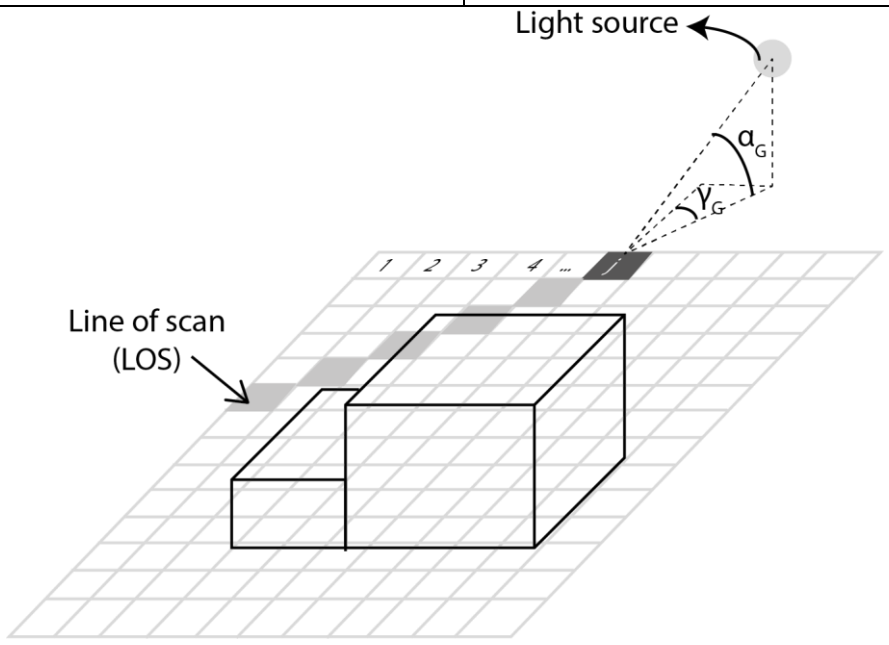

Figure 17: Extracting line-of-scan (LOS) matrices from a 2.5D DEM

After having obtained the LOS matrices, the lit heights of the façade stripes, $l(x, y, \gamma_G, \alpha_G)$, are obtained by deploying the preliminary sub-algorithm on each LOS matrix. The output of the advanced sub-algorithm is a matrix, having the same size as the given 2.5D DEM ($X \times Y$) but the values of the cells in the matrix represent the lit heights of the stripes.

2.3 Validation

2.3.1 Preliminary Sub-algorithm

To validate the preliminary sub-algorithm, a hypothetical 1.5D DEM was set up and the results were evaluated. These results were then compared with the manual measurements in a 3D drafting program.

The hypothetical 1.5D DEM consist of eight façades with random heights, as shown in Figure 18. An arbitrary altitude angle for the light source position $\alpha_G = 25°$ was chosen to perform the ray-tracing. The algorithm was executed, and the results are shown in Figure 19. Scanning started with the first feature by assuming that the shadow height was $s_1 = 0$. Then the ray hit the second feature at a height slightly below its center. The height of the shadow on the third feature was obtained similarly. In both cases, the height of the feature was more than the height of the shadow ($h_2 > s_2$ and $h_3 > s_3$). When the ray was traced from the third feature onwards, it was found to pass through a point above the height of the fourth feature ($s_4 > h_4$). Hence, the fourth feature was considered to be in complete shadow ($s_4 = h_4$). The scanning was continued from the same height (s_4) and the ray was found to hit the fifth feature at a height slightly less than its own height. Then, the ray was traced from the fifth feature and a similar situation was found for the sixth and seventh features as for the fourth feature ($s_6 > h_6$ and $s_7 > h_7$). Finally, when the ray was traced from the seventh feature, it intersected with the ground before it hit the last feature. In this situation, the last feature was considered as completely shadow-free. For all the features, the lit heights were finally evaluated.

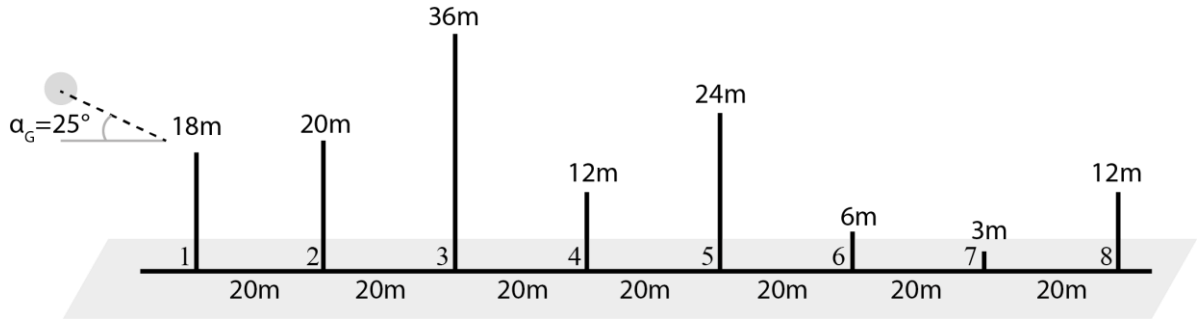

Figure 18: A hypothetical 1.5D DEM

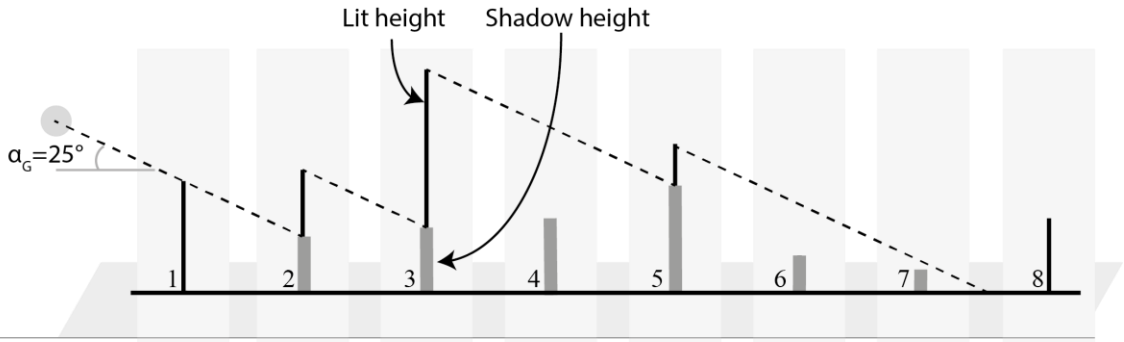

Height (h)	18 m	20 m	36 m	12 m	24 m	6 m	3 m	12 m
Shadow height (s)	0 m	8.7 m	10.7 m	12 m	17.3 m	6 m	3 m	0 m
Lit height (l)	18 m	11.3 m	25.3 m	0 m	6.7 m	0 m	0 m	12 m

Figure 19: Results of preliminary sub-algorithm for the hypothetical layout

Now, a 3D geometric model representing the same scene as in the hypothetical 1.5D DEM was created in Google Sketchup [156]. Shadows were generated by turning on the shadow feature and the results obtained are shown in Figure 20. By manually measuring and comparing the lit heights shown, the results were found to be in good agreement with the proposed preliminary sub-algorithm.

It must be noted that Google Sketchup is a 3D drafting program used for generating realistic scenes. It is not a suitable alternative to the proposed sub-algorithm because setting up the sun position and measuring the shadows' dimensions requires manual steps; hence, obtaining results for all the individual facades in a layout, at all possible sun positions during a typical year, is not a feasible

approach. Further, it has no feature allowing export of the lit heights for later use in evaluating the solar potential.

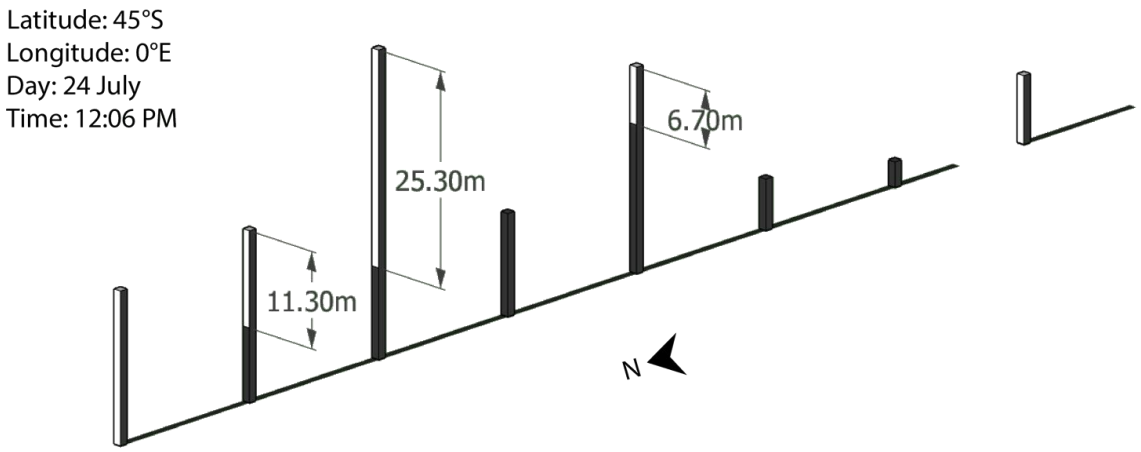

Figure 20: Comparison of results between preliminary sub-algorithm and shadow casting feature in Google Sketchup

2.3.2 Advanced Sub-algorithm

To validate the advanced sub-algorithm, a hypothetical 2.5D DEM was set up and the results were evaluated. These results were then compared with the manual measurements in a 3D drafting program.

The hypothetical layout chosen for analysis is shown in Figure 21. It consists of three buildings (A, B and C) of different heights, each having four facades. In order to reach a balanced compromise between accuracy of results and computation time, a resolution of $\Delta x = \Delta y = 1m$ was chosen when creating the $80m \times 80m$ DEM for the layout. A simulation was carried out with the light source at an arbitrary position $\alpha_G = 20°$ and $\gamma_G = 5°$, which required $j_o = 159$ lines of scans. The results are shown in Figure 22. Note that the DEM is rotated from the orientation shown in Figure 21 to show the details on different façades.

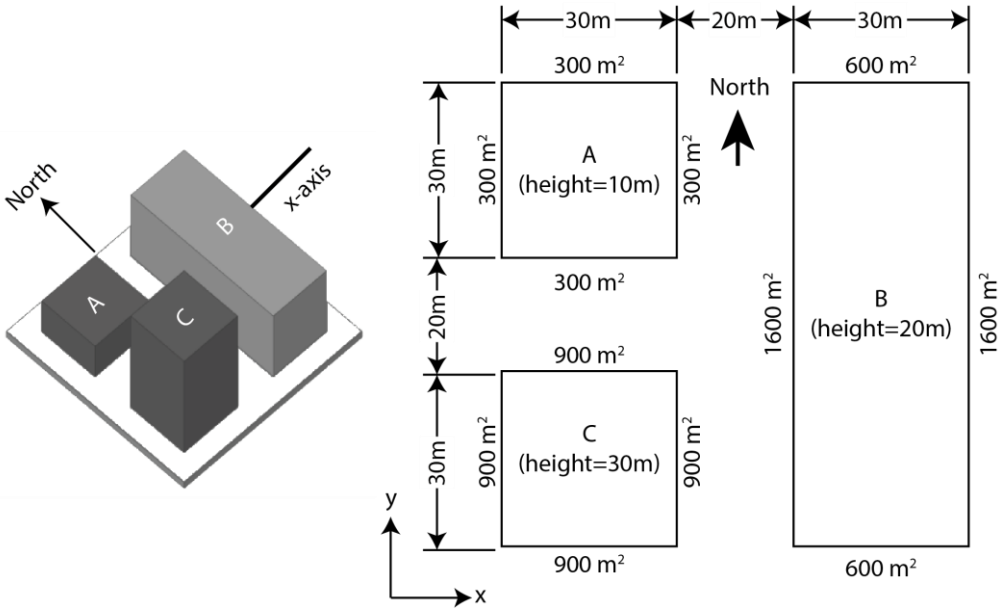

Figure 21: A hypothetical 2.5D DEM

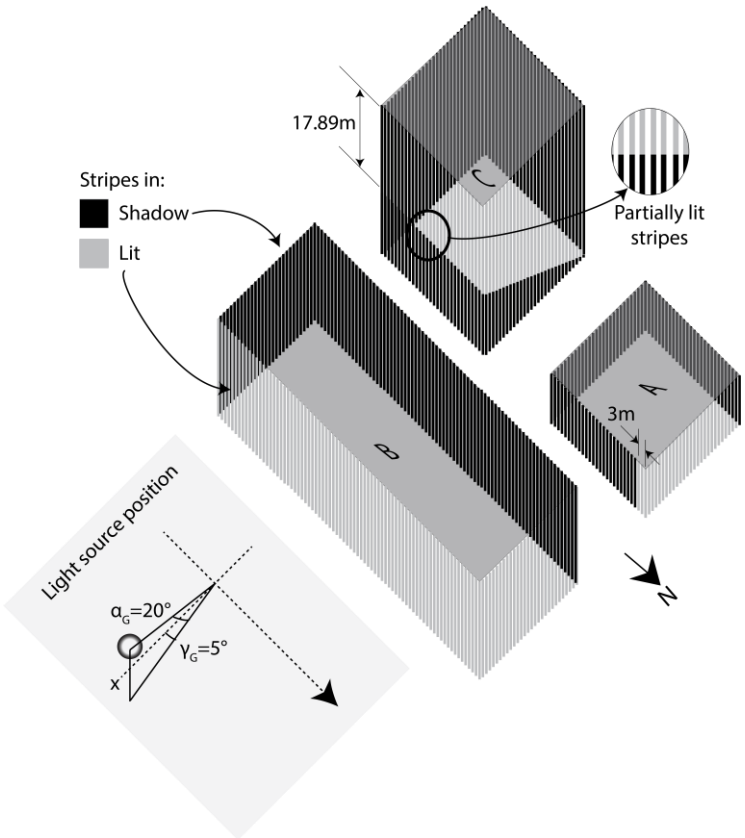

Figure 22: Results of advanced sub-algorithm

Now, a 3D geometric model representing the same scene as the hypothetical 2.5D DEM was created in Google Sketchup and the shadows were generated by turning on the shadow feature. The results obtained are shown in Figure 23. The lit heights were measured using the 'Tape Measure' tool, available in the user interface. Comparing the lit heights (e.g. for the façade of building C facing building B) showed that the results were in good agreement with each other. However, a minor discrepancy was observed with regard to the width of the lit portion on the façade of building A facing building B (near the northern corner). This was due to the limitation of DEM where the measurements are always discrete; i.e. in terms of the number of cells, and in this case, a single cell was $1m \times 1m$. The advanced sub-algorithm yielded 3 cells, corresponding to $3m^2$, while the 3D geometric model yielded $2.82m^2$, which is more precise. Ruiz-Arias et al. [152] indicated that such measurement errors are a limitation of DEM-dependent algorithms and they can be eliminated if a DEM with higher spatial resolution is employed.

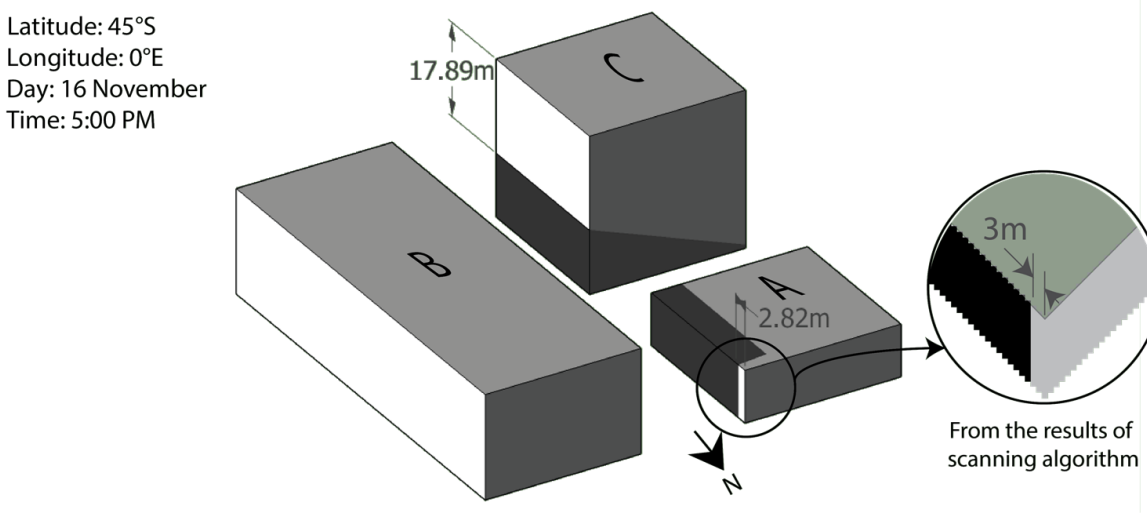

Figure 23: Comparison of results from the advanced sub-algorithm and the shadow casting feature in Google Sketchup

2.4 Performance Comparison

2.4.1 Accuracy of Results

The FRT algorithm can be justified as a reliable substitute for the BRT algorithm only if it produces the same or greater accuracy of results compared to the BRT algorithm. However, since the results of the BRT scanning algorithm are themselves sensitive to the chosen hyperpoint density [151], a reference scanning algorithm is required that considers a façade as whole i.e. without decomposing them into cells or stripes, as can be seen in Figure 24. This reference algorithm is defined here as a *benchmark model* and is derived and validated in Appendix A.

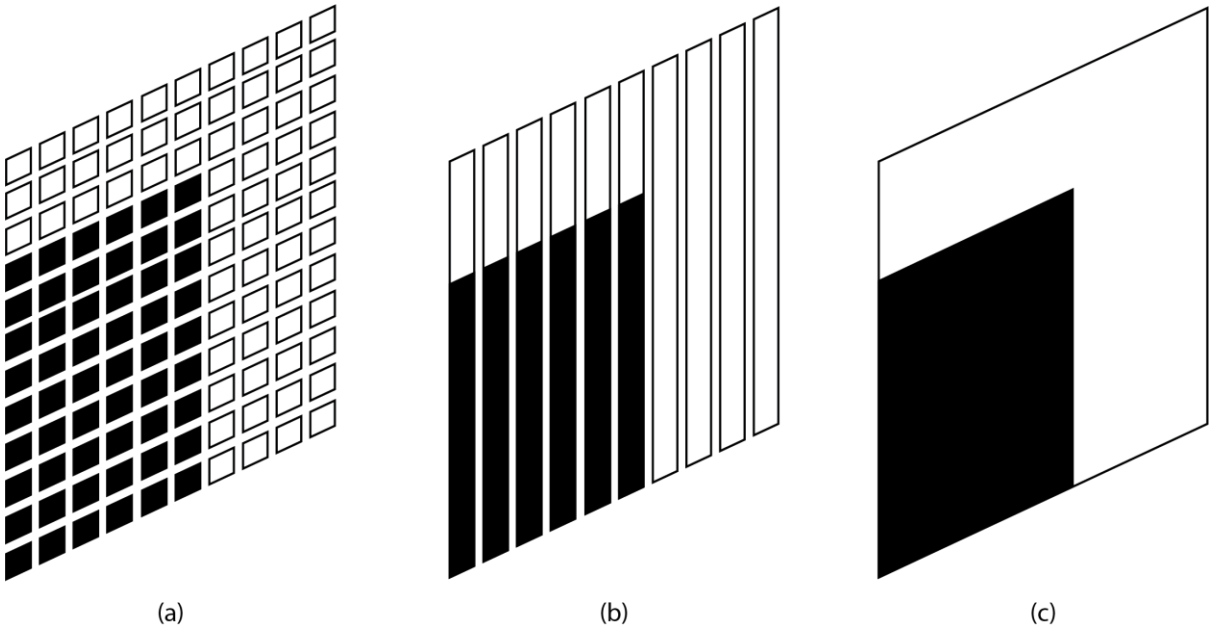

Figure 24: Difference between the treatment of façades in different scanning algorithms (a) The BRT algorithm (b) The FRT algorithm (c) The benchmark model

It is crucial to note that since the benchmark model consists of simplistic geometrical relations, it is limited to calculating the lit area of only one façade when the other façade is casting its shadow on it. In other words, it cannot be used for complex situations such as those given in DEM. Therefore, a

simple hypothetical layout was chosen for the purpose of comparison, as shown in Figure 25. The same layout was chosen for validating the results of the benchmark model (details are available in Appendix A(III)).

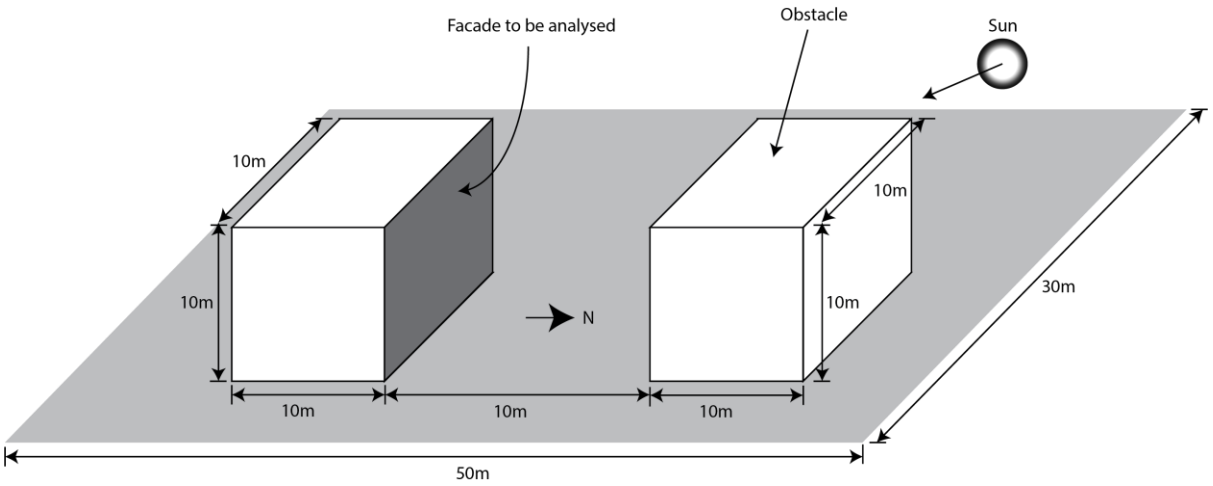

Figure 25: Hypothetical layout chosen for comparing the different scanning algorithms

The simulation was performed for a scenario where the sun is at $\alpha_G = -35°$ and $\gamma_G = 20°$ and the benchmark model yielded a lit area of 55.5m^2. The simulations were performed using BRT and FRT algorithms for the same scenario. For the BRT algorithm, it was important to choose the right hyperpoint density so as to achieve the same (or nearest) output. The simulations were therefore performed separately for a range of hyperpoint densities and the errors, which are the deviation of the results from the benchmark model, were recorded as shown in Figure 26. At low hyperpoint densities (<0.1), the error was as high as 13%. However, negligible error was observed at a hyperpoint density of 1.0 point/m.

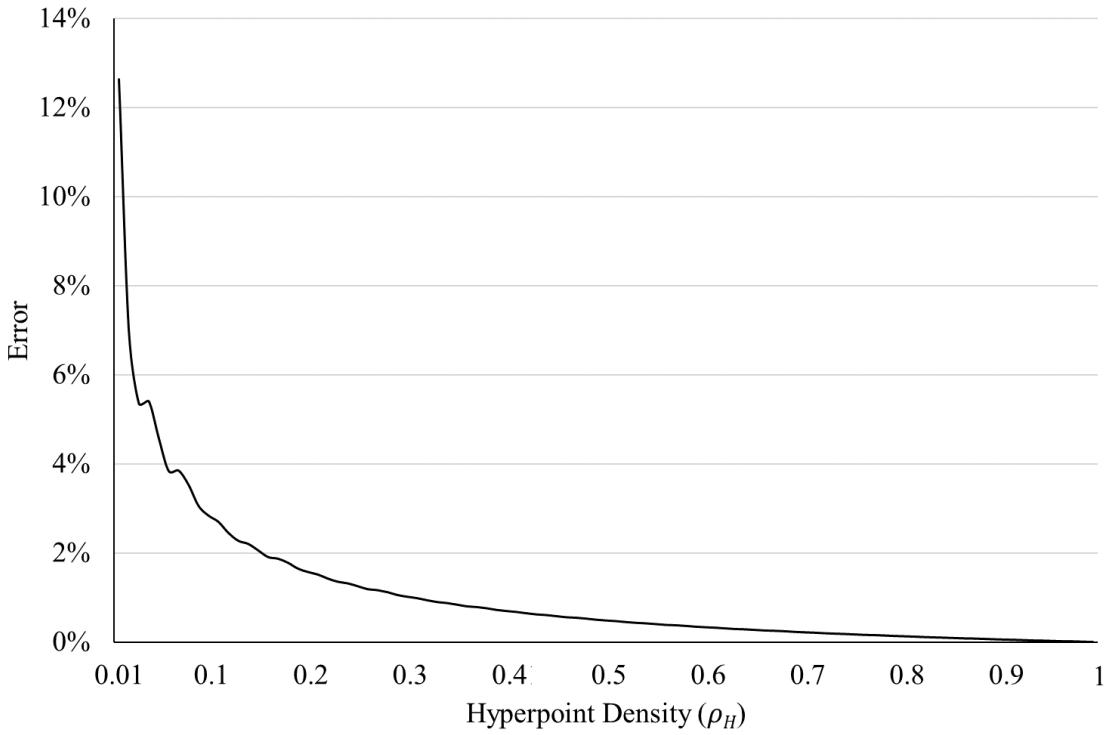

Figure 26: Effect of hyperpoint density on the accuracy of results when compared with the benchmark model for the chosen façade in a hypothetical layout when using the BRT algorithm

On the other hand, when the simulations were performed for the FRT algorithm, it resulted in the stripe-level details, which were than aggregated to obtain façade-level details. The result was found to be the same as that obtained in the benchmark model. Hence, the FRT algorithm, without decomposing the façade into hyperpoints, produced the same accuracy of results as BRT produced at a hyperpoint density of 1.0 point/m.

2.4.2 Computation Time

For comparing the performance of the BRT and FRT algorithms in terms of computation time, the simulations were performed on the local machine (RAM: 32 GB, Processor: 1 CPU x 3.4 GHz) and the time were recorded. Figure 27 is showing the computation time taken by the BRT algorithm when the different hyperpoint densities were chosen. For the hyperpoint density of 1.0 point/m, the

simulation took 340 ms to produce results compiled at the facade-level detail. On the other hand, when the simulations were performed for the FRT algorithm, it resulted directly in stripe-level details, which were than aggregated to obtain façade-level details. The whole computation time was only 85 ms, which is 4 times faster than the BRT algorithm. Note that, whenever the time is recorded for any simulation (for any of the algorithms), the simulation was performed for a couple of times and the average time to achieve the computing results is presented.

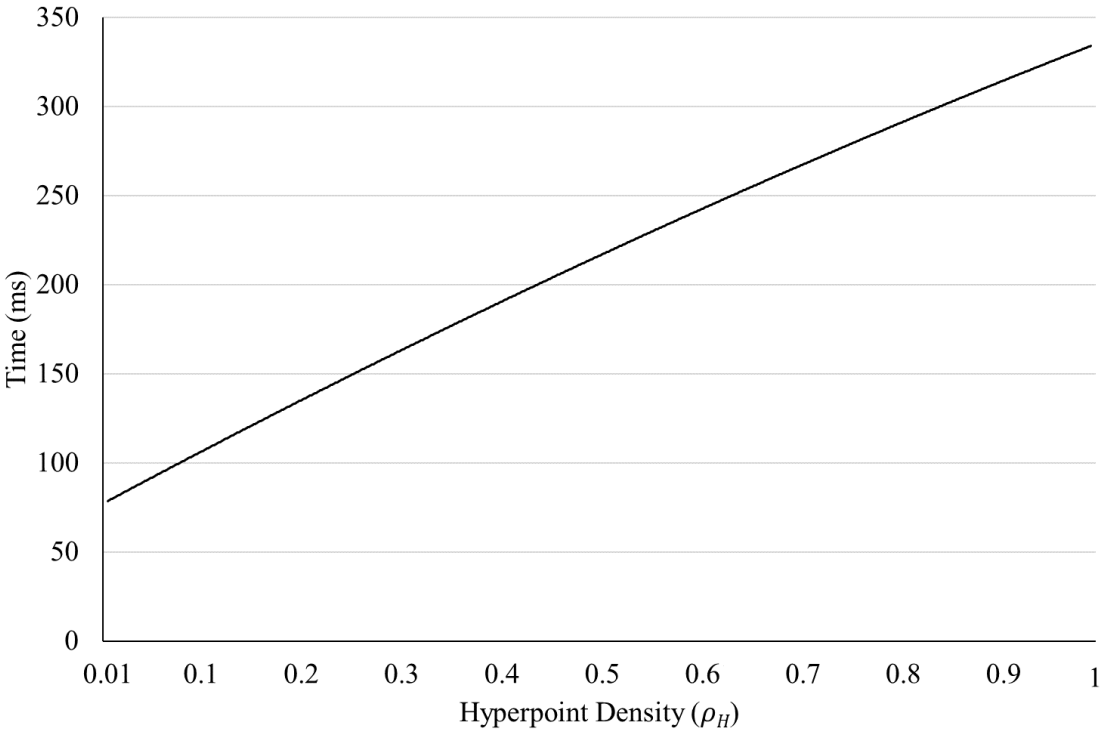

Figure 27: Effect of hyperpoint density on computation time for the chosen façade in a hypothetical layout when using the BRT algorithm

2.5 Programming Codes

The codes for the Preliminary sub-algorithm are available in ‘codes/PrimSubAlgo/PrimSubAlgo.php’. Whereas the codes for the Advanced sub-algorithm are available in ‘codes/AdvSubAlgo/AdvSubAlgo.php’.

2.6 Summary

An FRT technique-based discretization-independent scanning algorithm for extracting the lit heights of the façades in a 2.5D DEM was proposed in this chapter. It comprises two sub-algorithms, the preliminary sub-algorithm, which deals with 1.5D DEM; and the advanced sub-algorithm, which uses the preliminary sub-algorithm for computing the lit heights of façades in 2.5D DEM. The sub-algorithms were validated by comparing their simulation results for the hypothetical layouts with results from Google Sketchup, which is a 3D drafting program. Then, the performance of the BRT and FRT algorithms was compared. For the purpose, the benchmark model was used as a reference algorithm. The accuracy and computation time of the BRT algorithm were found to be directly proportional to the hyperpoint density. The BRT algorithm produced accurate results at a hyperpoint density of 1.0 point/m. In contrast, the developed FRT algorithm yielded accurate results without decomposing the façades, while remaining 4 times faster than the BRT algorithm.

3

DEVELOPMENT OF BEAM SOLAR POTENTIAL SUB-MODEL

3.1 Introduction

In the previous chapter, an FRT technique-based discretization-independent scanning algorithm for extracting the lit heights of the façades in a 2.5D DEM was developed. In this chapter, a sub-model, compatible with the proposed FRT algorithm, for computing the beam solar potential of façades is developed, and is termed the *FRT beam sub-model*. Since this sub-model is based on an FRT algorithm it is independent of the façade discretization. Finally, the performance of the proposed sub-model is compared with the conventional BRT algorithm-based beam sub-model, hereafter termed the *BRT beam sub-model*.

3.2 FRT Beam Sub-model

One way to communicate geographic solar potential is to present the instantaneous radiant flux (kJ/hr), or the accumulated radiant energy (kJ) over the time span, received by the surface. In the case of beam radiation, the radiant flux can be obtained by multiplying the theoretical beam solar irradiance (kJ/hr.m^2) by the area of the receiving surface (m^2) that is normal to the direction of the sun's rays. Hence, the position of the sun in the sky, as well as the angular characteristics of the surface, affects the beam solar potential.

The location of the sun can be described by its azimuth (γ_b) and altitude (α_b) angles. γ_b is the angle measured between true north (in the southern hemisphere) and the projection of the line connecting sun and the receiving point at ground. It is zero when the sun is at north (noon), positive when the sun is to the west of north, and otherwise negative. α_b is measured from the horizontal, upward to the location of sun. At solar noon the sun is at its maximum altitude. The angular characteristics of the surface are described by the surface azimuth angle (γ) and tilt angle (β). γ has the same sign convention as γ_b whereas, β is measured from the horizontal and is always positive. All these angles are graphically summarized in Figure 28.

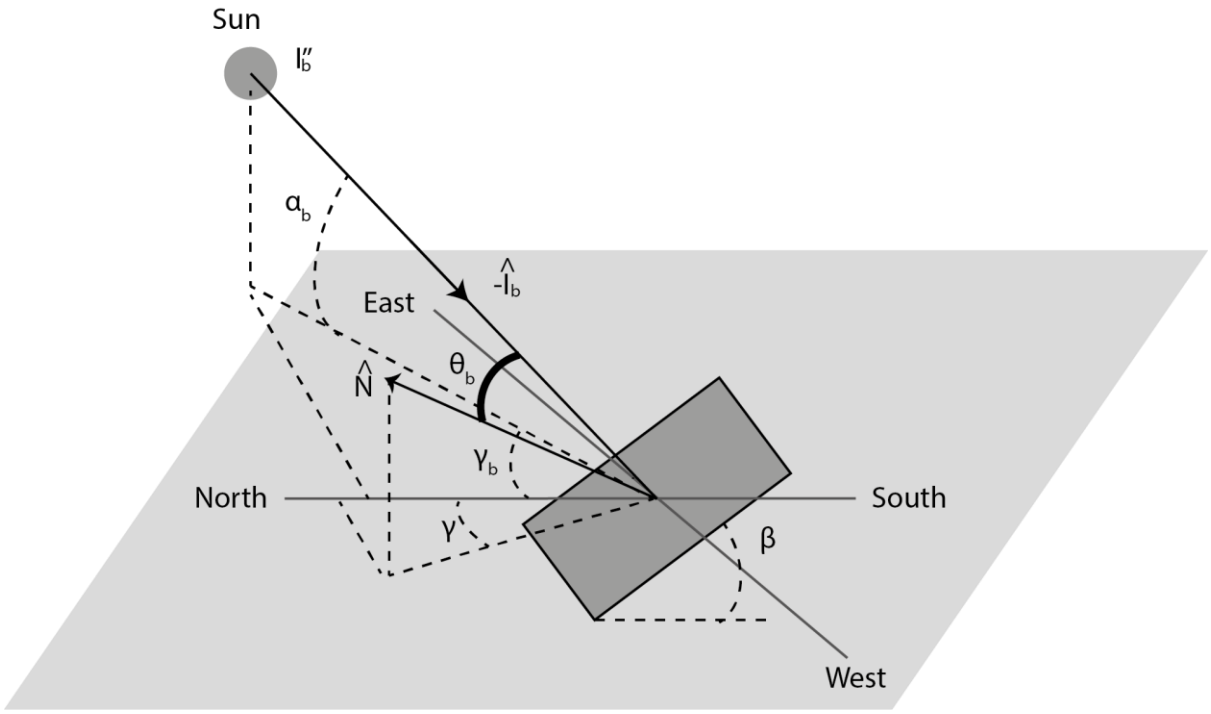

Figure 28: Angles describing the position of the sun in the sky somewhere in the southern hemisphere and the angular characteristics of the receiving surface

If I_b'' (kJ/hr.m^2) is the theoretical beam solar irradiance (obtained from a geolocation-tied database), the beam radiant flux (I_b, kJ/hr) can be obtained by using Eq. (8):

$$I_b = I_b'' A \cos\theta_b \qquad \textbf{(8)}$$

Where A (m^2) is the surface area and θ_b represents the incidence angle, which is the angle between the direction of the beam and the normal to the surface. θ_b can be obtained from the knowledge of the vectors representing these directions. So, if $\hat{I}_b$ and $\hat{N}$ represent the unit vectors of the ray and the surface normal, respectively, then they can be written mathematically as Eq. (9) and (10):

$$\hat{I}_b = \cos\gamma_b \cos\alpha_b \,\hat{\imath} + \sin\gamma_b \cos\alpha_b \,\hat{\jmath} + \sin\alpha_b \,\hat{k} \qquad \textbf{(9)}$$

$$\hat{N} = \cos\gamma \sin\beta\, \hat{\imath} + \sin\gamma \sin\beta\, \hat{\jmath} + \cos\beta\, \hat{k} \quad \textbf{(10)}$$

Thus, the incidence angle can be evaluated by Eq. (11):

$$\theta_b = \cos^{-1}\left(\frac{\hat{I}_b \cdot \hat{N}}{|\hat{I}_b||\hat{N}|}\right) \quad \textbf{(11)}$$

where "." represents the vector dot-product and $|\hat{I}_b|$ and $|\hat{N}|$ represent the magnitudes of the corresponding vectors ($|\hat{I}_b||\hat{N}| = 1$ as they both are unit vectors).

To obtain the incidence angle for the vertical façades, $\beta = 90°$, and $\gamma = \gamma_F$ (which is the orientation angle of façade) are substituted in Eq. (10), which reduces it to Eq. (12):

$$\hat{F} = \cos\gamma_F\, \hat{\imath} + \sin\gamma_F\, \hat{\jmath} \quad \textbf{(12)}$$

where $\hat{F}$ represents a unit vector representing the normal to the façade, which depends only on its orientation.

When applying this concept to a sky-obstructed urban relief, where the features are described in a 2.5D DEM, a variation of a DEM that can identify the directions of façades (the normals to the façades, in other words) would be required, as illustrated in Figure 29. The other information required is the position of the sun in the sky and the magnitude of beam irradiance. Existing geolocation-tied databases can be used for this purpose. In such databases, the altitude angle, azimuth angle and beam irradiance are represented as functions of the hour (τ, hr) of the year i.e. $\alpha_b(\tau)$, $\gamma_b(\tau)$ and $I_b''(\tau)$, respectively. Lastly, the lit heights of the façade stripes at a given hour are also required, which can be obtained from the FRT algorithm, developed in Chapter 2.

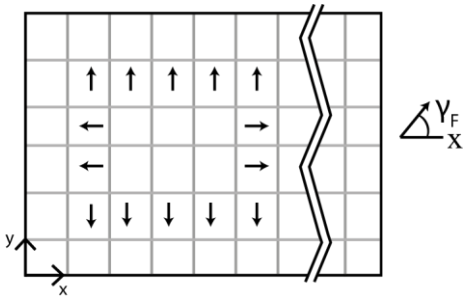

Figure 29: Illustration of a variation of a DEM showing the normal to each façade

The radiant flux, $I_b(x, y, \tau)$, at any instant of time τ, received by a façade stripe located at (x, y) and having an orientation of $\gamma_F(x, y)$, can be estimated from Eq. (13):

$$I_b(x, y, \tau) = I_b''(\tau)\, W\, l_b(x, y, \tau)\, \delta_b(x, y, \tau) \qquad \textbf{(13)}$$

where W (m) represents the width of the façade cell, which depends upon the spatial resolution of DEM and is constant for all the stripes in a DEM, $l_b(x, y, \tau)$ is the lit height of that particular stripe, as graphically illustrated in Figure 30(a), and the factor δ_b is the incidence effect factor, which depends entirely upon the orientation of the façade and the direction of the beam. It can be expressed as Eq. (14):

$$\delta_b(x, y, \tau) = \left[\cos\left(\theta_b(x, y, \tau)\right)\right] \vee 0 \qquad \textbf{(14)}$$

where $\theta_b(x, y, \tau)$ is the angle of incidence, as shown in Figure 30(a). The maximum operator '$\vee$' discards the irradiance if it arrives from behind the exposed surface of the façade (i.e. $90° < \theta_b(x, y, \tau) < 270°$).

The value of θ_b can be obtained from knowledge of the vectors and is given by Eq. (15):

$$\theta_b(x, y, \tau) = \cos^{-1}\left(\hat{I}_b(\tau) \cdot \hat{F}(x, y)\right) \qquad \textbf{(15)}$$

where $\hat{I}_b(\tau)$ and $\hat{F}(x,y)$ are the unit vectors representing the directions of the beam irradiance and the normal to the façade, respectively. These vectors can be written mathematically as Eq. (16) and Eq. (17), respectively:

$$\hat{I}(\tau) = \cos\big(\gamma_{bN}(\tau)\big)\cos\big(\alpha_b(\tau)\big)\,\hat{\imath} + \sin\big(\gamma_{bN}(\tau)\big)\cos\big(\alpha_b(\tau)\big)\,\hat{\jmath} + \sin\big(\alpha_b(\tau)\big)\,\hat{k} \qquad \textbf{(16)}$$

$$\hat{F}(x,y) = \cos\big(\gamma_F(x,y)\big)\,\hat{\imath} + \sin\big(\gamma_F(x,y)\big)\,\hat{\jmath} \qquad \textbf{(17)}$$

where γ_{bN} is the azimuthal position of the sun, measured counter-clockwise from the x-axis, as illustrated in Figure 30(b). The γ_{bN} can be determined using Eq. (18):

$$\gamma_{bN}(\tau) = \gamma_b(\tau) + \gamma_N \qquad \textbf{(18)}$$

where γ_N is the angle of true north measured CCW from the x-axis.

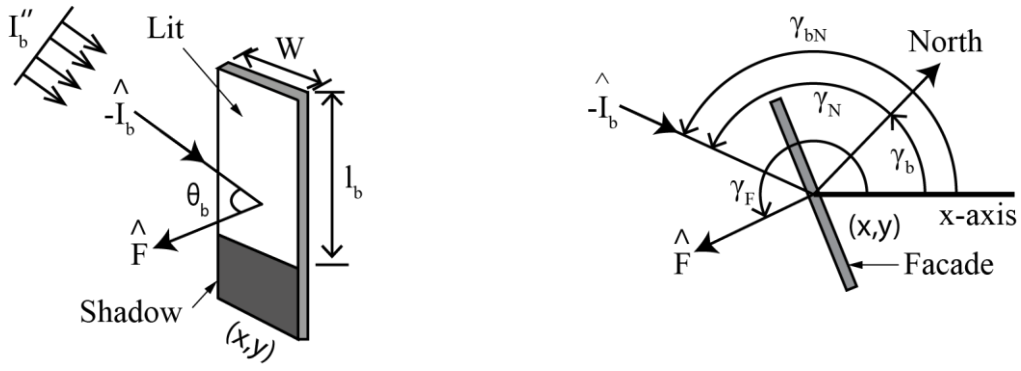

(a) **(b)**

Figure 30: (a) A façade stripe receiving solar beam radiation (b) Top view of stripe showing various azimuthal angles

Finally, the radiant beam energy ($H_b(x,y)$) of a façade stripe can be obtained by accumulating the radiant fluxes over the given time span, as given by Eq. (19):

$$H_b(x,y) = \sum_{\tau} I_b(x,y,\tau) \quad \textbf{(19)}$$

3.3 Performance Comparison

3.3.1 Accuracy of Results

As before, the simulation results obtained from the benchmark model were used as a reference for comparing the accuracy of the results of the BRT and FRT beam sub-models. The scenario described in Figure 25 (Chapter 2) was taken into account. For the single instant of time when the sun is at $\alpha_G = -35°$ and $\gamma_G = 20°$ and considering a beam normal irradiance of 500 W/m^2, the benchmark model yielded an instantaneous beam radiation potential of 21 777 W. The BRT beam sub-model yielded the same value but at a hyperpoint density of 1.0 point/m. In contrast, the FRT beam sub-model produced the same value but without discretizing the façade into cells.

After performing simulations for a single instant of time, the accuracies of the beam sub-models were compared to evaluate the annual beam radiation potential of the façade. The layout was assumed to be in Auckland and the sun position and radiation data were obtained from a geolocation-tied database [48]. In simulations, the benchmark model produced an annual beam radiation potential of 283,479,184 J. The BRT beam sub-model, at a hyperpoint density of 1.0 point/m, yielded a value of 280,891,018 J, which was 99.01% accurate, whereas the FRT beam sub-model, without discretizing the façade into cells, yielded a value of 281,148,984 J, which was 99.17% accurate.

3.3.2 Computation Time

The performance of the BRT and FRT beam sub-models in terms of their computation time was compared by recording their simulation times on the same local machine that was used in Chapter 2

(RAM: 32 GB, Processor: 1 CPU x 3.4 GHz). At a hyperpoint density of 1.0 points/m, the simulation using the BRT sub-model took 342 ms to produce results at facade-level detail. In contrast, the FRT beam sub-model produced results at stripe-level detail, which were than aggregated to the façade-level details, and the whole time for the computation was only 87 ms. Hence, the FRT beam sub-model was found to be computing at speed 3.9 times faster than the BRT beam sub-model.

Comparing the computation time when evaluating the annual beam radiation potential, the BRT beam sub-model required 15 minutes. In comparison, the FRT beam sub-model took only 3 minutes and 20 seconds. Therefore, the FRT beam sub-model was found to be 4.5 times faster than the BRT beam sub-model.

3.4 Summary

A sub-model for estimating the beam solar potential of façades using the 2.5D DEM, compatible with the discretization-independent FRT based scanning algorithm, was developed in this chapter. Then, the performance of the BRT and FRT beam sub-models was compared by simulating them for a single instant of time as well as by evaluating annual beam radiation potential. The BRT beam sub-model produced accurate results at a hyperpoint density of 1.0 point/m, whereas the FRT beam sub-model responded with nearly the same accuracy but without discretizing the façade into cells. On comparing computation times, the FRT beam sub-model was found to be 3.9 to 4.5 times faster than the BRT beam sub-model. A summary of the performance comparisons between the BRT and FRT beam sub-models is shown in Table 5.

Table 5: Summary of performance comparison between the BRT and FRT beam sub-models

Beam solar potential assessment		**Benchmark model (Appendix A)**	**BRT beam sub-model (At hyperpoint density of 1.0 point/m)**	**FRT beam sub-model (Proposed)**
At a single instant of time	**Result and accuracy**	21 777 W	21 777 W (100%)	21 777 W (100%)
	Simulation time	Not recorded	342 ms	87 ms
Annual	**Result and accuracy**	283 479 184 J	280 891 018 J (99.01%)	281 148 984 J (99.17%)
	Simulation time	Not recorded	15 minutes	3 minutes 20 sec

4

DEVELOPMENT OF ISOTROPIC DIFFUSE SOLAR POTENTIAL SUB-MODEL

4.1 Introduction

In the previous chapter, a sub-model for estimating the beam solar potential of façades using the 2.5D DEM, compatible with the discretization-independent FRT based scanning algorithm, was developed. This chapter focuses on developing a sub-model, compatible with the proposed FRT algorithm, for computing the isotropic diffuse solar potential of façades, and is termed the *FRT isotropic diffuse sub-model*. Since this sub-model is based on an FRT algorithm it is independent of the façade discretization. The performance of the proposed sub-model is then compared with the conventional

BRT algorithm-based isotropic diffuse sub-model, hereafter termed the *BRT isotropic diffuse sub-model*.

4.2 FRT Isotropic Diffuse Sub-model

In contrast with beam radiation, which reaches the surface from a single direction, diffuse radiation approaches from all directions and hence is treated differently. The theoretical potential of diffuse radiation is generally available in the form of irradiance on the horizontal received under an unobstructed sky (I_d'', kJ/hr.m^2). However, for transforming this potential into the geometric potential, the sky discretization technique is generally employed. In this technique, the celestial sky vault around the surface is divided into a number of finite areas, known as sky elements, in which each element behaves as a source of illumination. Every element has its unique location in the sky, denoted by its azimuth angle (γ_e) and altitude angle (α_e), as shown in Figure 31. The γ_e is measured on the base of the vault, whereas α_e is measured upward from the base of vault.

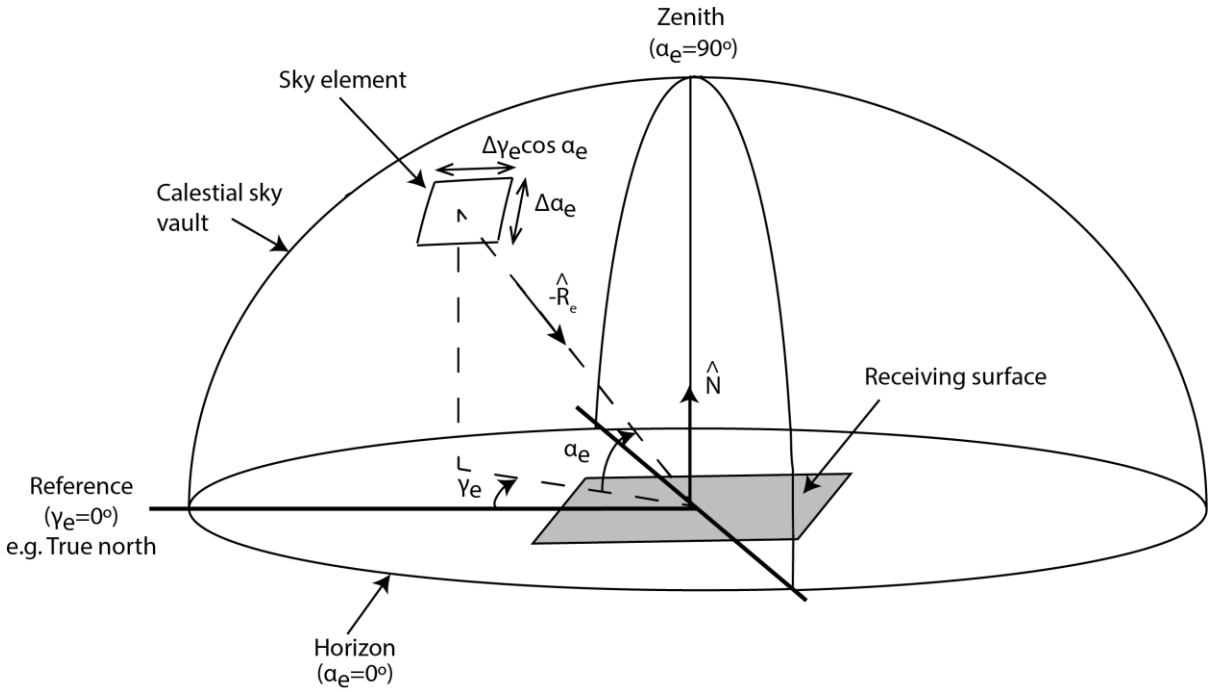

Figure 31: Discretized celestial sky vault around a receiving surface

The surface area of the sky element plays an important role when estimating the radiant flux or energy of its associated radiant source. The solid angle (ω_e, sr), which characteristically represents that area depends on α_e and can be calculated using Eq. (20):

$$\omega_e(\alpha_e) = \Delta\gamma_e \Delta\alpha_e \cos\alpha_e \quad \textbf{(20)}$$

where $\cos\alpha_e$ accounts for the increment in the element's area from the zenith of the vault to its base, as illustrated in Figure 32, and $\Delta\gamma_e$ and $\Delta\alpha_e$ denote the azimuthal and altitudinal dimensions of a single element at the base of the vault. Choosing the values of $\Delta\gamma_e$ and $\Delta\alpha_e$ is crucial as they describe the sky discretization resolution ($\rho_S = \sqrt{\Delta\gamma_e \Delta\alpha_e}$), which eventually sets the number of elements (n) in the sky for analysis, as given by Eq. (21):

$$n = \frac{90 \times 360}{\rho_S^2} \quad \textbf{(21)}$$

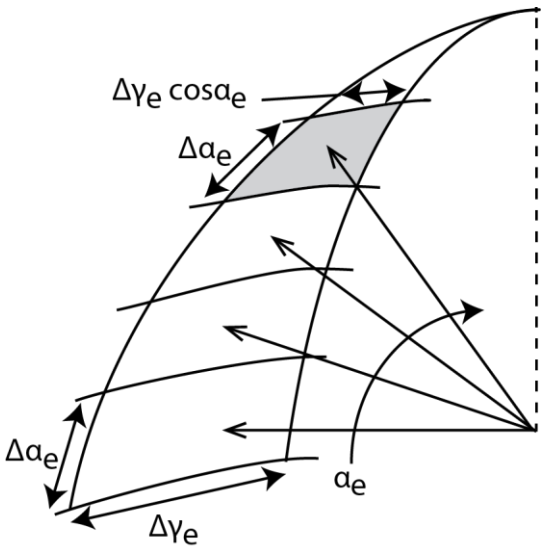

Figure 32: Area of sky element as a function of its altitude angle

The magnitude of the radiance, received by the horizontal surface, in an isotropically radiant sky (R_{iso}, kJ/hr.m^2.sr), which is the fraction of diffuse radiation approaching from its associated sky element, can be obtained using Eq. (22) [130]:

$$R_{iso} = \frac{I_d''}{\sum_{\gamma_e} \sum_{\alpha_e} (\omega_e \ \sin \alpha_e)} \quad \textbf{(22)}$$

where the multiplier $\sin \alpha_e$ in the denominator accounts for the incidence effect of the radiance with the horizontal surface.

Thus, the fractional radiant flux ($I'_{d,iso}$, kJ/hr) that is collected by an arbitrarily tilted surface after receiving the radiance approaching from a single sky element located at (α_e, γ_e) is given by Eq. (23):

$$I'_{d,iso}(\gamma_e, \alpha_e) = R_{iso} \ \omega_e(\alpha_e) \ A \ \cos \theta_e \quad \textbf{(23)}$$

where A (m^2) is the area of the receiving surface (assuming it is completely lit) and θ_e is the angle of incidence between the direction of the element's radiance and the normal to the arbitrarily tilted surface. This angle can be obtained by using Eq. (11):

$$\theta_e = \cos^{-1}\left(\hat{R}_e \cdot \hat{N}\right) \quad \textbf{(24)}$$

where $\hat{R}_e$ is the unit vector representing the direction of the radiance approaching from the sky element at (γ_e, α_e), given by Eq. (25):

$$\hat{R}_e = \cos \gamma_e \cos \alpha_e \, \hat{\imath} + \sin \gamma_e \cos \alpha_e \, \hat{\jmath} + \sin \alpha_e \, \hat{k} \quad \textbf{(25)}$$

and $\hat{N}$ can be obtained using Eq. (10), available in Chapter 3.

Finally, the diffuse radiant flux ($I_{d,iso}$, kJ/hr) received by the arbitrarily tilted surface is the sum of the fractions of the radiant fluxes approaching from all the sky elements, given by Eq. (26):

$$I_{d,iso} = \sum_{\gamma_e} \sum_{\alpha_e} I'_{d,iso} \qquad \textbf{(26)}$$

When applying this concept to a sky-obstructed situation, where the urban features are described in a 2.5D DEM, variations in the DEM to represent the normal to the façades ($\gamma_F(x,y)$) are again required, as discussed in Chapter 3. The other information required is the isotropic diffuse irradiance ($I''_d(\tau)$, kJ/hr.m^2) on the horizontal, which can be obtained from existing geolocation-tied databases. In such databases, this irradiance is represented as a function of hour (τ, hr) of the year. This eventually gives a temporal dimension to the radiance, fractional radiant flux and diffuse radiant flux i.e. $R_{iso}(\tau)$, $I'_{d,iso}(x,y,\gamma_e,\alpha_e,\tau)$ and $I_{d,iso}(x,y,\tau)$, respectively.

The diffuse radiant flux, $I_{d,iso}(x,y,\tau)$, at any instant of time τ, collected from all the sky elements by a façade stripe located at (x,y) and having an orientation of $\gamma_F(x,y)$, can be estimated from Eq. (13):

$$I_{d,iso}(x,y,\tau) = R_{iso}(\tau) \sum_{\gamma_e} \sum_{\alpha_e} \omega_e(\alpha_e)\, W\, l_d(x,y,\gamma_e,\alpha_e)\, \delta_d(x,y,\gamma_e,\alpha_e) \qquad \textbf{(27)}$$

where again W (m) represents the width of the cell, which is constant for all the stripes in a DEM, $l_d(x,y,\gamma_e,\alpha_e)$ is the lit height of that particular stripe and the incidence factor $\delta_d(x,y,\gamma_e,\alpha_e)$, which accounts for the orientation of the façade and direction of the radiance, as given by Eq. (14):

$$\delta_d(x,y,\gamma_e,\alpha_e) = \left[\cos\left(\theta_d(x,y,\gamma_e,\alpha_e)\right)\right] \vee 0 \qquad \textbf{(28)}$$

where $\theta_d(x,y,\gamma_e,\alpha_e)$ is the angle of incidence between the direction of the element's radiance and the normal to the surface, as illustrated in Figure 33. The maximum operator '$\vee$' discards the radiance if it arrives from behind the exposed surface of the vertical façade (i.e. $90° < \theta_d(x,y,\alpha_e,\gamma_e) < 270°$).

The value of θ_d can be obtained from knowledge of the vectors and is given by Eq. (15):

$$\theta_d(x, y, \alpha_e, \gamma_e) = \cos^{-1}\left(\hat{R}_e(\gamma_e, \alpha_e) \cdot \hat{F}(x, y)\right) \quad \textbf{(29)}$$

where $\hat{F}(x, y)$ is given by Eq. (17), available in Chapter 3.

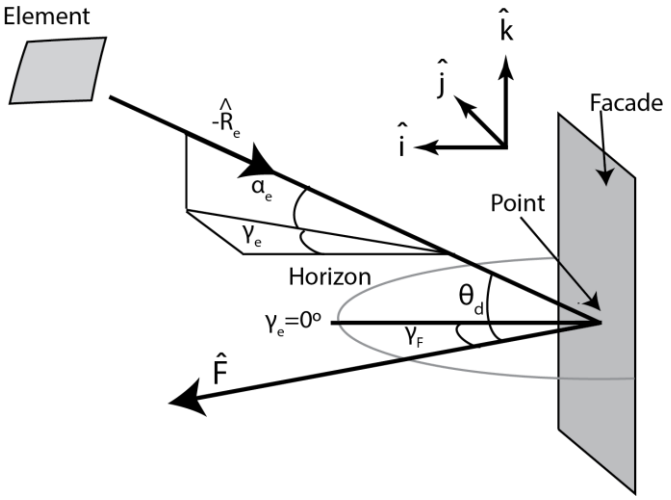

Figure 33: Illustration of angle of incidence

By substituting Eq. (22) in Eq. (13) and simplifying it to separate the spatial-only parameters, the relation given in Eq. (30) is obtained:

$$\frac{I_{d,iso}(x, y, \tau)}{I_d''(\tau)} = \frac{\sum_{\gamma_e}\sum_{\alpha_e}\omega_e(\alpha_e)\, W\, l_d(x, y, \gamma_e, \alpha_e)\, \delta_d(x, y, \gamma_e, \alpha_e)}{\sum_{\gamma_e}\sum_{\alpha_e}(\omega_e\ \sin\alpha_e)} \quad \textbf{(30)}$$

where the right-hand-side term is purely spatial in nature. Also, the denominator of this term is a constant, independent to layout, and could be evaluated prior to any simulation. This separation leads to considerable reduction in the overall processing time when evaluating the radiant energy ($H_{d,iso}(x, y)$) of any façade stripe, which is the integral of the temporal radiant fluxes of the stripes during the assessment period. This is because the scanning need only be done once, given that the urban layout is unchanged. Once the right-hand side term is evaluated, it can be multiplied by the sum of the $I_d''(\tau)$ over the analysis period to yield a radiant energy for each (x, y) stripe, as shown by Eq. (19):

$$H_{d,iso}(x,y) = \sum_{\tau} I''_d(\tau) \,.\, \frac{\sum_{\gamma_e} \sum_{\alpha_e} \omega_e(\alpha_e)\, W\, l_d(x,y,\gamma_e,\alpha_e)\, \delta_d(x,y,\gamma_e,\alpha_e)}{\sum_{\gamma_e} \sum_{\alpha_e} (\omega_e\ \sin\alpha_e)} \quad \textbf{(31)}$$

where the scanning is performed using FRT algorithm, considering all the sky elements one by one ($0° \leq \gamma_e < 360°$ and $0° \leq \alpha_e \leq 90°$).

It is interesting to note that dividing both the sides of Eq. (30) by the area of the stripe ($A(x,y)$) reveals a dimensionless parameter, herein defined as the *Diffuse Sky Factor* (DSF), as mathematically given by Eq. (32):

$$DSF_{iso}(x,y) = \frac{\sum_{\gamma_e} \sum_{\alpha_e} \omega_e(\alpha_e)\, W\, l_d(x,y,\gamma_e,\alpha_e)\, \delta_d(x,y,\gamma_e,\alpha_e)}{h(x,y)\ \sum_{\alpha_e} \sum_{\alpha_e} (\omega_e\ \sin\alpha_e)} \quad \textbf{(32)}$$

where h (m) is the total height of the façade stripe. The DSF_{iso} becomes equal to the conventional SVF if the façade stripe collection is queried at a point-level. In such a situation, the DSF_{iso} of a façade point under no obstruction will depend only on its tilt angle (which is $\beta = 90°$). From the popular Liu Jordan model [58], the value of DSF_{iso} for a façade under unobstructed sky would be 50%, as given by Eq. (33):

$$DSF_{iso} = \frac{1 + \cos\beta}{2} = \frac{1 + \cos 90°}{2} = 0.5 \quad \textbf{(33)}$$

4.3 Performance Comparison

4.3.1 Accuracy of Results

Once again, the simulation results obtained from the benchmark model were used as a reference for comparing the accuracy of results from the BRT and FRT beam sub-models. The scenario described in Figure 25 (Chapter 2) was taken into account. For a single instant of time, an isotropic diffuse

potential on the horizontal of 500 W/m^2 was assumed. Since benchmark model as well as the BRT and FRT isotropic diffuse sub-models depends upon the sky discretization resolution, the benchmark model was simulated to obtain the optimum value, which was then used while simulating other sub-models. This was obtained by decreasing the value of the sky resolution, starting from 30° (coarse, having only 36 sky elements) and progressing to 1° (fine, with 32,400 sky elements), as shown in Figure 34. The DSF was obtained for the façade under observation for every value of resolution and the trend was found to become stable for the lower values of resolution. At a value of around 1°, the change in results observed was negligible; however, lower values greatly increased the computation time. Hence, the value of 1° was chosen in order to obtain a good balance between accuracy and computation time.

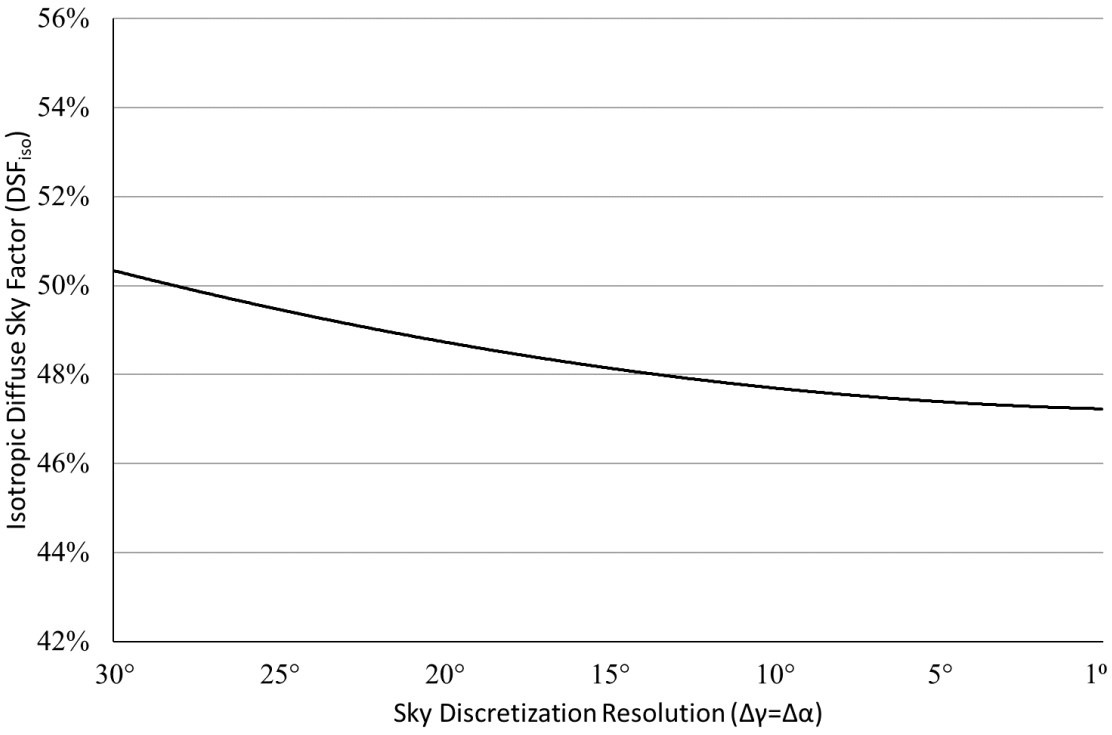

Figure 34: Choosing the optimum sky discretization resolution for the simulations

The benchmark model yielded an instantaneous isotropic diffuse solar potential of 23,640 W. Then the BRT and FRT isotropic diffuse sub-models were simulated while considering the same sky

discretization resolution of 1° that was used for the benchmark model. The BRT isotropic diffuse sub-model yielded 23,419 W, which was 99.06% accurate, at a hyperpoint density of 1.0 point/m. The FRT isotropic diffuse sub-model produced a value of 23 432 W, which was 99.12% accurate, but without discretizing the façade into cells.

4.3.2 Computation Time

The performance of the BRT and FRT isotropic diffuse sub-models in terms of their computation time was compared by recording their simulation times on the same local machine that was used in Chapter 2 (RAM: 32 GB, Processor: 1 CPU x 3.4 GHz). At a sky discretization resolution of 1° and a hyperpoint density of 1.0 point/m, the BRT isotropic diffuse model took 2 hours and 55 minutes to compute firstly, the results at point-level details and then aggregate them for façade-level details. In contrast, the computation time for simulating the FRT isotropic diffuse sub-model to yield the same façade level-details, was found to be only 44 minutes and 40 seconds, which was 3.9 times faster.

4.4 Summary

A sub-model for estimating the isotropic diffuse solar potential of façades using the 2.5D DEM, compatible with the discretization-independent FRT-based scanning algorithm, was developed in this chapter. Then, the performances of the BRT and FRT isotropic diffuse sub-models were compared. For the purpose, the benchmark model was used as a reference. Initially, this algorithm was simulated to obtain the optimum value of sky discretization resolution, which was found to be 1°. This was obtained by simulating the benchmark model at different values of resolution and observing the stability in the DSF value. This value was used when comparing the sub-models. The BRT isotropic diffuse sub-model produced accurate results at a hyperpoint density of 1.0 point/m, whereas the FRT isotropic diffuse sub-model responded with nearly the same accuracy but without discretizing the façade into cells. Comparing computation time, the FRT isotropic diffuse sub-model was found to be

3.9 times faster than the BRT isotropic diffuse sub-model. A summary of the performance comparison between the BRT and FRT isotropic diffuse sub-models is shown in Table 6.

Table 6: Summary of performance comparison between the BRT and FRT isotropic diffuse sub-models

Isotropic diffuse solar potential assessment	**Benchmark model (Appendix A)**	**BRT isotropic diffuse sub-model (At hyperpoint density of 1.0 point/m)**	**FRT isotropic diffuse sub-model (Proposed)**
Result and accuracy	23 640 W	23 419 W (99.06 %)	23 432 W (99.12%)
Simulation time	Not recorded	2 hours 55 minutes	45 minutes

5

DEVELOPMENT OF ANISOTROPIC DIFFUSE SOLAR POTENTIAL SUB-MODEL

5.1 Introduction

In the previous chapter, a sub-model for estimating the isotropic diffuse solar potential of façades using the 2.5D DEM, compatible with the discretization-independent FRT-based scanning algorithm, was developed. This chapter presents an advance in the diffuse sub-model to evaluate the anisotropic diffuse solar potential on facades, which is generally considered as more realistic. For anisotropic sky conditions, a well-known solar radiance model is integrated. This sub-model is compatible with the proposed FRT algorithm and therefore, it is termed the *FRT anisotropic diffuse sub-model*. Since this

sub-model is based on an FRT algorithm it is independent of the façade discretization. Then, a discussion of the relationship between the performance of FRT isotropic and anisotropic diffuse sub-models is provided.

5.2 FRT Anisotropic Diffuse Sub-model

In the previous chapter, the magnitude of radiance was treated as a constant due to the assumption that sky diffused radiation was reaching its target isotropically (R_{iso}). However, when the sky diffused radiation is assumed to be anisotropic, the incoming diffuse radiance is composed of three subcomponents, each dominating in different regions of the sky. The first subcomponent is the isotropic diffuse radiation, which is received equally from all elements. The next is the horizon brightening subcomponent, which is concentrated near the horizon and is most pronounced in clear skies with unobstructed views. The last is the circumsolar subcomponent, which is concentrated in the region of the sky around the sun. To obtain the anisotropic diffuse radiant flux at the façade stripe ($I_{d,aniso}$), the magnitude of each radiance ($R_{aniso}(\gamma_e, \alpha_e, \tau)$) should be represented by a model that considers the instantaneous circumsolar and horizon brightening subcomponents together with the isotropic subcomponent. The modified version of Eq. (27) that operates under such sky assumptions is shown in Eq. (34):

$$I_{d,aniso}(x, y, \tau) = \sum_{\gamma_e} \sum_{\alpha_e} R_{aniso}(\gamma_e, \alpha_e, \tau)\ \omega_e(\alpha_e)\ W\ l_d(x, y, \gamma_e, \alpha_e)\ \delta_d(x, y, \gamma_e, \alpha_e) \quad \textbf{(34)}$$

where the terms ω_e, l_d and δ_d can be obtained from the knowledge presented in the previous chapter, while the magnitude of the radiances, associated with the angular positions of sky elements, can be obtained using the Brunger and Hooper model [79], given by Eq. (35):

$$R_{aniso}(\gamma_e, \epsilon_e, \tau) = I''_d(\tau)\ f_{BH}(\gamma_e, \epsilon_e, \tau) \quad \textbf{(35)}$$

where ϵ_e is the complementary angle of α_e (i.e. $\epsilon_e = 90° - \alpha_e$), and $f_{BH}(\gamma_e, \epsilon_e, \tau)$ is defined by Eq. (36):

$$f_{BH}(\gamma_e, \epsilon_e, \tau) = \left[\frac{a_o + a_1 \cos \epsilon_e + a_2 \exp(-a_3 \psi)}{\pi(a_o + 2a_1/3) + 2a_2 I(90 - \alpha_b, a_3)}\right] \quad \textbf{(36)}$$

where in the numerator, the first term (constant) in the square bracket represents the isotropic diffuse subcomponent, the cosine term takes into account the horizon brightening subcomponent and the circumsolar subcomponent is modelled as an exponential decay as it decreases rapidly with angular distance from the solar disk. The assignable values for the parameters a_0, a_1, a_2 and a_3 that allow the sky radiance model to respond to the atmospheric radiation conditions are tabulated in Table 2 in [79] (a copy of which is available in Appendix B).

The ψ in Eq. (35) is the angle between the direction of the element and the sun, given by Eq. (37), and I_{BH} is given by Eq. (38) [79]:

$$\psi(\gamma_e, \epsilon_e) = \cos^{-1}(\sin \epsilon_e \cos \alpha_b \cos(\gamma_e - \gamma_s) + \cos \epsilon_e \sin \alpha_b) \quad \textbf{(37)}$$

$$\begin{aligned} I_{BH}(90 - \alpha_b, a_3) \quad & \textbf{(38)} \\ &= \frac{[1 + \exp(-a_3 \pi/3)]}{a_3^{2+} + 4} \\ &\times \left\{ \pi \right. \\ &- \left[1 - \frac{2[1 - \exp(-a_3 \pi)]}{\pi a_3 [1 + \exp(-a_3 \pi/2)]}\right] \\ &\times \left. \left[\frac{\pi(90 - \alpha_b) \cos \alpha_b}{90} - 0.02\pi \sin\big(2(90 - \alpha_b)\big)\right]\right\} \end{aligned}$$

where γ_b and α_b are the azimuth and altitude angles of the sun as previously described in Figure 28.

By substituting Eq. (35) in Eq. (13) and simplifying, the following relation is obtained:

$$\frac{I_d(x,y,\tau)}{I_d''(\tau)} = \sum_{\gamma_e}\sum_{\alpha_e} f_{BH}(\gamma_e,\alpha_e,\tau)\ \omega_e(\alpha_e)\ W\ l_d(x,y,\gamma_e,\alpha_e)\ \delta_d(x,y,\gamma_e,\alpha_e) \quad \textbf{(39)}$$

Similar to Eq. (32) in Chapter 4, the DSF_{aniso} can be obtained by dividing Eq. (39) by the area of the stripe, such that:

$$DSF_{aniso}(x,y,\tau) = \frac{\sum_{\gamma_e}\sum_{\alpha_e} f_{BH}(\gamma_e,\alpha_e,\tau)\ \omega_e(\alpha_e)\ l_d(x,y,\gamma_e,\alpha_e)\ \delta_d(x,y,\gamma_e,\alpha_e)}{h(x,y)} \quad \textbf{(40)}$$

Unlike Eq. (30), the right-hand side of Eq. (40) is not entirely spatial because of the f_{BH} term, which has a temporal dimension. This means that, when evaluating the radiant energy over a specific time span, scanning would be required for every instant of time (e.g. every hour) before integrating the results. This could be extremely time consuming if the assessment's temporal range is, for example, a year. To mitigate this situation, the anisotropic skymap of the site could be used. The skymap represents the accumulated anisotropic radiance values for each sky element, over the given time period i.e. $\sum_\tau f_{aniso}(\gamma_e,\theta_e,\tau)$. The discussion on developing the anisotropic skymap with an example is available in Appendix C.

Finally, the façade stripe anisotropic diffuse radiant energy potential can be obtained using Eq. (41):

$$H_{d,aniso}(x,y) = \sum_{\tau} I_d''(\tau) \sum_{\alpha_e}\sum_{\gamma_e}\left[\sum_{\tau} f_{aniso}(\gamma_e,\theta_e,\tau)\right]\ \omega_e(\alpha_e)\ W\ l_d(x,y,\gamma_e,\alpha_e)\ \delta_d(x,y,\gamma_e,\alpha_e) \quad \textbf{(41)}$$

5.3 Discussion on the Performance of Sub-model

It is prudent that the computation time for both the FRT isotropic and anisotropic diffuse potential assessment sub-models should fundamentally be the same. This is because the main difference between Eq. (31), which is for isotropic diffuse radiation, given in Chapter 4, and Eq. (41), is the term

$\sum_{\tau} f_{aniso}(\gamma_e, \theta_e, \tau)$. Since it would be evaluated before any scanning takes place (through skymap), the number of runs required to solve both the equations should be exactly the same, given that the same sky discretization resolution (e.g.1°) is used. This goes applies to the accuracy as well.

A test was performed to confirm the above argument and the FRT anisotropic diffuse sub-model yielded the same accuracy (99.12%) that was found for the FRT isotropic diffuse sub-model. The whole model took 45 minutes to process and compile results at façade-level details.

5.4 Summary

With this advancement over the sub-model described in the previous chapter, the sub-model can now be used to evaluate the anisotropic diffuse solar potential of façades using the 2.5D DEM. For the purpose, the Brunger and Hooper [79] anisotropic sky radiance model was integrated to respond to the atmosphere-dependent scenarios by considering the solar diffuse fraction, clearness index and the position of the sun in the sky. The sub-model was developed such that it could use the anisotropic skymap, which drastically reduces the overall computation time. Also, the performance of FRT isotropic and anisotropic diffuse potential assessment sub-models is proved to be fundamentally the same.

6

QUERYING

6.1 Introduction

So far, the solar potential assessment model, which comprises FRT sub-models for the beam, isotropic diffuse and anisotropic diffuse solar potential, has been developed, hereafter termed the *FRT model*. The model produce results for façade stripes, but if assessment is required at other spatial levels (e.g. whole façade), *querying* should performed.

In the context of this study, the *level of detail* is the term applied to define the spatial level at which the solar potential assessment results are evaluated or required. There can be a range of such levels. Those that can answer most of the questions from various types of end-users are given in Table 7.

Table 7: Different levels of detail relevant to different end-users and their questions regarding solar potential assessment

Level of Detail	End-users	Questions that can be answered
Point-level	Occupant of an apartment	1. Is the installation of a solar device at some particular location on the façade suitable? 2. What is the best location for installing the solar device?
Façade-level	Potential buyers of an apartment	3. What is the potential of a particular façade? 4. What is the potential of facades facing in a particular direction? 5. Which façade of an apartment has the most potential?
Building-level	Real-estate developers; Building owners	6. What is the potential of a building? 7. Which building has more potential? 8. Can the potential be increased by changing the building design, position or orientation?
Region-level	Government administration; Big real-estate developers	1. What is the potential of a town (or city)? 2. Which town has more potential? 3. Can the potential be maximized by changing the urban design?

The stripe-level details, obtained from the FRT model, can be understood as an intermediate level chosen for evaluating high-accuracy, hyperpoints-independent results that can be obtained at computational speeds several times faster than the BRT model. However, the details at the other levels can be obtained by executing *aggregation* and *decomposition* queries, as can be seen in Figure 35.

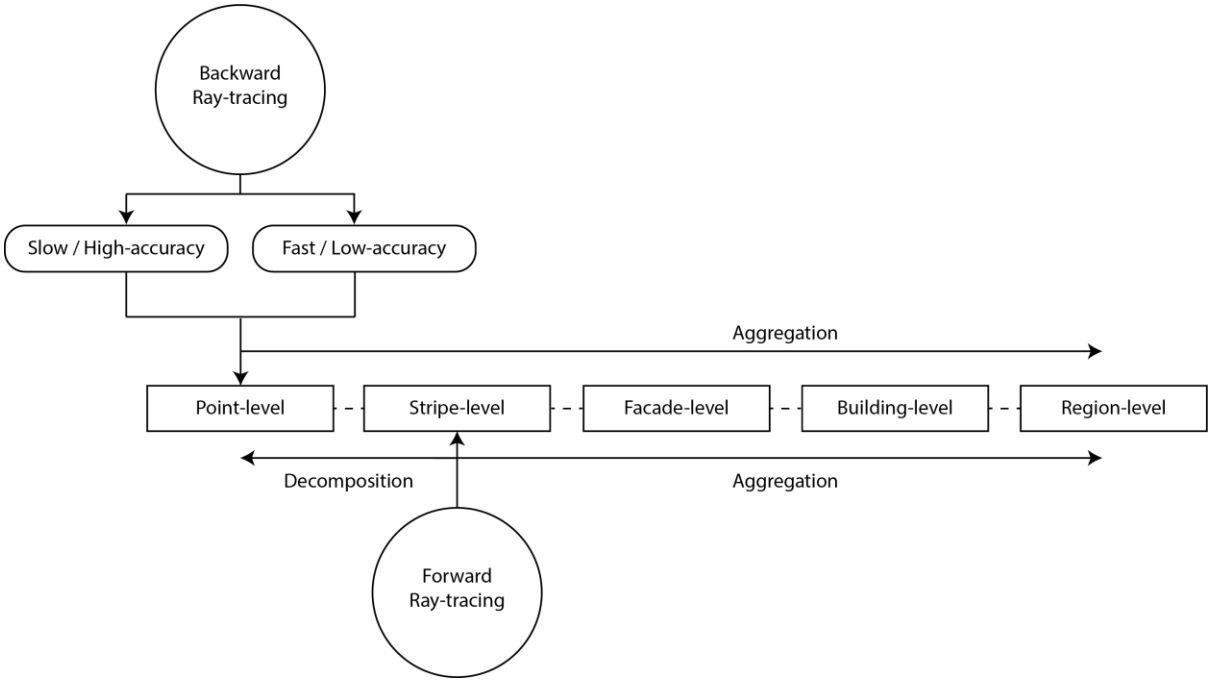

Figure 35: The process of querying

The BRT model, by default, results in point-level details. This seems good, but only as long as the area represented by these hyperpoints (or the hyperpoint density in other words) is carefully selected. Any error at this early stage may be exaggerated when querying for the façade-, building- and region-level details. This is in contrast to the FRT model which results in stripe-level details without the need to determine a hyperpoint density and thus is insensitive to such errors.

One question may arise about comparing the computation time of the FRT model with the BRT model, when results at point-level are required. Of course, the FRT model will take additional time to decompose the results from façade-level to point-level, but to quantify the total computation time for comparison, an appropriate querying method is needed.

Hence, in this chapter, the methods for querying the desired level of detail, starting from the stripe-level of detail, are developed.

6.2 Querying Methods

6.2.1 Aggregation

From the derived stripe-level of detail, different levels of detail, such as façade-, building- and region-level, can be obtained by aggregating the results spatially. This firstly requires the association of each façade stripe with the façade, building and region. It can be represented in a similar form to a DEM except that the cell values will symbolise the addresses rather than the stripe height. This is illustrated in Figure 36.

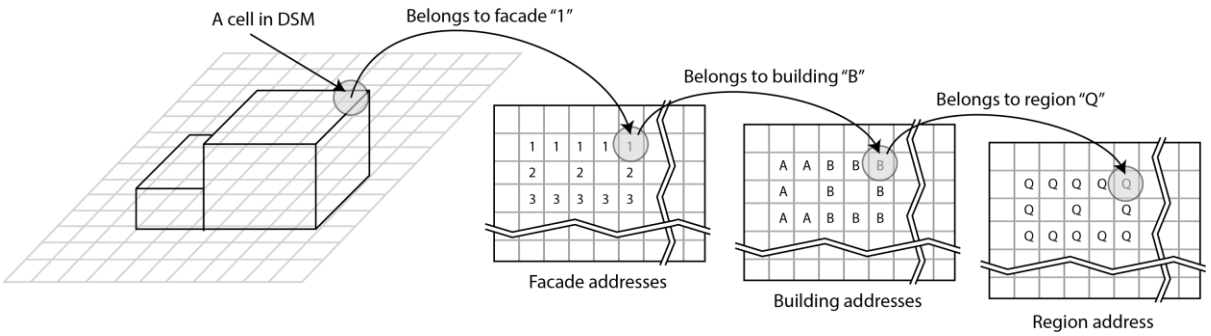

Figure 36: A variation of DEM representing the association of a stripe with façade, building and region, given by their unique addresses

So, for example, finding the total lit area of a particular façade will require stripe-wise aggregation of all the lit heights for the stripes that belong to that façade. As another example, if the beam radiant flux of a building is required, the radiant fluxes of all the stripes that are associated with that building should be aggregated. A similar approach can be used for obtaining the radiant energy.

6.2.2 Decomposition

For transforming the stripe-level details into finer details; i.e. points-level, the decomposition of stripes into small sections would be required. The number of sections will depend upon the

hyperpoints density (ρ_H, points/meter of façade stripe), such that there would be $P = l(x,y) \times \rho_H$ sections, where l represents the height of a façade stripe at (x,y). If p is the numberth section $(= 1,2,3,\dots,P)$ on a façade stripe, having the elevation of its associated hyperpoint in its middle (u_p), then a binary function, $v(x,y,p)$, that can output about whether that section is lit $(= 1)$ or in shadow $(= 0)$, as graphically illustrated in Figure 37, can be written as Eq. (42):

$$v(x,y,p) = \begin{cases} 1, & u_p > s(x,y) \\ 0, & u_p \leq s(x,y) \end{cases} \quad \textbf{(42)}$$

where $s(x,y)$ is the shadow height and the elevation of the associated hyperpoint can be obtained using:

$$u_p = \frac{1}{\rho_H}\left(p - \frac{1}{2}\right) \quad \textbf{(43)}$$

The terms in Eq. (42) may also have temporal (τ) or sky element (α_e, γ_e) related dimensions, depending upon the nature of the analysis.

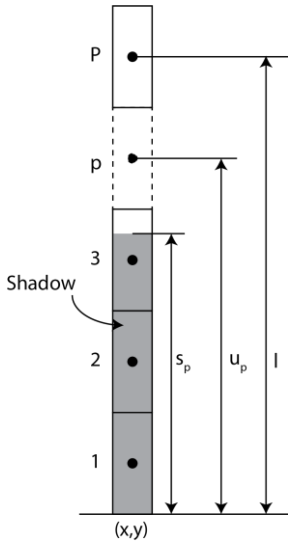

Figure 37: Illustration of elevation of hyperpoints and shadow height

The binary function, together with the hyperpoints density, is used in evaluating the radiant flux and radiant energy of any subdivided section (or hyperpoint). So, for example, the beam radiant flux of section p at hour τ would be:

$$I_b(x,y,\tau,p) = I_b''(\tau)\, W\left[\frac{v(x,y,\tau,p)}{\rho_H}\right] \delta_b(x,y,\tau) \qquad \textbf{(44)}$$

which is a modified version of Eq. (13) in Chapter 3, in which the total lit height has been replaced by the term shown in square brackets. This term has the dimension of length (m) and describes whether the pth section, which has length $1/\rho_H$, is able to receive the radiation or not.

The modification presented above can be deployed in any of the other equations that yield radiant flux or energy. For example, the isotropic Diffuse Sky Factor (DSF_{iso}) at some pth hyperpoint can now be obtained by Eq. (45):

$$DSF_{iso}(x,y,p) = \frac{\sum_{\alpha_e}\sum_{\gamma_e}\omega_e(\alpha_e)\, W\left[\frac{v(x,y,\alpha_e,\gamma_e,p)}{\rho_H}\right] \delta_d(x,y,\alpha_e,\gamma_e)}{l(x,y)\ \sum_{\alpha_e}\sum_{\gamma_e}(\omega_e\ \sin\alpha_e)} \qquad \textbf{(45)}$$

which is the modified version of Eq. (32) in Chapter 4.

6.3 Computation Time

6.3.1 Aggregation

To record the aggregation times, the simulations were performed on the same local machine that was used in Chapter 2 (RAM: 32 GB, Processor: 1 CPU x 3.4 GHz).

For the FRT beam sub-model, simulated for a single instant of time, the aggregation took 0.2 ms, which was negligible compared to the time required for generating the results at the default stripe -

level, which was 86 ms. The main reason was that in aggregation, no scanning was performed, and the results obtained at the stripe-level of detail were merely summed up.

Similarly, the aggregation took < 1.0 sec for simulation performed using the FRT beam sub-model for assessing the annual beam potential. Once again, it was negligible compared to the time required for generating the results at the default stripe-level, which was 3 minutes and 20 seconds.

Lastly, the aggregation took < 10 sec when the results obtained from the FRT isotropic diffuse sub-model were integrated. Yet again, it was trivial compared to the time required for generating the results at the default stripe-level, which was 44 minutes and 40 seconds.

Hence, it can be concluded that the aggregation does not take significant time compared to the computation time for generating results at the default stripe-level. Therefore, the FRT sub-models were proved to be still performing faster than BRT sub-models even when the aggregation time was added.

6.3.2 Decomposition

To record the decomposition times, the simulations were performed for decomposition results from the available stripe-level details to point-level details at a hyperpoint density of 1.0 point/m. The same local machine, as mentioned before, was used for the purpose.

For the FRT beam sub-model, simulated for a single instant of time, the decomposition took 0.9 ms, which was negligible compared to the time required for generating the results at the default stripe-level, which was 86 ms. In contrast, the BRT beam sub-model generated the results at point-level in 341 ms. The main difference in the computation time was because, in the FRT beam sub-model, the task was to check whether each cell under analysis was above or below the lit height whereas in the

BRT sub-model, scanning of the whole DEM in the direction of the light source from each cell was performed.

The decomposition took < 2.0 sec for simulation performed using the FRT beam sub-model for the assessing the annual beam potential. Once again, it was negligible compared to the time required to generate results at the default stripe-level, which was 3 minutes and 19 seconds. The BRT beam sub-model generated the results at the same point-level in 14 minutes and 58 sec.

The stripe-level results obtained from the FRT isotropic diffuse sub-model at the different sky resolutions were converted to point-level details at a hyperpoint density of 1.0 point/m. While querying for each sky resolution, the time was recorded and is shown in Table 8. Interestingly, at a sky resolution of 1°, the whole querying time was only 30 seconds. This means that, to obtain the point-level details of diffuse radiation potential, for which the BRT isotropic diffuse sub-model took nearly 3 hours, the proposed model can obtain the same results in only 45 minutes and 30 seconds.

Table 8: Querying time for obtaining point-level details at a hyperpoint density of 1.0 point/m from the façade-level results obtained from the FRT isotropic diffuse sub-model

Sky Resolution	Sky Elements	Query Time
10º	3 240	< 1 sec
9º	3 600	< 1 sec
8º	4 050	< 1 sec
7º	4 629	< 1 sec
6º	5 400	< 1 sec
5º	6 480	< 10 sec
4º	8 100	< 10 sec
3º	10 800	< 10 sec

2º	16 200	< 10 sec
1º	32 400	30 sec

6.4 Summary

The querying methods for aggregating results from stripe-level to façade- , building- and region-levels, and for decomposing the stripe-level results into point-level results were proposed in this chapter. In both the queries, the computation time required for transforming stripe-level details obtained from FRT sub-models into other level of detail was negligible compared to the time taken by the sub-models to generate the results at default level. Also, the FRT sub-models were found to be performing several times faster when producing and querying results at the point-level of detail compared to the BRT sub-models.

7

COMPUTATIONAL PROCESS MANAGEMENT

7.1 Introduction

In Chapter 1, it was concluded that there are only a few solar potential assessment models that incorporate the management of computational processes but they can work only with BRT models. After developing the FRT model in previous chapters, this chapter therefore focuses on proposing a compatible computational process management method based on scalable architecture. The computation time, with and without deploying this advancement, was recorded for comparison purposes.

7.2 Scalable architecture

7.2.1 Scalability

Scalability can be defined as the ability of a computing system to handle a growing amount of work by adding resources to the system [157]. In general, scalable computing systems, based on any parallel architecture, are efficient and offer high performance in a predictable way [158]. Scaling can be broadly classified into two types, vertical scaling and horizontal scaling [159]. Vertical scaling refers to the capability of a system to allow the addition or removal of resources (such as CPU, RAM, and storage capacity) in a single computer machine. Usually, sequential algorithms, which the majority of algorithms are, do not require any changes when vertical scaling is applied. However, replacing the entire computer with a more powerful computer or adding more resources to the existing computer not only exponentially raise costs but are sometimes very time-consuming as well. With the advent of gigantic *cloud* computing environments such as Amazon Web Services [160], Google Cloud Platform [161] and Microsoft Azure [162], vertical scaling has become less problematic than before. The systems can now be scaled to the requirements by choosing from a range of pre-configured machines and the setup is ready in just a couple of minutes.

In contrast, horizontal scaling refers to the ability of a system to allow a task to be distributed physically (among processors or network nodes) or virtually (using multi-process or multi-threading approaches). Unlike vertical scaling, horizontal scaling largely requires transformation of a sequential algorithm into its equivalent parallel version, which adds many complications in code management, deployment and maintenance. However, the application of such scaling in building high-performance computing systems greatly reduces the need for expensive supercomputers. In fact, horizontal scaling is the only possible way of increasing the capacity of the overall system when it has reached its maximum possible technological limits, vertically.

Multi-process is an efficient way of doing horizontal scaling. In this approach, different instances of the same program are executed in the same machine. On one hand, such a method offers complete liberation from the network-related delays that can occur during task distribution and while compiling the end results over a network. On the other hand, due to the limitation of physical resources, there is always an upper limit to the number of instances that can be initiated. However, this is the cheapest way of deploying horizontal scaling in a system if the requirements are met within the available resources.

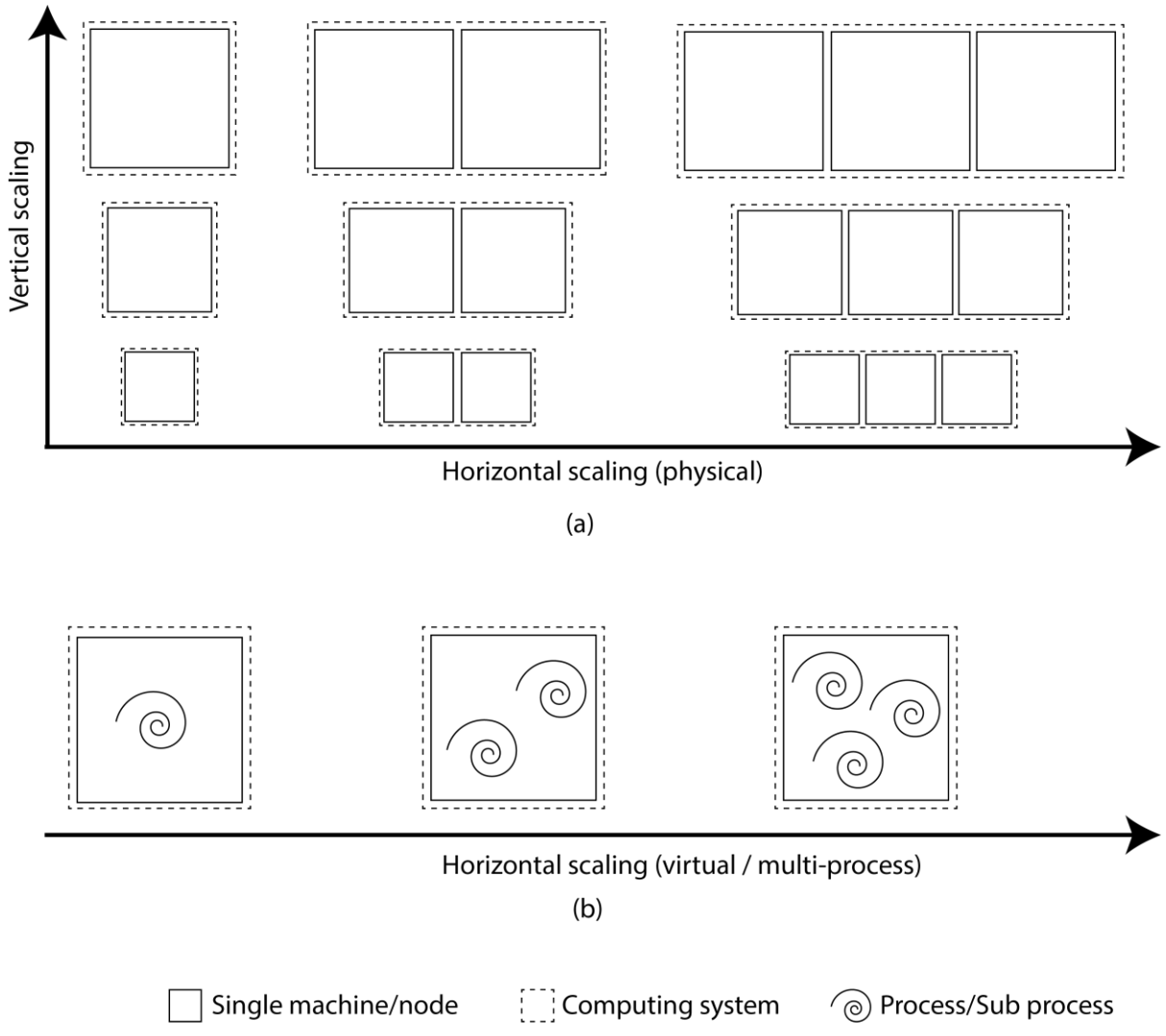

Figure 38: Scaling (a) Vertical and horizontal (physical) scaling; (b) Horizontal scaling using virtual/multi-process

Here, a multi-processing architecture for executing the FRT algorithm is presented. Such an architecture adds horizontal scaling capabilities in the computational process. Then, its implementation in the cloud computing environment is illustrated, to demonstrate its vertical scaling possibilities.

7.2.2 Vertical Scaling

The Amazon Elastic Compute Cloud (EC2) [163], which is the part of the Amazon Web Services cloud (commonly known as the AWS cloud) [160] was used to observe the effects of vertical scaling on scanning performance. The service provides complete control over configuring the computing resources of machines using an interactive web interface. The required system specifications can be chosen from a wide range of pre-configured combinations that are suitable for general-purpose to accelerated computing applications [164, 165]. The service is priced according to Amazon's pay-as-you-go model, which bills on per-second usage. Also, the pricing includes the cost to run the hardware as per its capacity, operating system and on-demand software [166].

The computing configuration used in this case was *m5.4xlarge*, which was tested and compared with the local machine performance. It is the new generation of general-purpose hi-end configurations and is popular for its uses in data processing, cluster computing, small- and medium-sized databases, and backend servers. For their web service, the machine does not allow more than 5 concurrent connections at a time. Table 9 shows the configuration of the local machine for comparison purposes. The web server configured at the local machine had no limitation on the number of connections.

Table 9: The two configurations used for testing and comparing the vertical scaling

Configuration name	Memory (RAM)	Processor	Maximum processes (M_{max})	Programming Language
M5 General Purpose Quadruple Extra Large (m5.4xlarge) [165]	64 GB	16 x CPUs (3.1 GHz each)	5	php 5.5.0
Local machine	32 GB	1 x CPU (3.4 GHz)	Infinite	

7.2.3 Horizontal Scaling

In general, horizontal scaling architectures require a *distributor* that divides the processes into sub-processes, which are then initiated in an asynchronous manner. The algorithm for a multi-process distributor for performing the scanning of large DEMs is illustrated in Figure 39. Initially, the distributor reads the list of illumination angles (pairs of altitude and azimuth angles) to be scanned. It then sets up the directory where each individual *process* will be storing the results for scans. Then, the maximum/permissible number of processes that can be initiated is set up. For a completely autonomous distributor operation, this value could be set to a large number, because the actual initiation of a process will depend upon the available capacity of the CPU. To determine whether the distributor should continue or stop its execution, it will compare the number of scanned pairs available in the directory with the total number of pairs to be scanned, determined previously. In a situation where further scans will be required, the distributor will first check the possibility of initiating a new process. This is performed by obtaining the CPU utilization percentage (average). The distributor is designed to initiate a new process only when the CPU utilization is below a specified threshold. The processes are executed asynchronously; i.e. in parallel to the distributor and other already initiated processes. The distributor loops back to check the progress of scanning until finished.

An algorithm of a *process* is shown in Figure 40. It begins by reading the DEM and its variations (e.g. showing classification and façade angles). Then it reads the list of all illumination angles that have been requested to be scanned. This is exactly like what was done by the distributor. The reason for performing this step in the process is that both the process and the distributor are loosely coupled; i.e. the distributor is not partitioning the range of angles among the process. This adds flexibility in the system to initialize as many processes as possible on the fly, and/or stop them. So, each process takes responsibility for collecting information about the angles that are to be scanned and checking the status of each angle in terms of whether it requires a scan or not. An illumination angle will not require a scan if it has already been scanned or is undergoing scanning by some other parallel process. To cater for the latter situation, where the illumination angle needs to be skipped by a concurrent process, a file locking method is used [167]. In this method, a file associated with the scanning angle is created with no modification rights at the operating system level, immediately after a decision is made by the process about scanning that angle. So, while scanning, which may take some time, the other processes keep on ignoring that angle as they cannot create the same (locked) file in the directory. After scanning and saving the results, the locked file is deleted by the process as the results file itself is now adequate to provide evidence that the angle has been scanned. The process is looped back after picking the next angle in the list. The process is terminated if there are no angles left to be scanned.

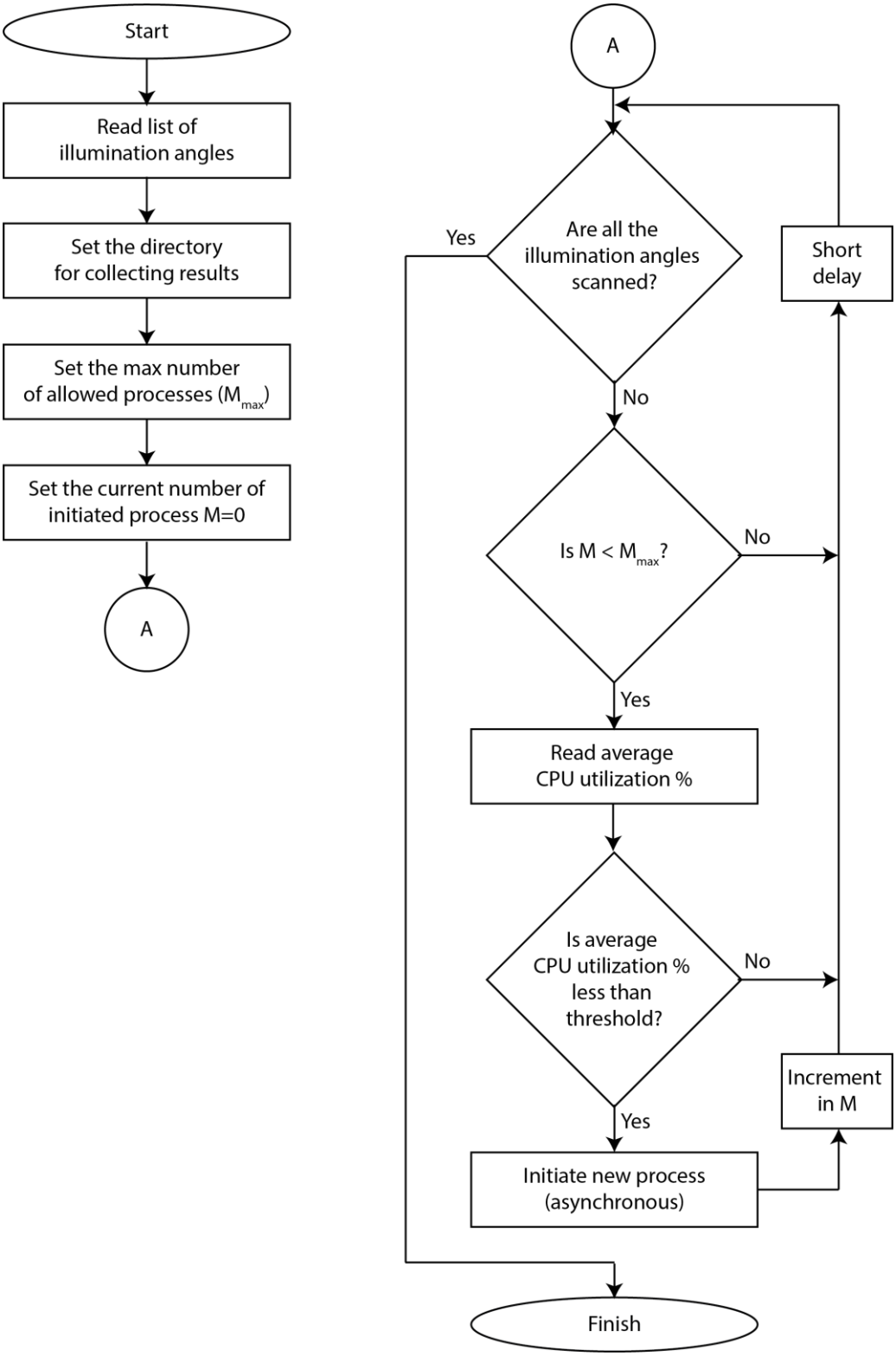

Figure 39: Algorithm of multi-process distributor

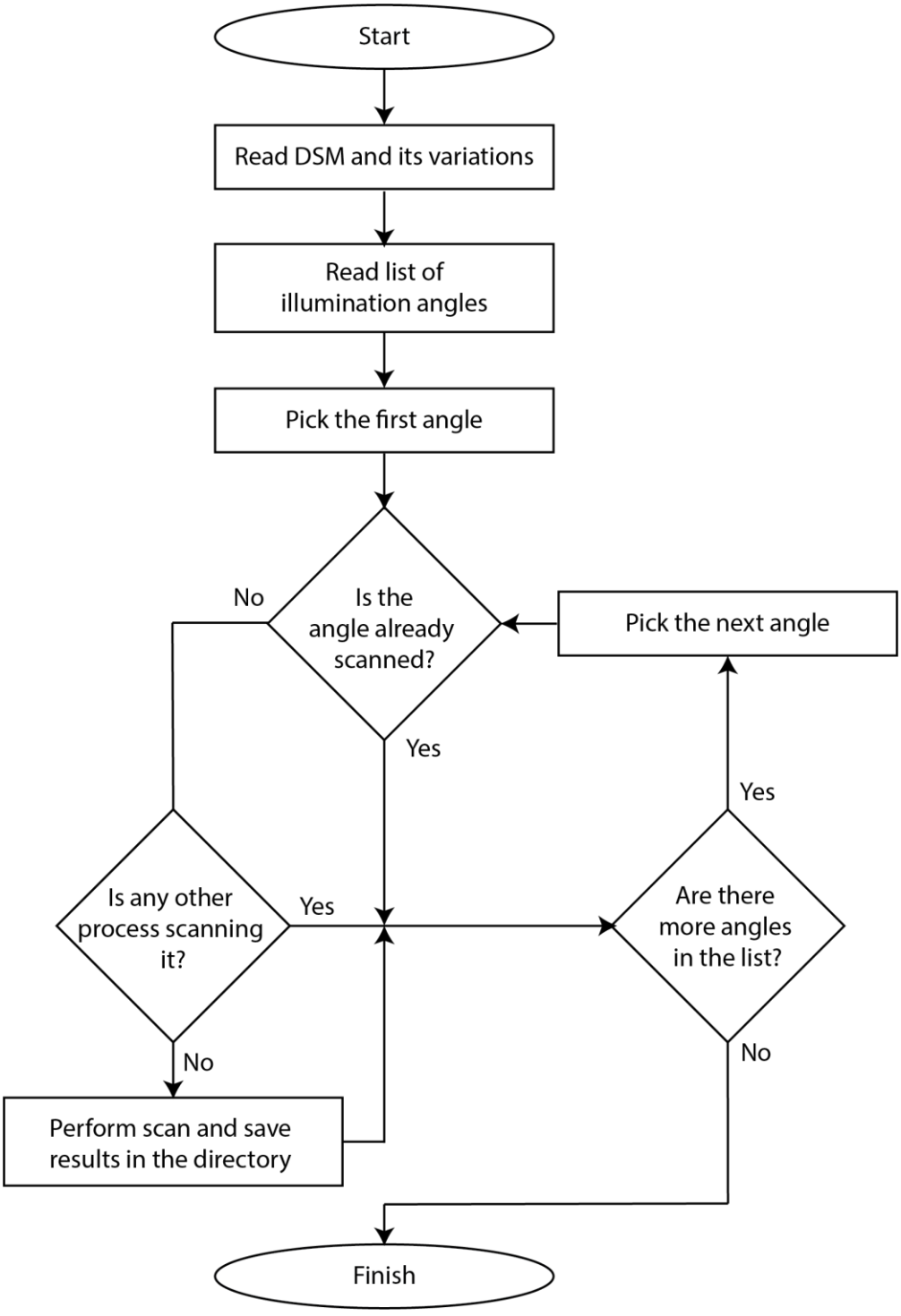

Figure 40: Algorithm of a process in a multi-process initiated asynchronously by the distributor

7.3 Computation Time

As the FRT diffuse sub-model required the greatest computation time compared with other sub-models, this sub-model was selected for testing the deployment of computational process management through scalable architecture.

To deploy the horizontal scaling, the sub-model was transformed into the multi-process architecture. As before, a sky resolution of 1° was selected so that the computation time could be compared with the already performed simulations. Also, for the same reason, the simulations were again performed using the local machine. The distributor was set to initiate a maximum number of processes, starting from 1 and proceeding to an infinitely any value. It was observed that after initiating the 7 asynchronous processes, the average CPU utilization percentage reached 100% and hence the distributor did not begin any new process after that. As expected, the computation time was observed to reduce with an increase in the number of processes. The steepest drop in computation time was found when the second process was initiated. After that, with the initiation of each successive process, the drop became more and more moderate. As can be seen in Figure 41, a dramatic reduction in computation time from 45 minutes to only 27 minutes was achieved, making it 1.7 times faster. This is almost 6.5 times faster as compared to the sequential, BRT isotropic diffuse sub-model, performed on the same local machine.

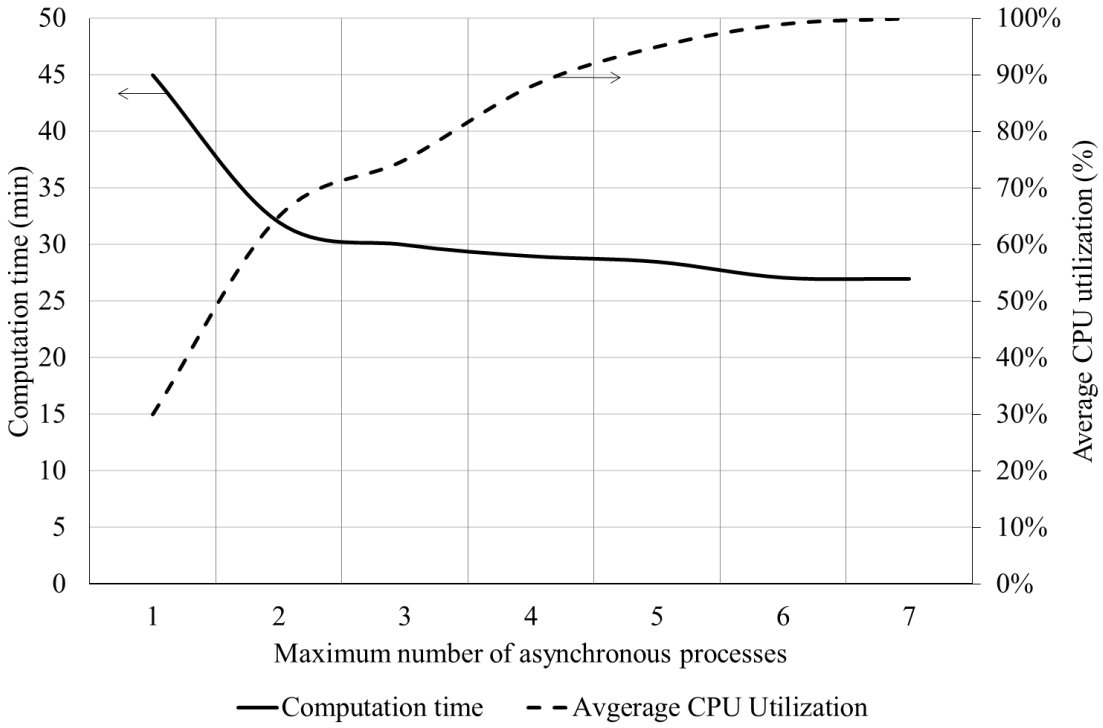

Figure 41: Effect of increasing the permissible number of asynchronous processes on the computation time and the CPU utilization on a local machine when evaluating FRT diffuse sub-model

For testing vertical scaling, the program was hosted in the Amazon Elastic Compute Cloud (Amazon EC2) [163] environment and was simulated under m5.4xlarge configurations. The distributor could initiate 5 asynchronous processes, and it took 11 minutes to complete the task, as shown in Figure 42. This was 2.5 times faster than multi-process using the local machine. Better configurations on the cloud could be rented to increase performance even further.

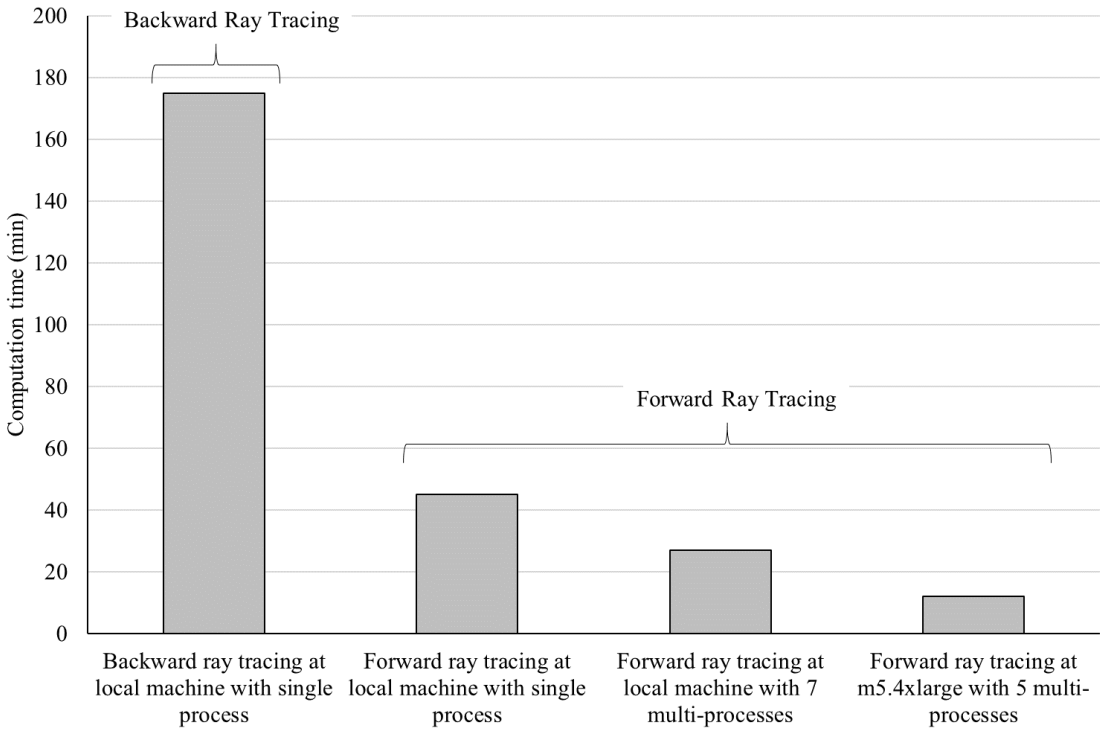

Figure 42: Effects of the different models and testing environments on computation time when evaluating diffuse radiation potential

The contributions of the different techniques applied in reducing the computation time using computational process management are compared in Figure 43. Replacing BRT scanning with FRT contributed 80% of the overall reduction in time required. This was followed by the contribution of adding horizontal scaling, which was found to be 11%. Lastly, moving into the cloud environment for achieving vertical scaling contributed 9% to the overall reduction in computation time.

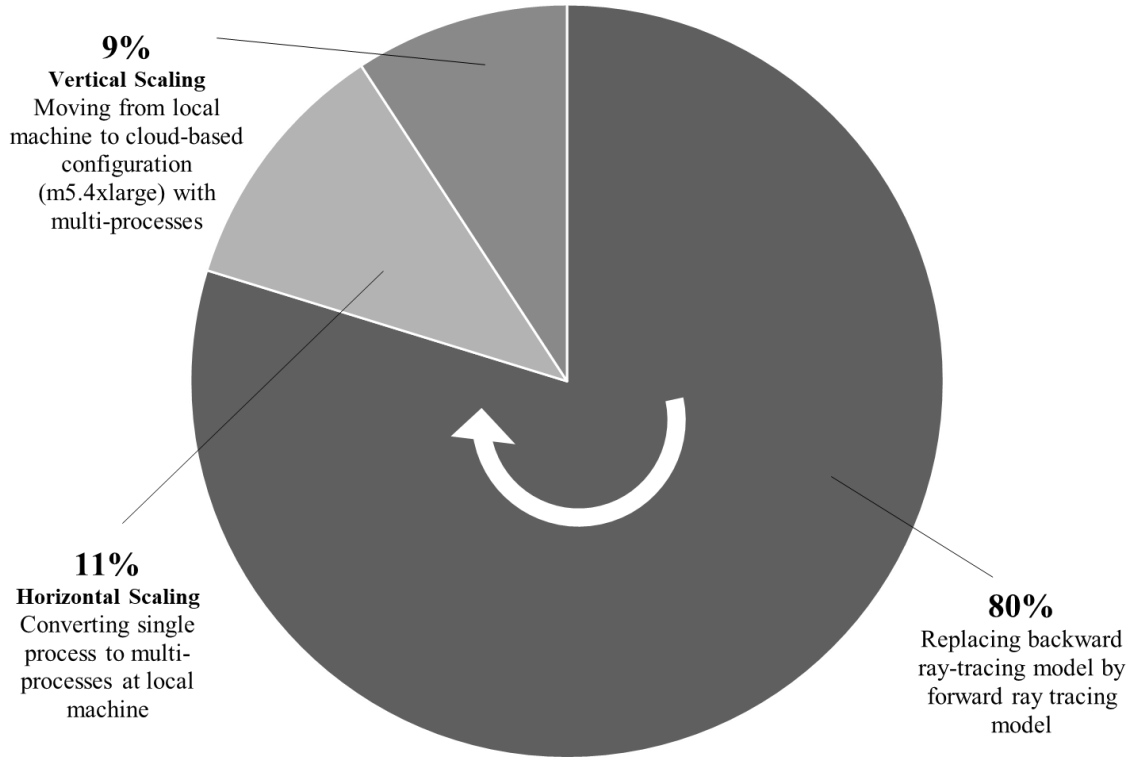

Figure 43: Contribution of the different techniques applied in reducing computation time

7.4 Summary

A compatible computational process management method, based on scalable architecture, was proposed in this chapter. It is compatible with the FRT model, developed in previous chapters. A drastic improvement in computing speed was demonstrated for the FRT isotropic diffuse sub-model. Deploying horizontal scaling led to an 11% improvement in speed, while vertical scaling contributed another 9%.

8

CASE STUDY

8.1 Introduction

In the previous chapter, the proposed FRT solar radiation potential assessment model was demonstrated using a simple layout, which effectively served the purpose of evaluating the accuracy and speed of its scanning algorithm and sub-models compared to the conventional, BRT model. It was concluded that the proposed model yields excellent accuracy without worrying about the hyperpoint density. In contrast, for the conventional model, it is crucial to choose a high hyperpoint density to obtain the same degree of accuracy, which significantly increases computation time.

This chapter describes the implementation of the proposed model for assessing the potential of a real layout. The façade potentials (i.e. beam, diffuse and total) at different spatial levels of detail are computed using both the proposed and conventional models, and their accuracies and speeds are compared. Then, the results obtained are applied to obtain several kinds of valuable information, including the assessment of the technical potential for PV panels and ST collectors.

8.2 AUT City Campus

To illustrate the implementation of the proposed model, the 80,000 m^2 AUT city campus (along with some residential and commercial neighbouring buildings) was chosen as a case study. It is in the heart of Auckland, is the biggest AUT campus, and is home to most academic units and central administration offices [168].

8.3 Elevation Data

The elevation data (including both the surface and terrain) and all the required variations of digital models were developed, as explained in Appendix D. The region of the campus was selected in OpenStreetMap [169], as shown in Figure 44. Some of the views of the layout after extracting façades are provided in Figure 45. The region has a non-uniform terrain, which can be seen in Figure 45 (b and c). The region's façade area was calculated to be approximately 40,000 m^2. The distribution of this area at different elevations from ground is also shown in Figure 46.

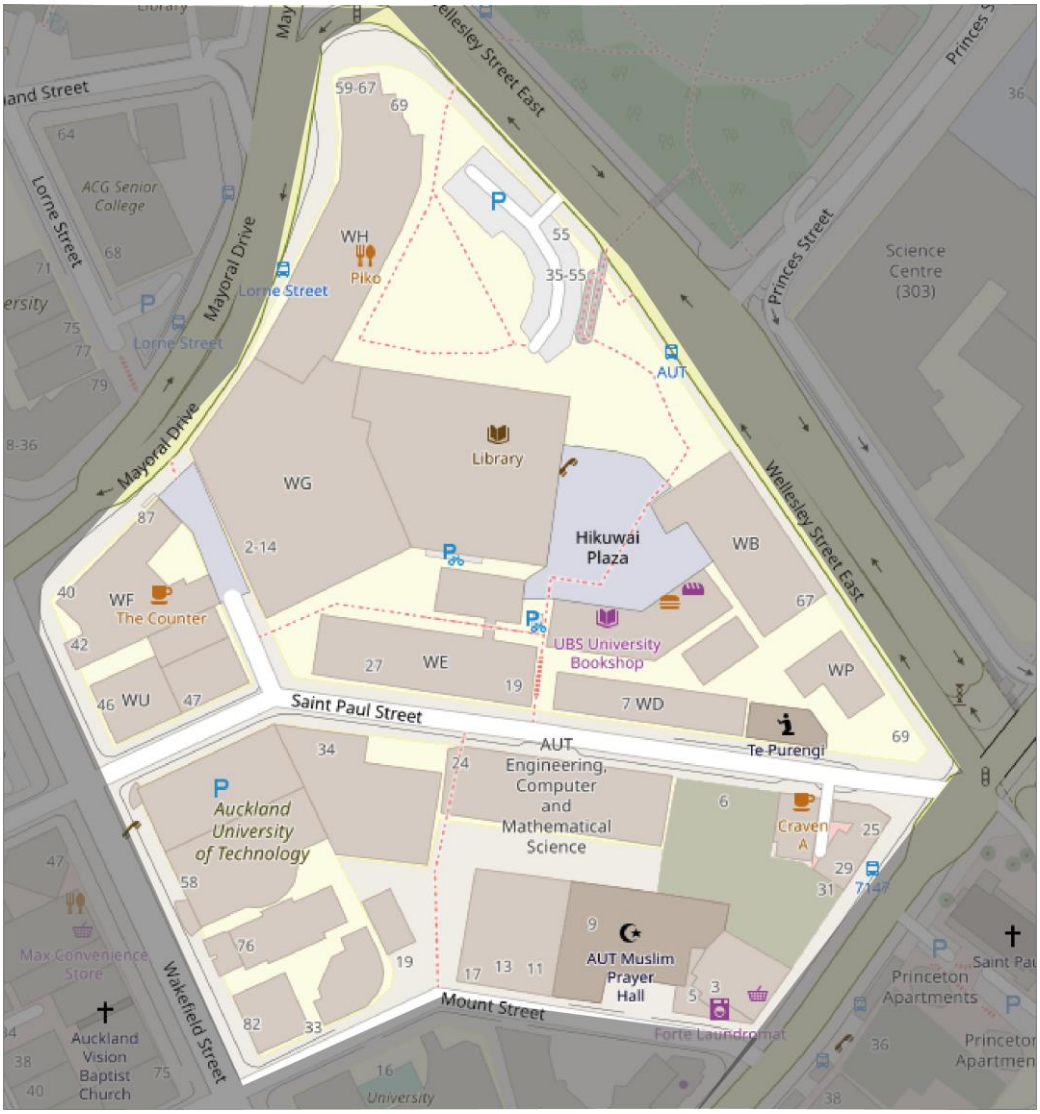

Figure 44: Region of AUT city campus to be analysed, as selected in OpenStreetMap [169]


★ AUT buildings
• Other buildings
Mayoral Drive
Wellesley Street
Wakefield Street
Symonds Street
Mount Street
St. Paul Street
WH
WA
WG
WB
WC
WP
WF
WE
WD
WU
WS
WM
WO
WN

(a)

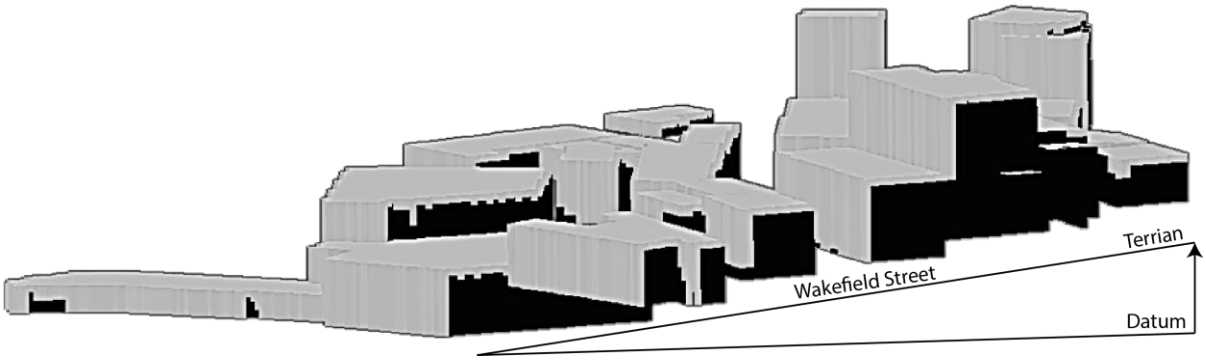
Terrian
Wakefield Street
Datum

(b)

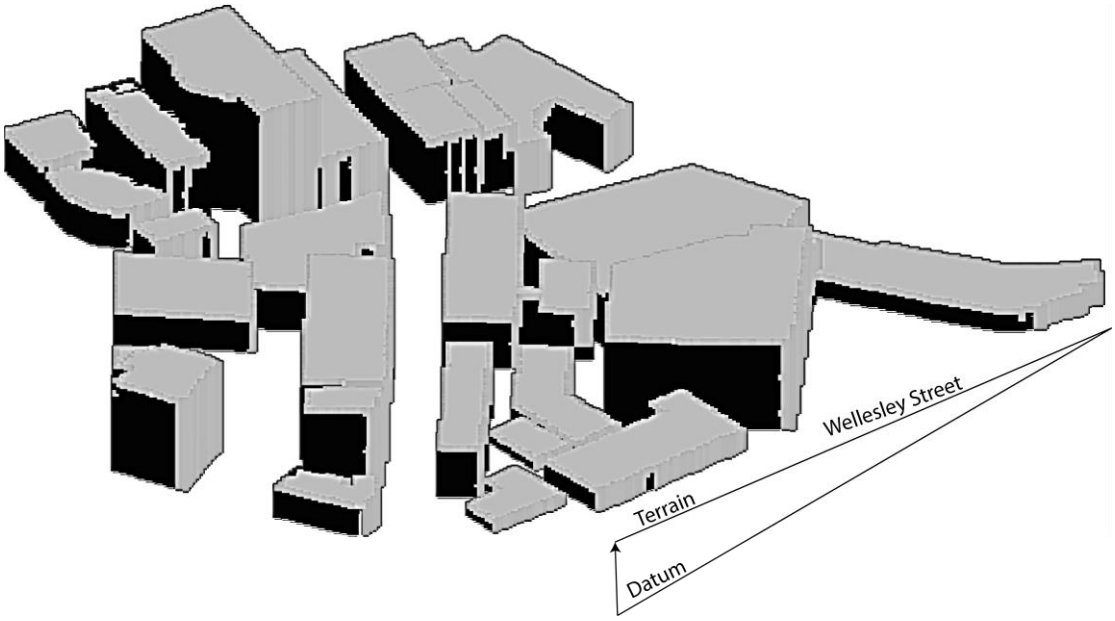

(c)

Figure 45: Views of AUT city campus layout after façade extraction (a) Birds-eye view (b) From Wakefield Street and (c) From Wellesley Street

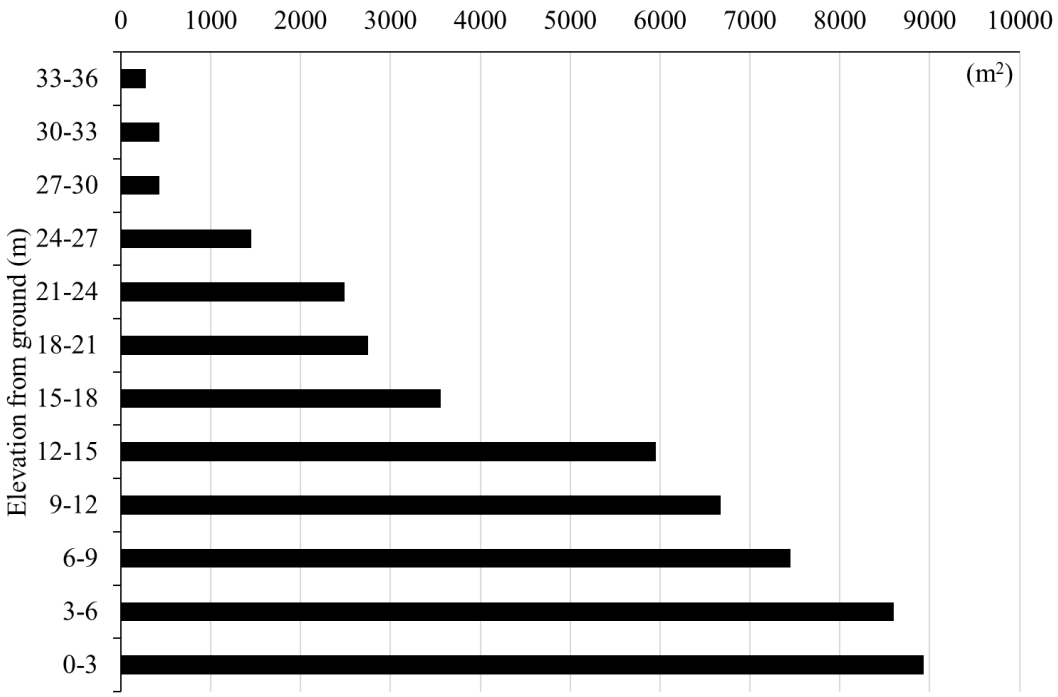

Figure 46: Distribution of façade area at different elevations from ground

8.4 Radiation Potential

8.4.1 Beam Radiation Potential

The proposed model was simulated for an arbitrarily chosen hour of the year ($\alpha_b = 30°$, $\gamma_b = 0°$ and normal irradiance of 2 200 kJ/hr.m^2). The results obtained were at stripe-level, which were aggregated to the region-level potential, yielding 21.8 GJ/hr. The point-level potential at a hyperpoint density of 1.0 point/metre is also shown in Figure 47. The computation times for scanning, evaluating stripe-level results and then aggregation and decomposition were recorded and are provided in Figure 48, which shows that scanning took most of the computation time compared to the other stages.

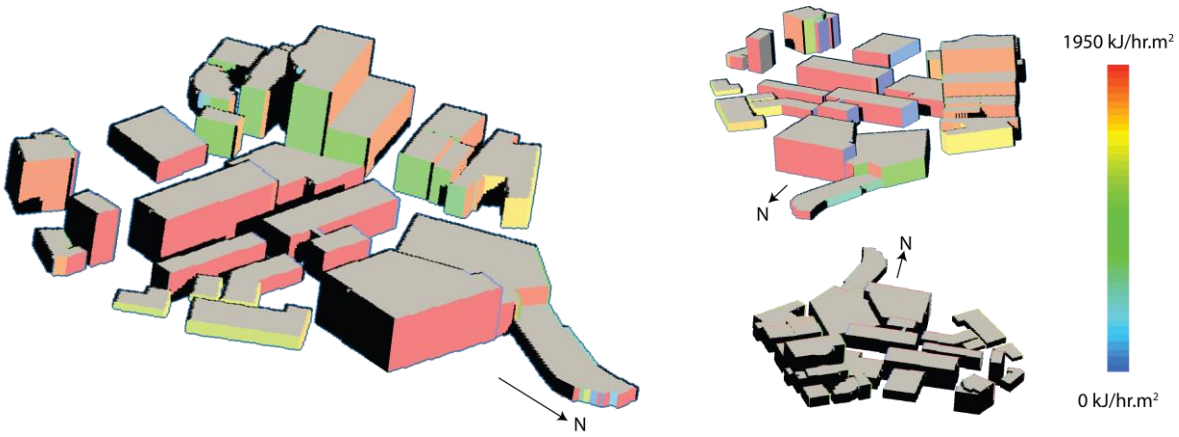

Figure 47: Beam radiation potential at point-level during an arbitrarily chosen hour of the year

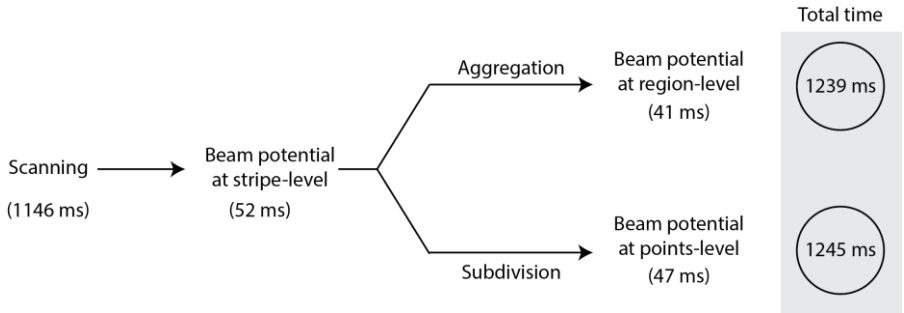

Figure 48: Computation times for assessing the beam radiation potential at region- and point-levels

To obtain the same (or nearly the same) region-level results, the conventional BRT model was simulated at different hyperpoint densities and the computation times were recorded, as shown in Figure 49. At the very low value of hyperpoint density (<0.1), the complete assessment was performed in only 694 ms; however, the error (now defined as the difference between the results and those from the proposed model) was found to be nearly 75%. Increasing the value of hyperpoint density yielded better results but took more computation time as the model had to analyze more points per façade stripe. At the hyperpoint density of 1.0 point/m, the error found was negligible and the computation took 11,986 ms. Increasing the hyperpoint density beyond this value does not affect the accuracy of the result significantly but dramatically increases the computation time. Hence, this value was chosen for the simulations subsequently performed. Using this value, the proposed model was found to be 9.7 times faster than the conventional model.

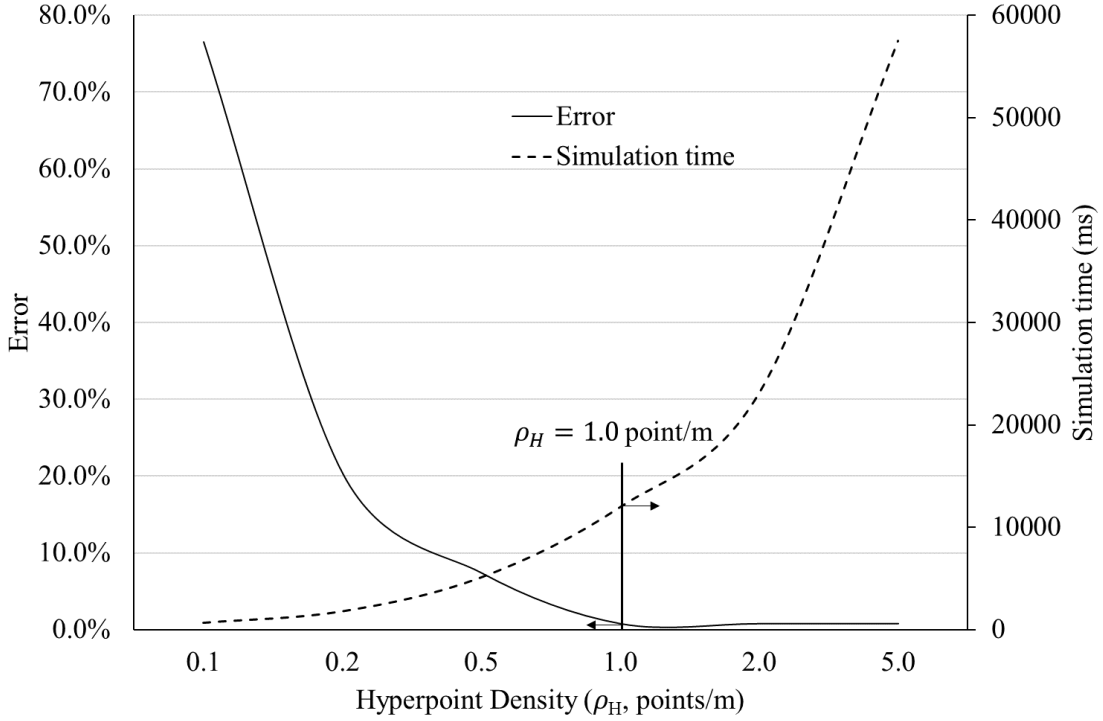

Figure 49: The error and computation time for assessing the beam radiation potential at region-level at different hyperpoint densities using a backward ray tracing-based model

The proposed and conventional models were then simulated to obtain the beam radiation potential of the chosen layout during the whole year. The sun positions and irradiance at different daytime hours of the year were obtained for Auckland from a geolocation-tied database [48]. The region-level potential was found to be 20 622 GJ. The conventional model took 11 hours and 36 minutes to complete the calculations, while the proposed model took only 1 hour and 51 minutes, including scanning and aggregation. Hence, the proposed model was found to be performing 6.3 times faster than the conventional model. The point-level details of the annual beam solar potential are shown in Figure 50.

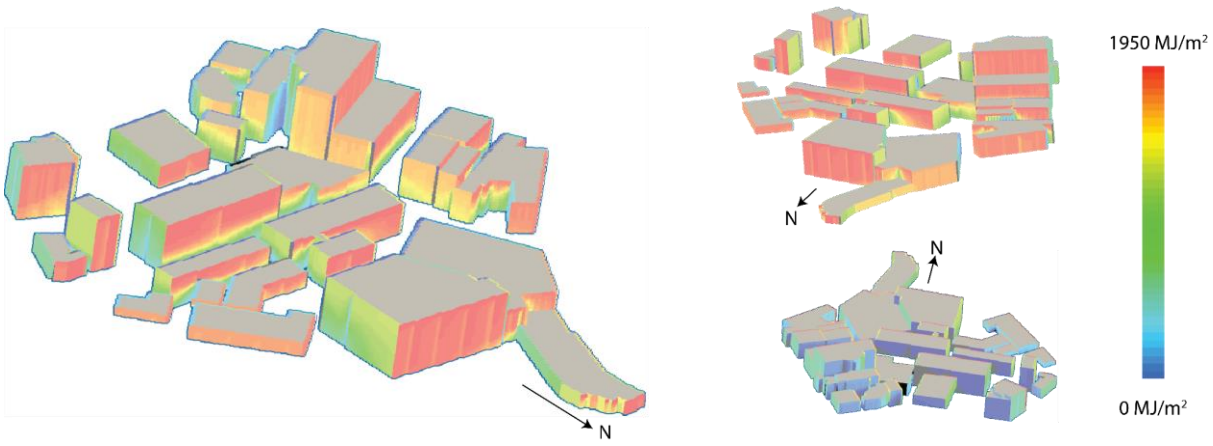

Figure 50: Annual beam solar potential of façades and buildings for the AUT city campus layout accumulated over a typical year

From the rose diagram, shown in Figure 51, it can be seen that the façades facing north or slightly west of north receive most of the beam radiation on a yearly basis. In contrast, south facing façades does not appear to receive significant levels of beam radiation.

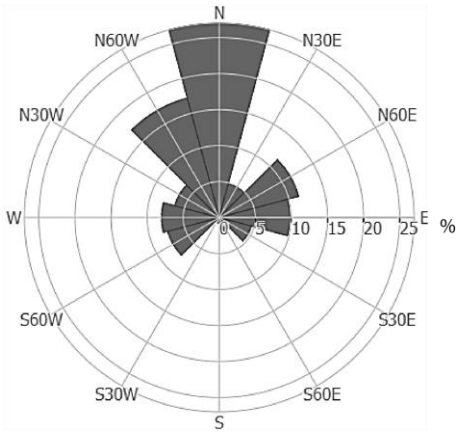

Figure 51: Percentage of yearly beam radiation accumulated on façades in AUT city campus layout facing different directions

Point-level details for the seasonal beam radiation potential were also obtained and are shown in Figure 52. The performance of the façades facing north was found to be greater during winter and autumn. This is because of the low altitude angle of the sun during these seasons. In contrast, the facades facing east and west performed slightly better than the north-facing façades in summer and spring. During these seasons, the irradiation is high at noon (to the north), but the high-altitude angle of the sun negatively affects accumulation. The south-facing façades were found to be barely receiving radiation in any season.

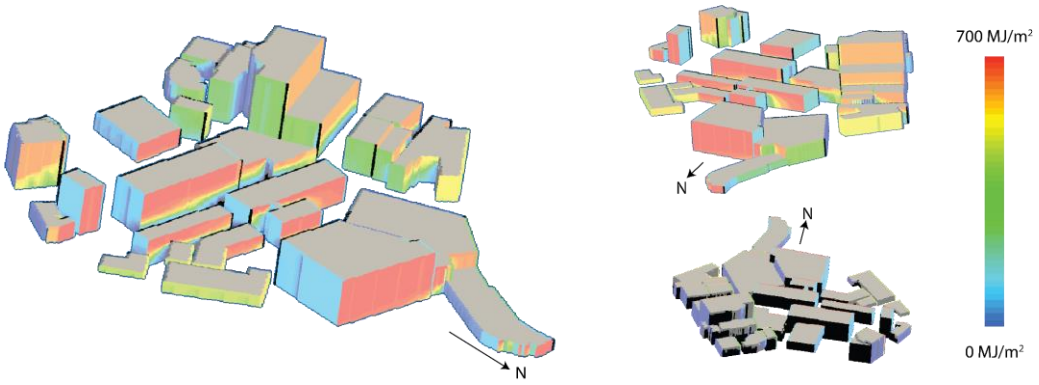

(a) Winter season (December-February)

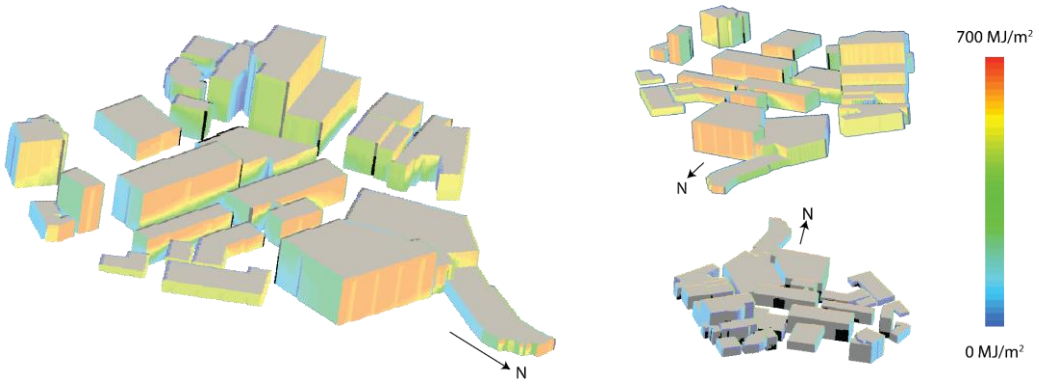

(b) Autumn season (March-May)

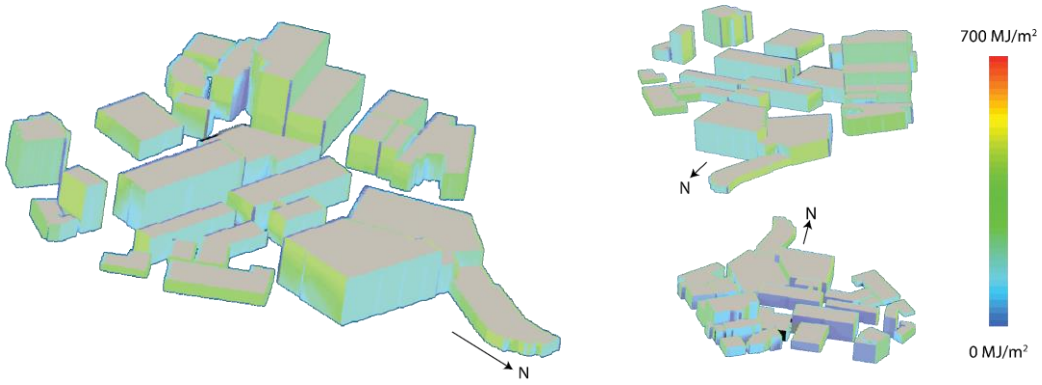

(c) Summer season (June-August)

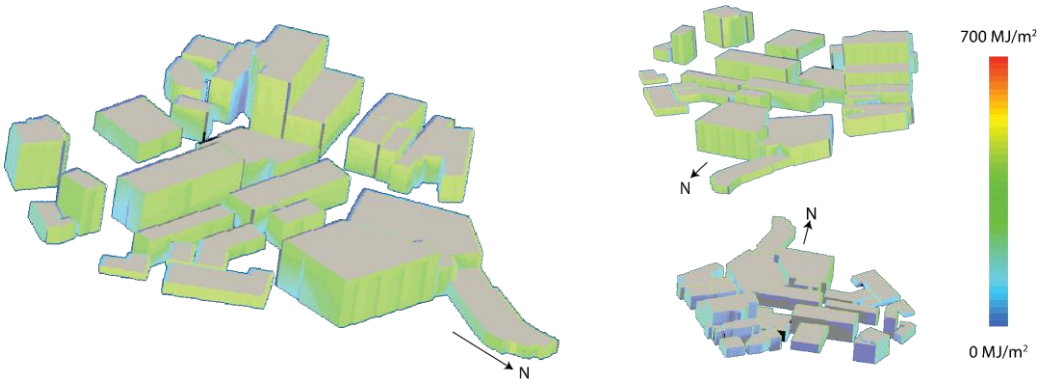

(d) Spring (September-November)

Figure 52: Beam solar potential of façades in the AUT city campus layout during different seasons of a typical year

8.4.2 Isotropic Diffuse Radiation Potential

To obtain the isotropic diffuse radiation potential, a sky discretization resolution of 1º was chosen. This resolution has shown a good balance between accuracy and computation time, as described in Chapter 4. The scanning was performed using the proposed scanning algorithm in 32k directions and the potential at the stripe-level was obtained. This process took 19 hours and 26 minutes on a local machine, 5 hours and 5 minutes on the same machine using a multi-process, and 2 hours and 48 minutes on the cloud-based m5.4xlarge machine with multi-process. The diffuse radiation potential at the region-level was 38 524 GJ for the whole year. The simulations were then performed using the conventional model. At a hyperpoint density of 1.0 point/metre, the annual potential was almost the same as that evaluated using the proposed model. However, the calculations took 4 days 6 hours and 47 minutes, including scanning and aggregation. Speed comparisons are provided in Figure 53, while the contributions of the different techniques applied in reducing the computation time are compared in Figure 54. Replacing BRT with FRT contributed 83% of the overall reduction in time required, making it 5 times faster. This was followed by the contribution of adding horizontal scaling, which was found to be 14%, making it overall ~20 times faster. Finally, moving into the cloud environment

to achieve vertical scaling contributed 3% to the overall reduction in computation time, which made it overall ~37 times faster.

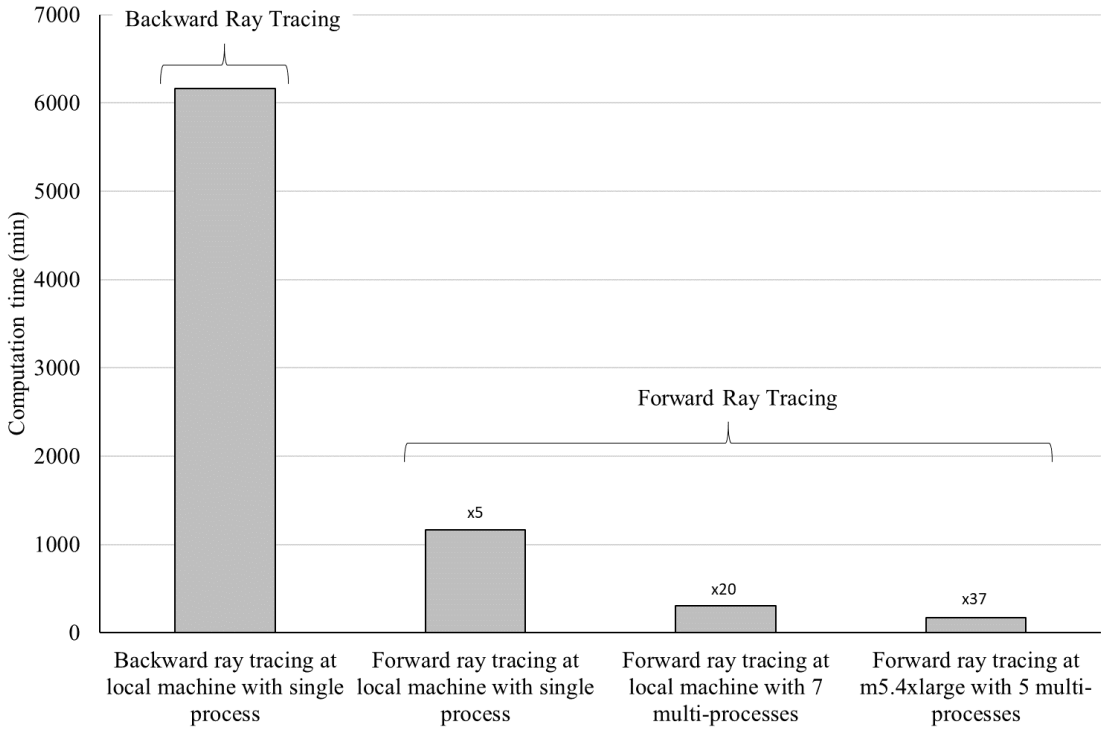

Figure 53: Effects of the different models and testing environments on computation time when evaluating diffuse radiation potential

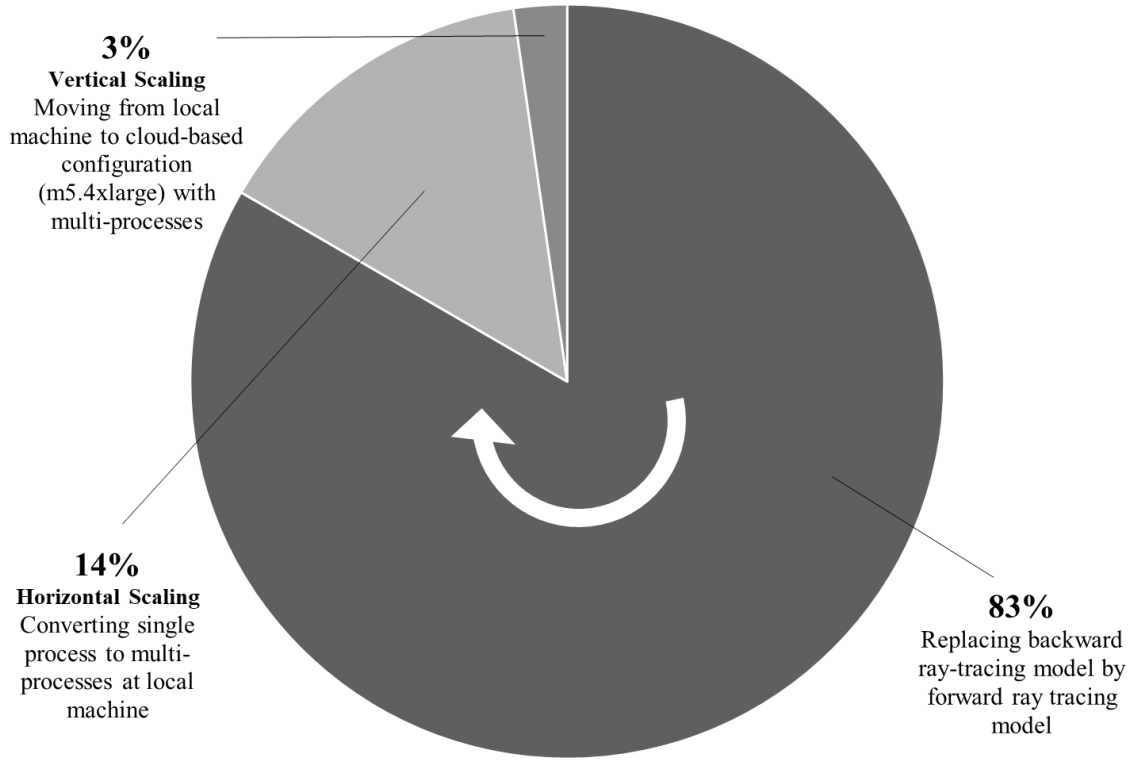

Figure 54: Contribution of the different techniques applied in reducing computation time

The point-level details of the isotropic diffuse potential are shown in Figure 55. Most of the points at the exterior walls of the layout that were not facing any sky obstruction were found to have a DSF_{iso} of 50%, which is the same value of sky view factor as a vertical surface under unobstructed sky (Eq. (33) in Chapter 4). Unlike the beam potential, which depends upon the position of the sun in sky, the value of DSF_{iso} is the same for unobstructed points on facades irrespective of where they are facing. Hence, a significantly high contribution of diffuse potential from the south-facing facades can also be seen in the rose diagram, shown in Figure 56. The points facing an obstructed sky due to the surrounding buildings had lesser values, depending upon the magnitude of the blocked sky radiances. In the rose diagram, shown in Figure 56, the contribution of the north-facing façade is high, showing that the façades facing north have large unobstructed areas compared to the other directions in the chosen layout.

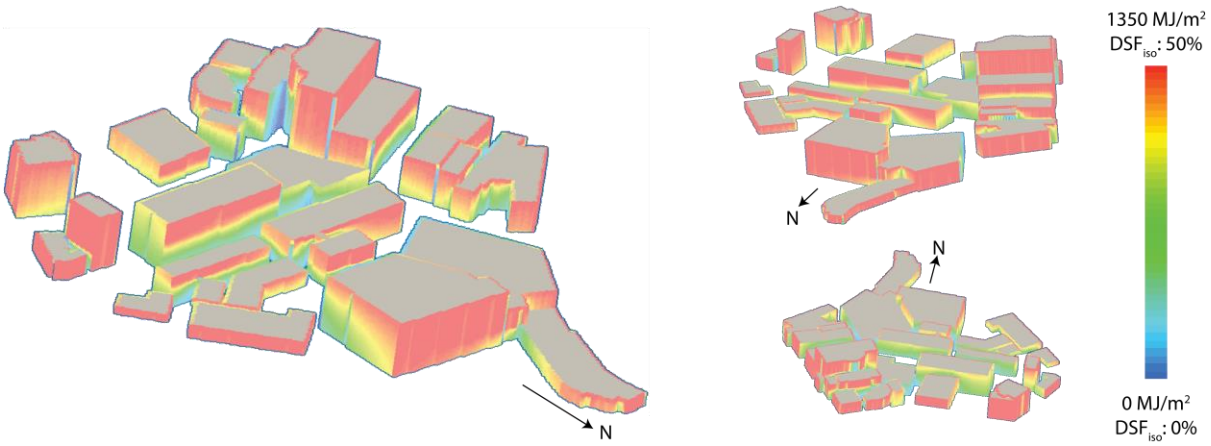

Figure 55: Simulation results demonstrating the isotropic Diffuse Sky Factor (DSF_{iso}) and the diffuse solar potential over a typical year for the AUT city campus layout

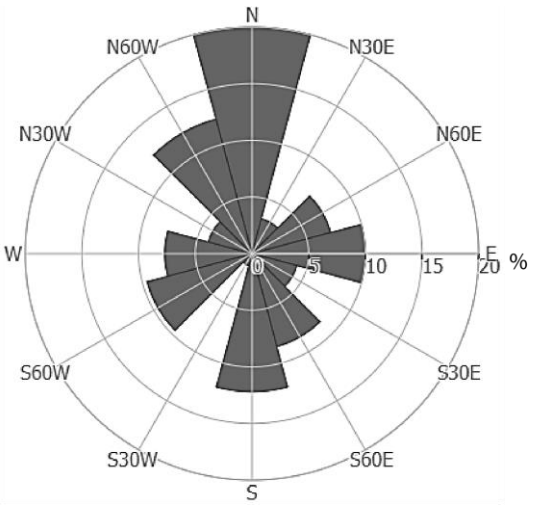

Figure 56: Percentage of yearly isotropic diffuse radiation accumulated on façades facing different directions in AUT city campus layout

The evaluated annual beam potential was combined with the isotropic diffuse potential and the results are shown in Figure 57. The rose diagram is shown in Figure 58. The points on the façades facing north and north-west had the largest contribution to the total solar radiation potential. Façades facing south still received some radiation but were not significant compared to other directions.

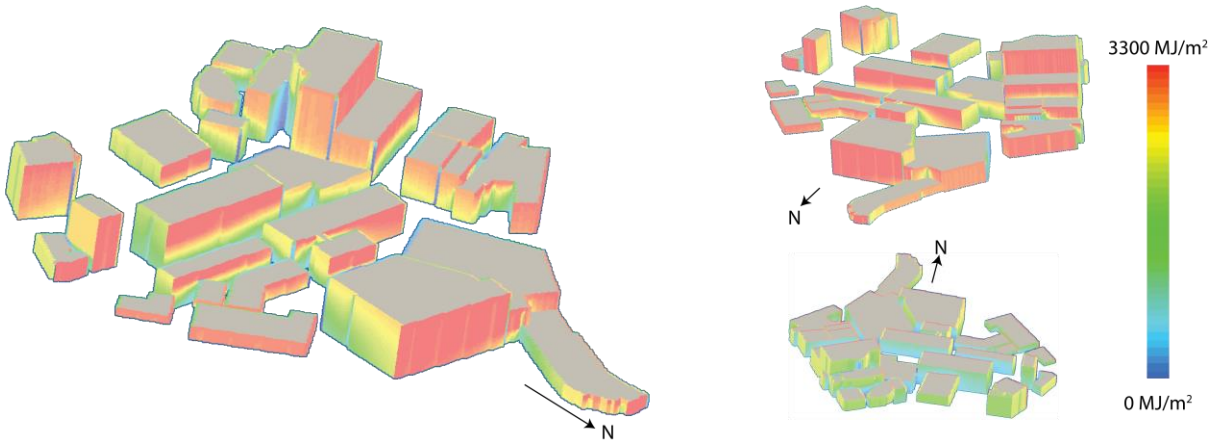

Figure 57: Annual solar energy potential (beam and isotropic diffuse) for the AUT city campus layout

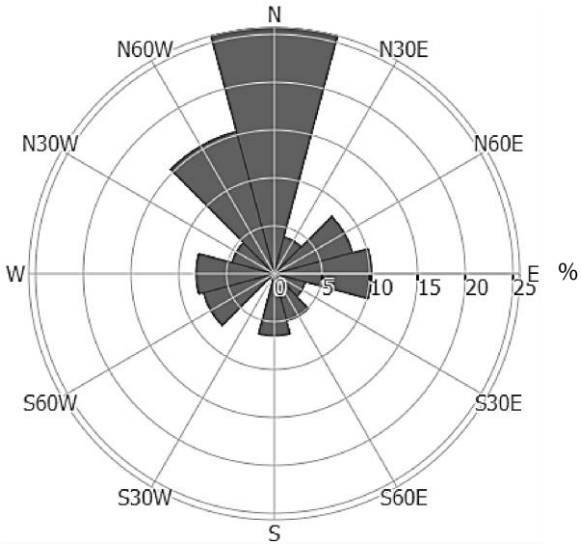

Figure 58: Percentage of yearly total (beam and isotropic diffuse) radiation accumulated on façades facing different directions in AUT city campus layout

8.4.3 Anisotropic Diffuse Radiation Potential

To obtain a more realistic diffuse radiation potential, anisotropic sky conditions were considered. The anisotropic skymap, as described in Appendix C, was used for this purpose. The process took nearly the same time as the evaluation of the isotropic diffuse potential. The anisotropic diffuse radiation

potential at the region-level was 38 469 GJ for the whole year. The point-level details of the anisotropic diffuse potential and the rose diagrams are shown in Figure 59 and Figure 60, respectively.

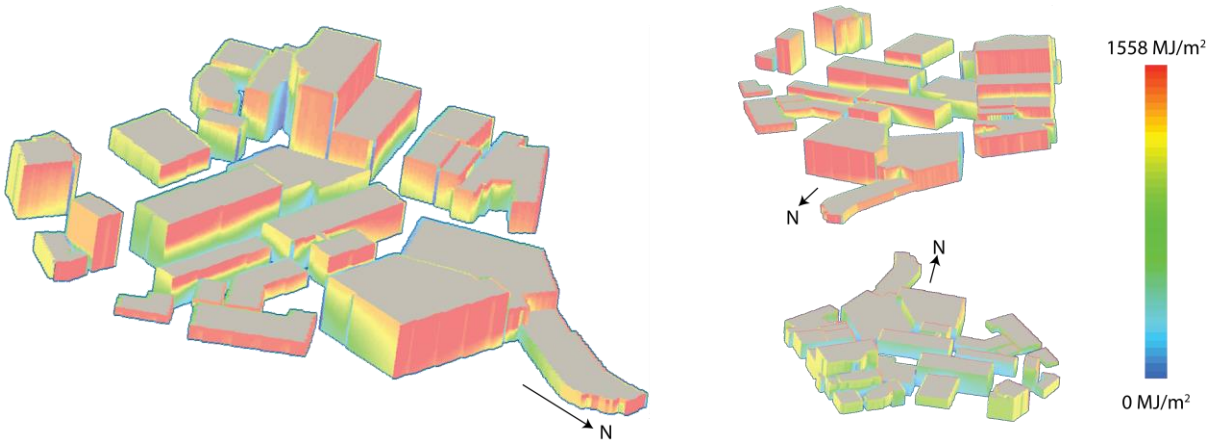

Figure 59: Simulation results demonstrating the anisotropic diffuse solar potential over the year for the AUT city campus layout

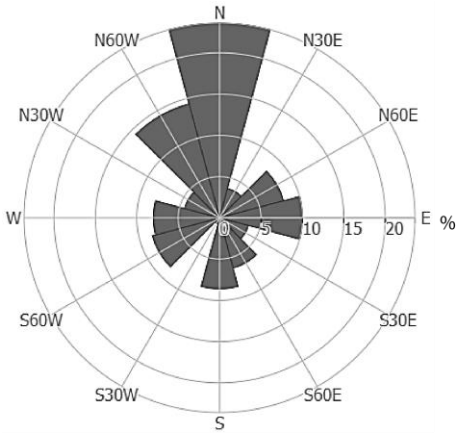

Figure 60: Percentage of yearly anisotropic diffuse radiation accumulated on façades in AUT city campus layout facing different directions

It is interesting to see that the region-level annual potentials are nearly the same in both the anisotropic and isotropic sky conditions. However, the accumulation on facades in different directions is noticeably different. This is illustrated in the rose diagram shown in Figure 61, which represents the

ratio between the anisotropic and isotropic diffuse radiation in specific directions. Between N30W to N60W, the ratio is higher than 1.0, showing an increase in accumulation in these directions when the anisotropic model is used. In contrast, a decrease in accumulation can be seen in the directions between S60W and S30E, as the ratio is less than 1.0. This shift is because the anisotropic model considers the circumsolar brightening subcomponent, which actually behaves similarly to the beam radiation (i.e. having more intensity from the direction in the sky nearest to the position of the sun).

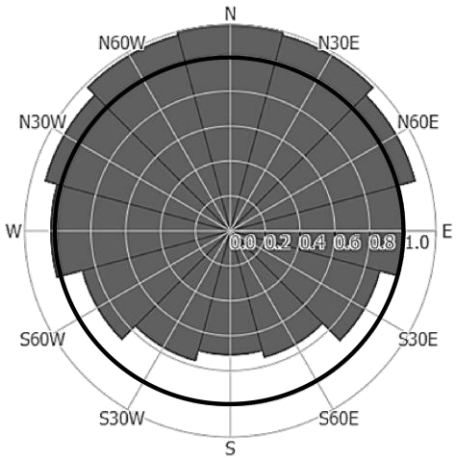

Figure 61: Ratio between the yearly anisotropic and isotropic diffuse radiation accumulated on façades facing different directions in AUT city campus layout

The evaluated annual beam potential was combined with the anisotropic diffuse potential and the results are shown in Figure 62. The rose diagram is also provided in Figure 63. As expected, the results are slightly different compared to the results for the previously evaluated total (beam and isotropic diffuse radiation), favouring the northern directions more.

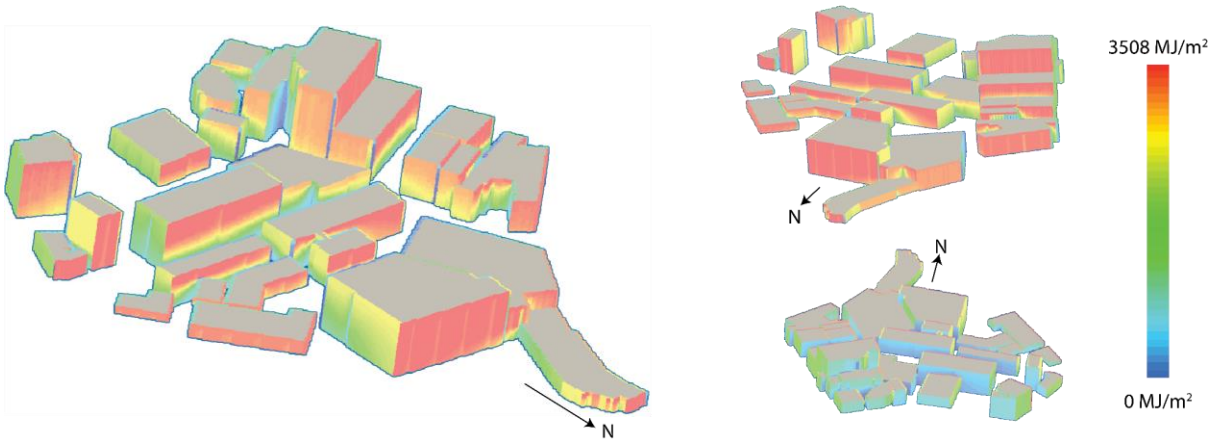

Figure 62: Annual solar energy potential (beam and anisotropic diffuse) for the AUT city campus layout

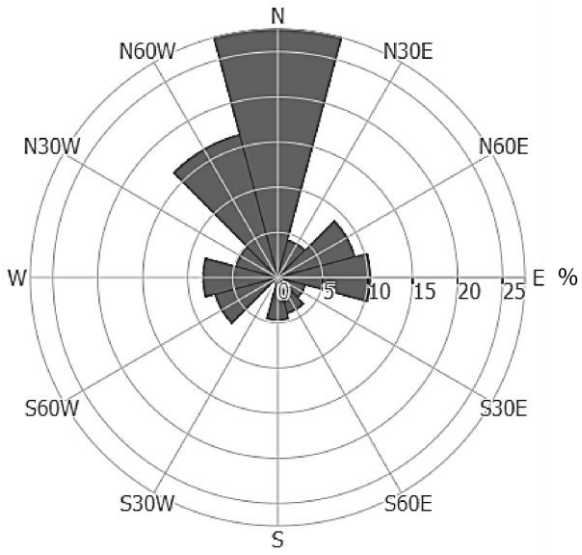

Figure 63: Percentage of yearly total (beam and anisotropic diffuse) radiation accumulated on façades in AUT city campus layout facing different directions

8.5 Applications

The results obtained so far can be applied to obtain several kinds of valuable information about the layout. For example, Figure 64 shows the annual total solar radiation potential at different storeys in

the layout. For the purpose, the annual total radiation potential was accumulated storey-wise (assuming a constant 3m storey height). The lower storeys (5 or less) appear to collect more energy due to the abundance of buildings of this height in the layout, as was shown previously in Figure 46. When this potential was averaged over the façade area of each storey, the average irradiation of each storey was obtained. As can be seen in Figure 65, locations above storey 8 were found to have greater average irradiation potential. Combining this statistic with the rose diagram (as shown in Figure 63), it is apparent that on the AUT city campus, locations on northern façades with elevations above 24m have high average total irradiation potential and they may be feasible sites for deploying solar technologies.

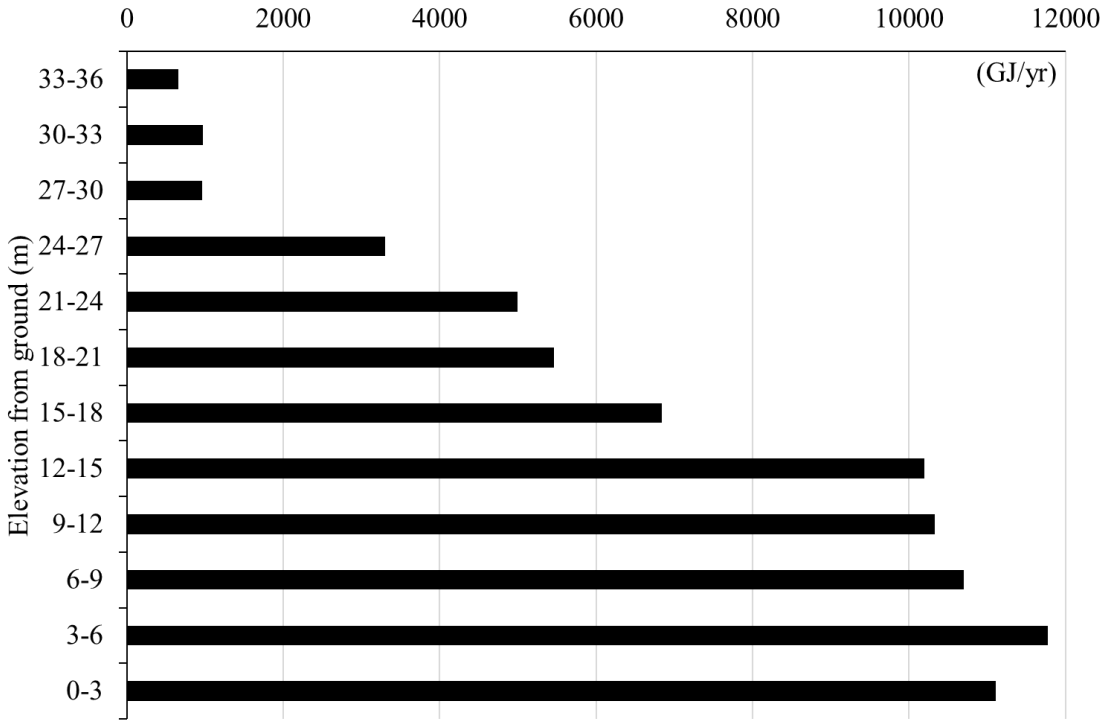

Figure 64: Total radiation potential at different storeys (elevations) of the façades in the AUT city campus layout

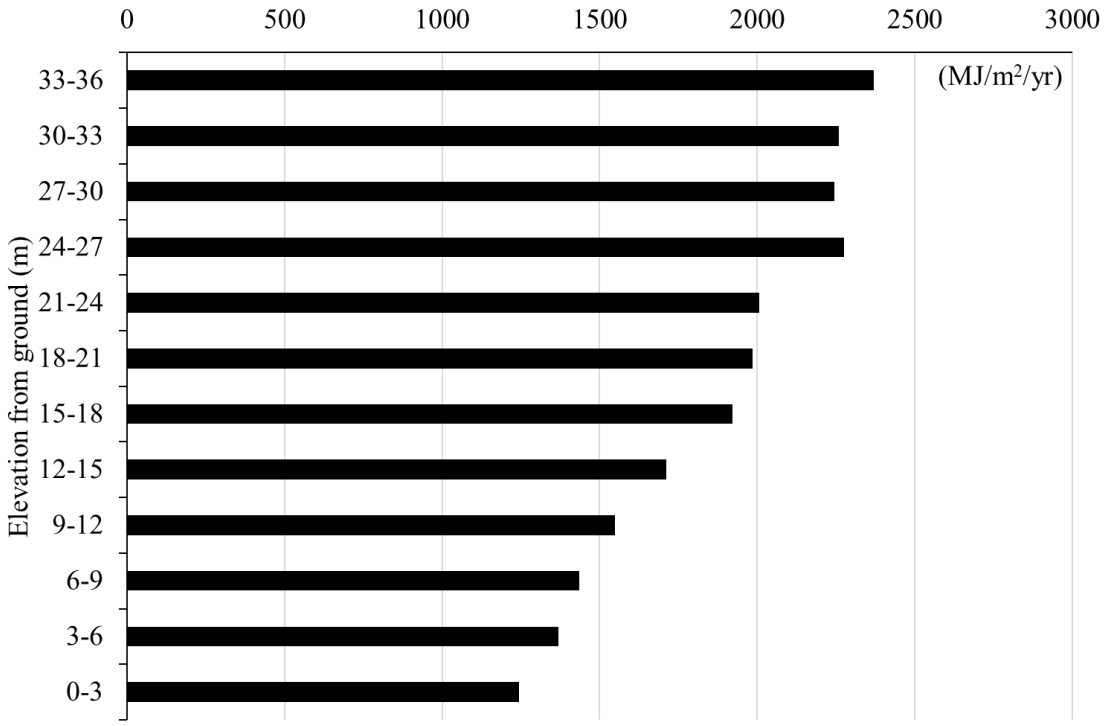

Figure 65: Average irradiation at different storeys (elevations) of the façades in the AUT city campus layout

Another interesting application is evaluating the technical potential of the site and identifying the locations on façades for installing solar technologies. Technical potential can be defined as the percentage of the region's (or building's) overall façade area that receives an amount of solar radiation greater than or equal to pre-set thresholds [170]. For the purpose, the threshold values for installing PV panels and ST collectors were taken as 2880 MJ/m^2 (800 kWh/m^2) and 1440 MJ/m^2 (400 kWh/m^2), respectively, as described by Compagnon in [171]. These values were derived on the basis of technical and economic limitations. If the irradiation at a location is higher than these thresholds, that location is considered a favourable location for installing the corresponding technology.

To work out the technical potential, a histogram of the annual irradiation against the façade area is provided in Figure 66 and the values above the thresholds for the said technologies are highlighted.

The region's technical potential for PV panels and ST collectors was found to be 21.8% and 50.4%, respectively. Based on the thresholds, the locations are identified as shown in Figure 67.

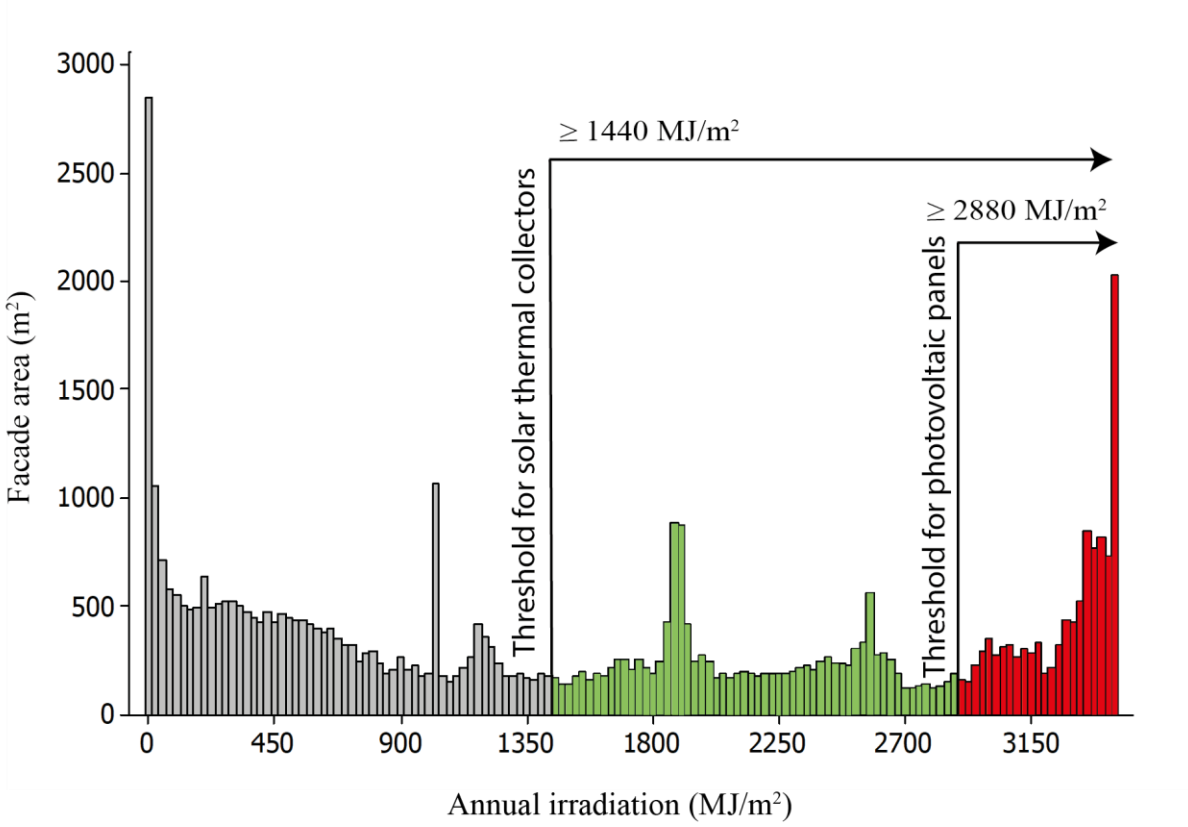

Figure 66: The annual irradiation received by the façade areas in the AUT city campus layout

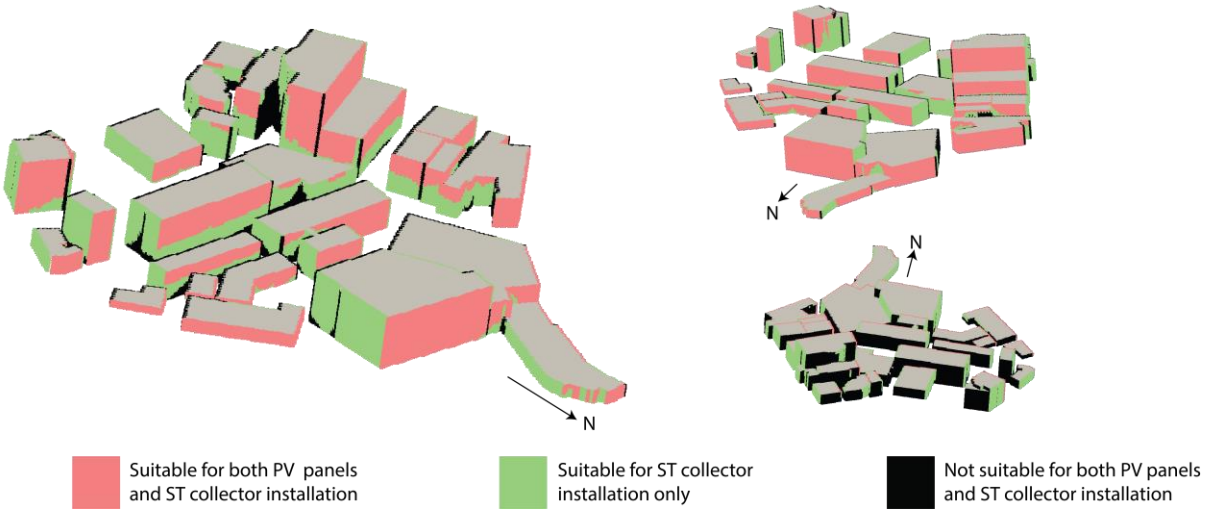

Figure 67: Locations favourable for installing PV panels and ST collectors

Lastly, the building-level results can be used to obtain the PV panel and ST collector potential for individual buildings. For example, the AUT buildings' technical potential is shown in Table 10. The WP and WB buildings have the highest PV panel potential, whereas the WH and WA buildings have the highest ST collector potential.

Table 10: Building-level technical potential for AUT buildings

Building	PV panel potential	ST collector potential
WA	30.18%	61.96%
WB	49.59%	55.15%
WC	28.69%	38.56%
WD	15.29%	36.14%
WE	17.60%	48.66%
WF	34.40%	55.46%
WG	26.06%	35.37%
WH	39.79%	87.03%
WM	1.81%	37.53%
WN	1.18%	43.06%
WO	14.11%	40.91%
WP	52.38%	52.38%
WS	20.25%	48.56%
WU	16.87%	51.64%

8.6 Summary

The proposed model was successfully implemented to evaluate the AUT city campus as a real case study. When compared with the conventional model, the proposed model was found to be performing 6.8 and 5 times faster when evaluating the beam potential and diffuse potential respectively. Substantial improvement in reducing the computation time by using horizontal scaling through multi-process and vertical scaling using a cloud environment was also demonstrated, boosting the processing speed up to 20 times and 37 times, respectively. The different solar potentials at various temporal and spatial scales were evaluated and discussed in detail.

Lastly, some valuable results were derived from the results, such as determining the storey levels in the campus layout that have maximum annual potential or average total irradiation. The technical potential in terms of installing the PV panels and ST collectors was also derived for the whole region as well as at building-level. Based on this, the locations for installing these technologies were also identified.

9

CONCLUSIONS AND RECOMMENDATIONS FOR FUTURE WORK

9.1 Conclusions

In urban areas such as modern city centres, which are comprised of tall skyscrapers and slender buildings, the limited rooftop space is creating a major barrier to the deployment of solar energy technologies on a large scale. Façades have been identified as an alternative location for solar installations but require potential assessment in the early stages of a project.

The literature review revealed that the existing area-based geographic potential assessment models use the BRT technique, which is not suitable for assessing façade potential. This is because the

application of these models on facades requires decomposition of the façade height into a large number of hyperpoints, and analysing them individually, which consumes a tremendous amount of computation time. Therefore, computing the façade solar potential of densely built environments in a reasonable time has become a major challenge.

In response to this research gap, a discretization-independent façade solar potential assessment model based on the FRT technique was developed. It consists of four sub-models for determining the shadows on the façade, and the beam, isotropic diffuse and anisotropic diffuse solar potentials. For the anisotropic diffuse potential assessment, the model uses skymaps, which drastically reduces the number of scans and hence optimizes the processing in terms of computation time. Computational process management for deploying horizontal and vertical scaling, compatible with the developed model, was also developed.

To assess the accuracy of the model, an analytical model for a hypothetical layout was derived and used as a benchmark. It was found that the accuracy of the existing model was proportional to the number of surfaces the façade was disintegrated into. In contrast, the proposed model produced the same result as the benchmark model, without the need for disintegration.

To compare speeds, both the models were executed on the same local machine and the developed model was found to be ~ 4 to 4.5 times faster in analyzing the instantaneous and annual beam and isotropic diffuse solar radiation potentials. For the anisotropic solar potential assessment, skymaps were used, which therefore corresponded to the same computation time as the isotropic diffuse solar radiation potential. It was also confirmed that the developed model was performing faster than the existing model when producing results at various levels of detail; e.g. point, facade, building and region. The management of computation processes increased the processing speed by 11% and 9% compared to the simulations at local machine, for the horizontal (multi-process) and vertical (cloud-based) scaling, respectively.

Finally, the existing and developed models were compared by using both to evaluate the solar potential of the AUT city campus, which has an area of 80,000 m^2. The proposed model was found to be computing ~6 times faster than the existing model when analysing annual beam and diffuse radiation potential. Adding horizontal and vertical scaling improved the performance by 20 and 37 times, respectively.

A couple of applications were also illustrated using results obtained from the model, which helped to provide meaningful information about the potential layout of solar facade collectors, generated by these models. For example, on the AUT city campus, the annual potential of facades up to 5 storeys high and the average irradiation potential of storeys above 7 were relatively high compared to others. Also, the PV panel and ST collector technical potentials of the campus were found to be 21.8% and 50.4%, respectively. The WP and WB buildings had the highest PV panel potential, while the WH and WA buildings showed the highest ST collector potential.

Thus, to conclude, a hyperpoints-independent solar potential assessment model for evaluating beam and isotropic and anisotropic diffuse solar potential in densely built-up environments was successfully developed in this work. The presented case studies have shown its remarkable performance in terms of speed when compared with the conventional model. The model's ability to use skymaps and its speed optimization through computational process management were also demonstrated.

9.2 Recommendations for Future Work

There are many ways in which the model and its applications can be explored in future, including but not limited to the following:

1. In this study, the façades were considered as perfectly vertical, flat surfaces, with no information included about fabric/material and essential features such as windows, doors, balconies, and awnings. This happened because the proposed model uses 2.5D DEM, which omits all details in

the third dimension (vertical) other than height. The model should be tested with 3D DEMs that can be obtained from 3D point cloud data obtained from LiDAR or IfSAR or by using sophisticated parametric/procedural modelling approaches, such as the one explained in [172]. Decomposition of the results into cells, as explained in Section 6.3.2, and mapping them on the façade features, would be a way to progress.

2. The ground, rooftops and façades of the buildings may reflect the incoming solar radiation. This eventually affects the accumulation of solar radiation on the façades of the layout in a complicated manner. One way to incorporate these effects is to apply a radiosity algorithm that uses the general radiation exchange at the point-level details of results obtained from the proposed model. A simplified radiosity algorithm is explained in [173].
3. Vegetation in the layout, such as trees and bushes, may significantly reduce the façade solar potential [174]. Their effects would be most prominent in the first couple of storeys. Analysing their effects is complicated as the shape of vegetation (spread, height, leaf sizes etc.) changes with the seasons. One potential improvement in the shadow scanning algorithm could be to account for the vegetation present in the layout.
4. Further applications of the results could be explored; for example, finding potential and feasible locations for incorporating passive heating technologies during the heating season [175, 176], deploying façade-mounted solar concentrating systems [177], the application of laminated amorphous PV that can be cut to almost any size and shape [178] and incorporating transparent and translucent solar technologies for windows [179].
5. The model may be further optimized for speed in a couple of other ways, such as making use of hybrid ray tracing techniques that combine the advantages of both BRT and FRT techniques [180], and using pyramid datasets [62] and other low-resolution sky discretization techniques as long as they yield acceptable levels of accuracy [128].
6. Extending the proposed model to yield the roof-top solar potential as well.
7. Integrating the model into state-of-the-art GIS software, such as Esri products (e.g. ArcGIS) [181], QGIS [182] and GRASS GIS [183]) would be very interesting from both the utilization and

commercialization points of view. This would help GIS and solar analysts worldwide to integrate the model's results with other geographic analyses.

Appendix A: The Benchmark Model

In the context of this study, a benchmark model is defined as a solar potential assessment model that considers a façade as whole; i.e. it doesn't decompose the façade into hyperpoints (like the BRT model) or stripes (like the FRT model), and hence it should the most accurate. Since this model is based on simple geometrical relations, its application is limited to less complex surroundings only. This model has been used in comparing the performance of BRT and FRT models in Chapter 2, 3 and 4. It is comprised of a scanning algorithm, presented in Section I and a solar potential assessment model, given in Section II, in the following. The validation and accuracy of this model has been assessed in Section III.

I. Scanning Algorithm

In this section, a method for determining the lit heights on the façade using simple geometrical relationships is described, considering a simple layout, as shown in Figure 68.

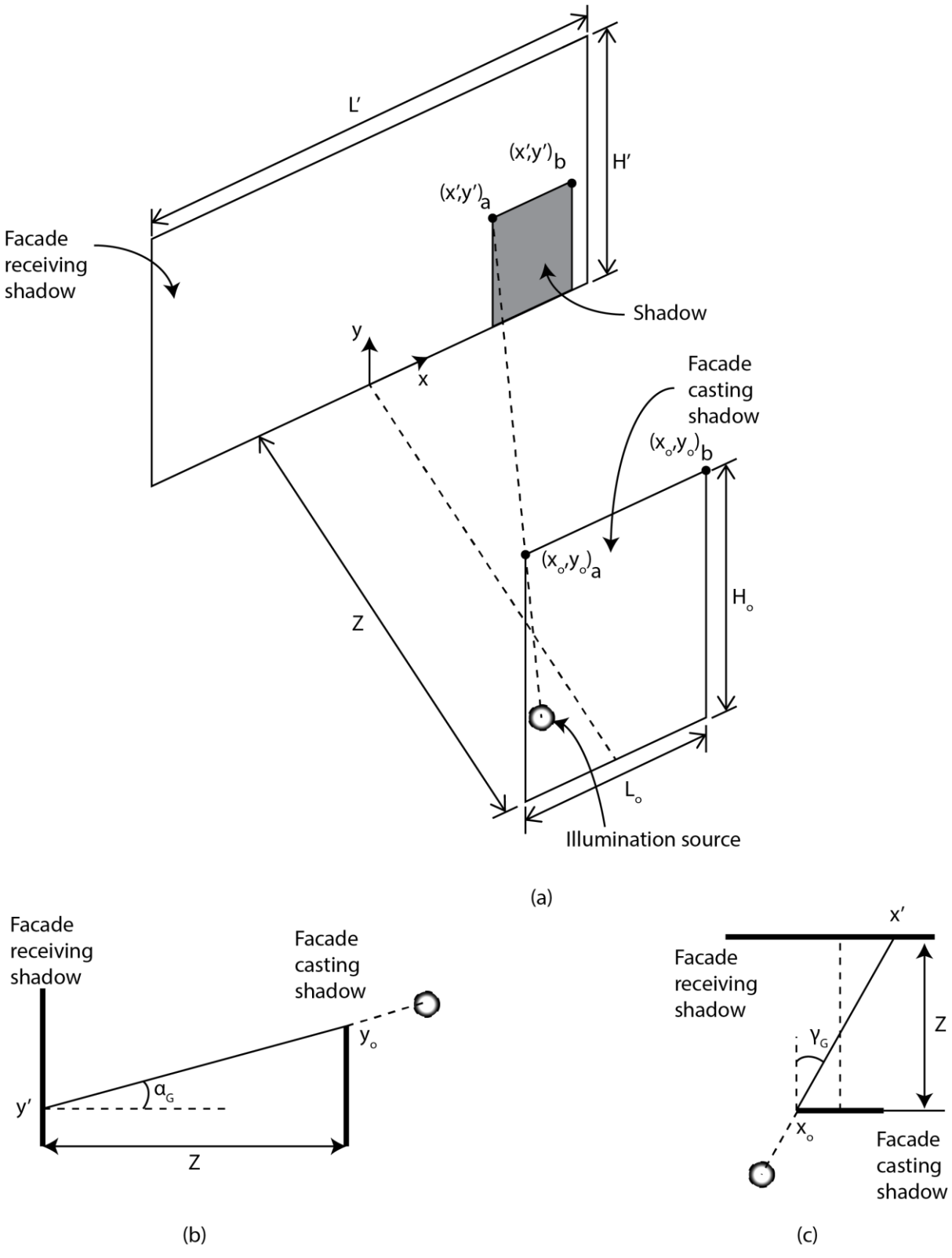

Figure 68: Simple geometrical layout used while developing the benchmark model (a) Shadow formation (b) Side view (c) Bird-eve view

The façade receiving the shadow has length L' along the x-axis and height H' along the y-axis. The façade that is casting the shadow has a length of L_o and height H_o along the x- and y-axes, respectively. These two façades are a distance Z apart. The illumination source is assumed to be behind the façade casting a shadow and has an azimuth and altitude angle of γ_G and α_G, respectively. The angle α_G is measured positive upward from the horizontal whereas γ_G is measured positive when the illumination source is towards the left of façade and is otherwise negative. The façade casting the shadow has its elevated corners represented by the coordinates $(x_o, y_o)_a$ and $(x_o, y_o)_b$. The corresponding corners of the shadow are represented by the coordinates $(x', y')_a$ and $(x', y')_b$, respectively. These coordinates can be obtained using Eq. (46) and Eq. (47):

$$x'_{a,b} = x_{o\,a,b} + Z\ \tan\gamma_G \tag{46}$$

and

$$y'_{a,b} = y_{o\,a,b} - Z\ \tan\alpha_G \tag{47}$$

As the shadow is received by a façade having finite dimensions, the corner points of the shadow should not extend beyond the given physical length and height of the facade. Hence, the constraints given by Eq. (48) and Eq. (49) should be applied:

$$x'_{a,b} = \begin{cases} 0, & x' < 0 \\ L', & x' > L' \end{cases} \tag{48}$$

and

$$y'_{a,b} = \begin{cases} 0, & y' < 0 \\ H', & y' > H' \end{cases} \tag{49}$$

Finally, the lit area (A_l, m^2) of the façade receiving shadow can be obtained by taking away the area of the shadow (A_s, m^2) from the total area (A, m^2) of the façade. The area of the shadow can be evaluated by using the coordinates of the corners of shadows, given by Eq. (50) and (51):

$$A_l = A - A_s \quad \textbf{(50)}$$

where

$$A_s = y'_a(x'_b - x'_a) \quad \textbf{(51)}$$

II. Solar Potential Assessment Model

This section describes the method of determining the beam and diffuse solar potential of the façade that is receiving the shadow. It can be used for evaluating the accuracy of any other analytical, empirical or numerical model developed for the same purpose.

From the fundamental understanding of radiative heat transfer, the solar radiant flux (I, Watt), received by an exposed surface area (A, m^2), perpendicular to the incoming irradiance (I'', W/m^2), could be given by Eq. (52), and also illustrated in Figure 69:

$$I = I'' A \quad \textbf{(52)}$$

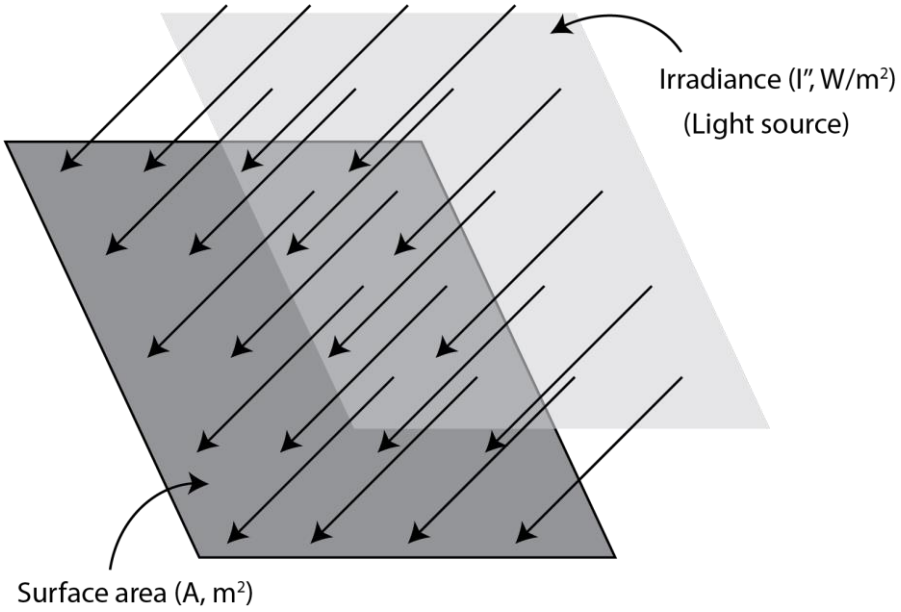

Figure 69: Illustration of radiant flux received by a surface

If the incident irradiance is in the form of beam irradiance (I_b'', W/m^2), approaching in a direction such that it is making an angle of θ with the normal of the receiving surface, the beam radiant flux (I_b, Watts) can be written as Eq. (53):

$$I_b = I_b'' \cos\theta \ A \qquad \textbf{(53)}$$

Eq. (53) can be modified for a special case when the receiving surface is a façade. In such a situation, θ will be the angle between the incoming beam irradiance and the normal to the receiving façade (also known as incidence angle).

Then, in a more practical situation, when the façade is partially in shadow (e.g. due to the sun being blocked by obstacles in the surrounding environment), Eq. (53) can be modified to produce the lit surface area of the façade instead of the total surface area, as given by Eq. (54):

$$I_b = I_b'' \cos\theta \, . A_l \qquad \textbf{(54)}$$

Deriving the isotropic diffuse solar potential of façade requires an understanding of the sky discretization technique [130]. In this technique, the large hemispherical sky vault around the receiving surface is divided into a number of illuminating areas, termed “sky elements”. Each of these areas is assumed to have a single illumination source at its centre, pointing towards the chosen point on the surface.

From the fundamental theory of radiative heat transfer [184, 185, 186], the area of the elements can be obtained from the solid angles (ω, sr) associated with it. So, for any arbitrarily chosen q^{th} sky element, as shown in Figure 70, the solid angle is given by Eq. (55):

$$\omega_q = \Delta\gamma\Delta\alpha \cos\alpha_q \qquad \textbf{(55)}$$

where $\Delta\gamma$ and $\Delta\alpha$ are the azimuthal width and height of a sky element located at the base of the vault and α_q is the altitude angle of the chosen sky element. The area of the sky element is proportional to the term $\cos\alpha_q$.

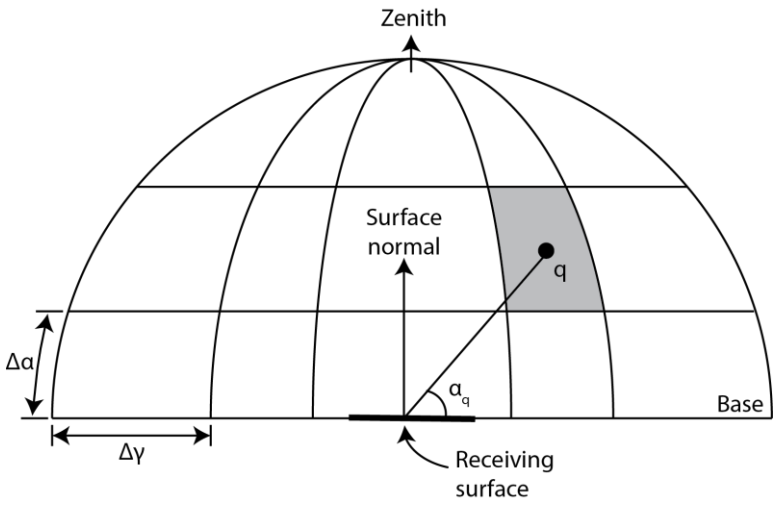

Figure 70: Illustration of the discretized sky vault with a chosen sky element

The apparent area of the sky element when it is seen from the receiving surface depends upon the viewing angle. So, to account for this, the solid angle, ω_q, should be multiplied by $\sin\alpha_q$.

The total apparent area of the vault as seen from the point on the receiving surface is the sum of all the individual areas. Hence, if the vault has been discretised to Q sky elements, that area will be as shown in Eq. (56):

$$\sum_{Q} \omega \sin \alpha = \omega_1 \sin \alpha_1 + \omega_2 \sin \alpha_2 + \cdots + \omega_Q \sin \alpha_Q \quad \textbf{(56)}$$

With the help of Eq. (56), the radiance approaching from any sky element (R, W/m^2.sr) can be obtained by distributing the incoming isotropic diffuse solar irradiance (I_d'', W/m^2) over all the sky elements, as shown in Eq. (57) [130]:

$$R = \frac{I_d''}{\sum \omega \sin \alpha} \quad \textbf{(57)}$$

This leads to evaluating the fraction ($I_{d\,q}''$, W/m^2) of incoming diffuse solar irradiance arriving from the q^{th} sky element, as given by Eq. (58):

$$I_{d\,q}'' = R\left(\omega_q \sin \alpha_q\right) \quad \textbf{(58)}$$

where each of these fractions can be treated as similar to the beam irradiance. For example, the fraction of the diffuse solar potential (I'_{d_q}, Watt) received from the q^{th} sky element by a surface of area A (m^2) can be written similar to Eq. (52), such that given by Eq. (59):

$$I'_{d_q} = I_{d\,q}'' A \quad \textbf{(59)}$$

Also, summing up all the fractions would yield the diffuse potential in an unobstructed sky condition.

Taking this further towards obtaining the potential of a surface situated in a partially obstructed sky, the surface area in shadow for each of the individual radiances should be considered separately. For

example, consider the cases shown in Figure 71. The three radiances (1,2 and 3) are approaching the surface but there is an obstruction that may block their path (Figure 71(a)). This obstruction is casting a shadow for each of the radiances which is different in its appearance (Figure 71(b)). Thus, the radiant flux received by the surface from these fractions would be: $I'_{d_1} + I'_{d_2} + I'_{d_2} = I''_{d\,1}\,A_{l,1} + I''_{d\,2}\,A_{l,2} + I''_{d\,3}\,A_{l,3}$. Where $A_{l,1}$, $A_{lit,2}$ and $A_{l,3}$ represent the lit area of the surface for radiances 1, 2 and 3, respectively.

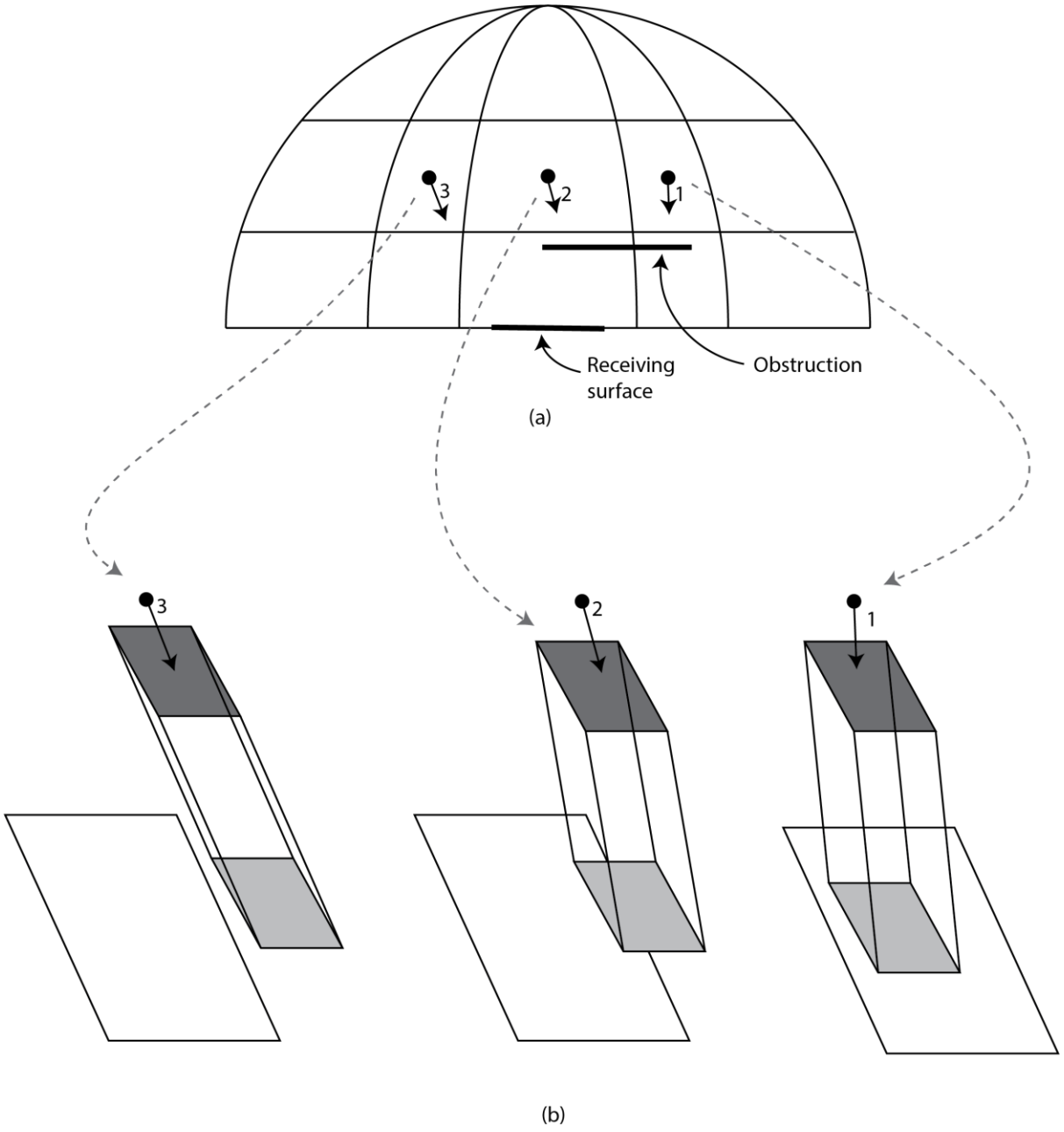

Figure 71: (a) Radiances reaching the surface having an obstruction in their path; (b) illustration of shadows being cast

Hence, the isotropic diffuse radiant flux can be written as shown in Eq. (60):

$$I_d = \sum_Q I'_{d_q} = \sum_Q I''_{d\,q}\, A_{l,q} \qquad \textbf{(60)}$$

Care should be taken for tilted and vertical surfaces when such surfaces can receive radiance only when it is approaching from the front. For this purpose, the $\sin \alpha_q$ in Eq. (58) should be replaced by the incidence effects, given by δ_q, which can mathematically be represented by Eq. (61):

$$\delta_q = \cos \theta_q \vee 0 \qquad \textbf{(61)}$$

where θ_q is the incidence angle between the radiance from the element and the normal to the receiving surface. Also, "$\vee$" is the maximum operator, which would take the maximum of its two arguments and hence ignore any radiance approaching from the back side of the surface.

The Diffuse Sky Factor (DSF), which can be defined as the ratio between the irradiance received by the surface and the irradiance at the horizontal, can be given by Eq. (62):

$$DSF = \frac{I_d}{AI''_d} \qquad \textbf{(62)}$$

The DSF has a similar use to the sky view factor (SVF), where, once determined, it can be used to obtain the radiation at a tilted surface when the global irradiance is provided. However, the SVF deals only with a point at a surface whereas the DSF deals with the whole surface.

Finally, the total solar potential of the surface can be obtained by summing up both the beam and diffuse solar potentials, as given by Eq. (63):

$$I = I_b + I_d \quad \textbf{(63)}$$

where I_b'' and I_d'', which are required for evaluating I_b and I_d, can be obtained from several resources, such as world maps of solar radiation [45], databases [40] and geo-coordinate dependent mathematical models [38].

III. Validation

Since the benchmark model cannot process complicated layouts, a simple hypothetical layout was chosen for the validation purpose, as shown in Figure 72.

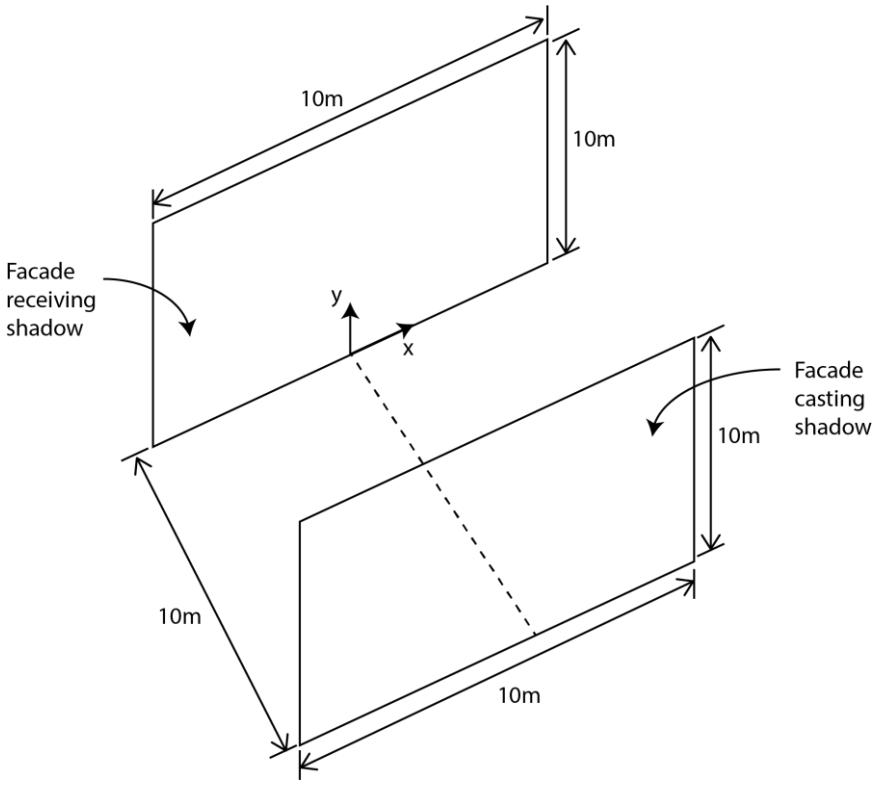

Figure 72: Hypothetical layout chosen for validating the benchmark model

The simulation was performed for a scenario where the sun is at $\alpha_G = -35°$ and $\gamma_G = 20°$ and the shadow corners on the receiving façade were obtained, giving the lit areas as shown in Figure 75. The

benchmark model yielded a lit area of 55.5 m^2. To validate this result, a 3D geometric model representing the same hypothetical layout was created in Google Sketchup. The coordinates of the shadow points and the lit area was measured manually using the tools provided in the program. The results were compared and were found to be in excellent agreement with each other.

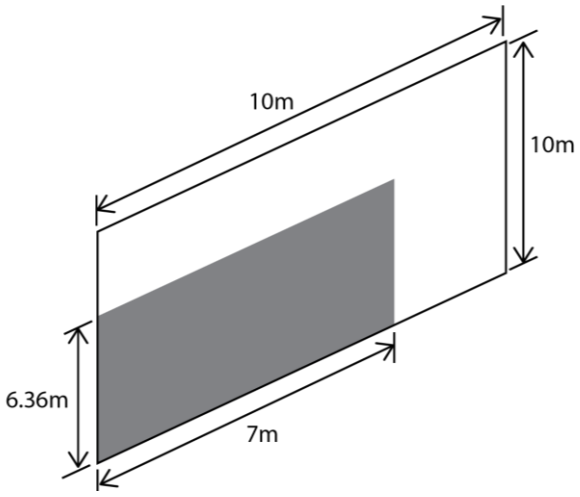

Figure 73: Graphical illustration of the simulation results from benchmark model

To estimate the beam potential, the incidence angle was also measured manually in the Google Sketchup program and was found to be $\theta = 38.3°$. When assuming a beam normal irradiance of I_b'' =500 W/m^2, the benchmark model yielded an instantaneous beam radiation potential of 21 777 W ($= \frac{500W}{m^2} \times 55.5\ m^2 \times \cos 38.3°$).

For the diffuse potential, the sky was discretised into elements taking $\Delta\gamma = \Delta\alpha = 1°$. The diffuse potential on the façade was assessed using $I_d'' = 500\ W/m^2$. The two scenarios were simulated. In the first scenario, the building casting the shadow was neglected, creating an unobstructed sky. In this scenario, the potential of the facade was evaluated to be 25 000 W, which is half of what it could have collected if placed horizontally ($= \frac{1}{2} \times 500 \frac{W}{m^2} \times 10m \times 10m$). This corresponds with the understanding of SVFs [58] of vertical collecting surfaces; such façades, under no sky obstruction,

receive 50% of the diffuse solar radiation that could be collected by a surface of the same area lying horizontally.

In the second scenario, the shadow cast by the building was accounted for and the solar potential was found to be 23 640 W. This is approximately 47% of the diffuse solar radiation that could have been collected by a surface of the same area lying horizontally.

Appendix B: Coefficients for the Sky Radiance Model

The following table has been copied from Brunger and Hooper [79]. The values are required while simulating the BRT anisotropic diffuse model, presented in Chapter 5 and in developing the skymap as described in Appendix C.

k \ k_t	0.05	0.15	0.25	0.35	0.45	0.55	0.65	0.75	0.85
0.95	0.1864	0.2002	0.138	0.1508	0.1718	0.2060			
	0.1979	0.1772	0.093	0.5472	0.0566	−0.0294			
	0.0000	0.0000	0.289	0.6659	0.8734	2.9511			
	1.0000	1.0000	0.9667	1.6755	2.4129	3.7221			
0.85	0.1431		0.3477	0.2664	0.2139	0.1520	0.1151		
	0.142		−0.2153	−0.1559	0.0307	0.1497	0.1805		
	2.636		5.3170	1.7758	1.6099	1.8315	2.2284		
	5.525		4.4211	2.8590	3.726	4.6125	4.1553		
0.75			0.3687	0.2684	0.2019	0.1870	0.1842	0.1566	
			−0.2927	−0.1615	−0.1275	−0.0632	0.0253	0.3003	
			2.6268	4.5224	1.4096	1.2819	1.3080	1.8486	
			2.8413	4.0842	2.2453	2.5932	3.1127	14.744	
0.65			0.3851	0.2843	0.2713	0.1597	0.2088	0.1273	
			−0.2726	−0.1645	−0.1837	−0.1715	−0.0520	−0.0500	
			4.1962	5.2960	2.822	1.2964	1.3225	1.5961	
			5.259	4.3678	3.486	1.9183	2.8364	2.0993	
0.55			0.6079	0.2892	0.2816	0.2465	0.2070	0.2477	
			−0.4838	−0.1953	−0.1945	−0.1245	−0.0927	−0.0711	
			11.078	2.1346	3.8606	2.9163	1.1098	1.5836	
			4.588	3.7268	3.7447	4.0760	2.5586	3.450	
0.45				0.2337	0.2822	0.2916	0.2583	0.2457	0.2315
				−0.1015	−0.1842	−0.2065	−0.1654	−0.1398	−0.2028
				11.792	6.0300	2.7327	1.9525	1.512	1.5803
				5.3698	4.5241	3.7624	3.3769	2.964	2.3229
0.35		a_0			0.3162	0.3006	0.2871	0.2491	0.2510
		a_1			−0.2039	−0.2172	−0.2184	−0.2224	−0.0907
		a_2			6.2226	4.5443	2.6467	1.5992	0.9733
		a_3			5.8975	4.2660	3.594	2.6404	2.6775
0.25						0.3417	0.3153	0.3071	0.2971
						−0.2574	−0.2338	−0.2576	−0.3126
						4.1918	3.8860	2.3127	1.3594
						4.3268	4.3920	3.5189	2.397
0.15							0.3360	0.3243	0.3061
							−0.2600	−0.3003	−0.4531
							4.2481	1.9157	1.612
							4.3727	3.2680	2.319

The values of a_o, a_1, a_2 and a_3 are specified in the form of ranges for solar diffuse fraction ($k(\tau)$) and the atmospheric clearness index ($k_t(\tau)$). The value of k represents the fraction of the diffuse component in the global irradiance. Therefore, in an overcast sky condition, when most of the incoming radiation is diffuse in nature, the value of k is high (close to 1). In contrast, in clear sky

conditions, when the beam component is more dominant than the diffuse component, the value of k is low (close to 0). Under clear skies, the circumsolar diffuse is weighted more heavily than the isotropic subcomponent. The value of k_t describes the fraction of global irradiance in the extra-terrestrial irradiance. The main reason for the attenuation of global irradiance is scattering and absorption in the atmosphere. Hence, an overcast sky corresponds to a low value of k_t (close to 0) compared with clear sky, which has a high value of k_t (close to 1). A partly cloudy sky condition has an average value of both k and k_t (close to 0.5).

Appendix C: Anisotropic Skymap for Auckland

In isotropic sky conditions, the Diffuse Sky Factor (DSF_{iso}) is independent of time (or hour of the year). Hence, a single scan from each sky element is sufficient to perform the assessment (Eq. (32) in Chapter 4). However, the situation is complicated when the sky is assumed anisotropic for obtaining mosre realistic results. In such a condition, the Diffuse Sky Factor (DSF_{aniso}) has a temporal dimension as well (Eq. (40) in Chapter 5). This means that a scan is required for each sky element for every instant of time. Assuming that the sky discretization resolution is 1º, there will be 32k sky elements, and if the assessment period is, say, 4000 hours, then the number of scans required will be 126.6 million, which will require a huge amount of scanning time.

To mitigate this situation, an anisotropic skymap can be developed, similar to the concept shown in [142, 187]. Such a skymap will have the accumulated radiance values for each sky element (kJ/m^2.sr), over the given time period. This is represented by the term "$[\sum_\tau f_{BH}]$" associated with individual sky elements (γ_e, θ_e) in Eq. (41) in Chapter 5.

To generate the anisotropic skymap for Auckland, the Brunger and Hooper model [79] and the constants (Appendix B) were used to obtain the radiance values for each sky element at (γ_e, θ_e). The desired radiation parameters associated with the sky conditions and the sun position for Auckland were obtained from a geolocation-tied database [48].

A skymap can be generated for any assessment duration required. For example, the results of an anisotropic skymap for Auckland, generated for annual assessments, are illustrated in Figure 74 as a 360º-panorama. The range of accumulation for the sky elements is between 498 MJ/m^2.sr and 1135 MJ/m^2.sr. The bright region represents the sun's path throughout the year, which contributes a circumsolar subcomponent. The darker regions may still represent a relatively small amount of radiation due to the isotropic (and/or horizon brightening) subcomponents. The skymap is required

while simulating the BRT anisotropic diffuse model, presented in Chapter 5, and is used during simulations for the real case-study, shown in Chapter 8.

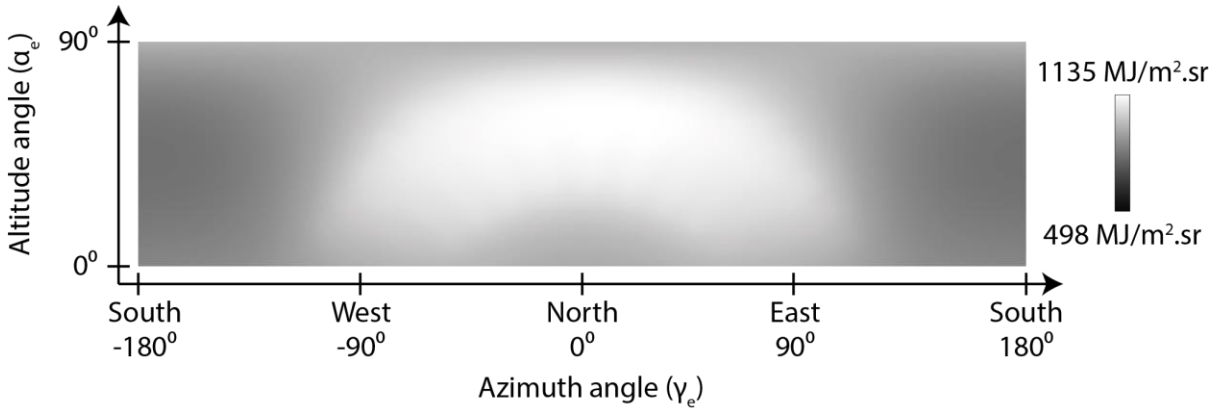

Figure 74: 360°-panorama of annual anisotropic skymap for Auckland

The high-resolution images of the hourly and the final skymaps for Auckland are available in ‘codes/AnisoSkymaps/’.

Appendix D: Auckland Elevation Data

The proposed solar potential assessment model requires elevation data to create the digital elevation models (DEMs) and their variations for the site to be analyzed. For New Zealand, as was required in Chapter 8, this data can be obtained from the Land Information New Zealand (LINZ) Data Service, which is an online interactive portal [188]. LINZ is responsible for managing land titles, geodetic and cadastral survey systems, topographic information, hydrographic information, and supporting government decision making around foreign ownership in New Zealand.

For Auckland, the elevation data is available for both terrains (DTM) [189] and urban surfaces (DSM) [190], as illustrated in Figure 75. The reference vertical datum used is NZVD2009 [191]. Both the datasets have the same resolution of 1m with vertical and horizontal accuracy of +/-0.2m and +/0.6m (at 95% confidence intervals), respectively. For querying these datasets, LINZ has provided a web-based Raster Query Application Programming Interface (API) [192]. The API call requires the user's API private key (which can be registered after creating an account at the LINZ portal), the layer number (which is 53405 and 53406 for DTM and urban DSM, respectively), and the latitude and longitude of the point. The service returns the results (elevation measured from datum in metres) in JavaScript Object Notation (JSON) [193] data format, which can be interpreted by most data processing packages and programming languages.

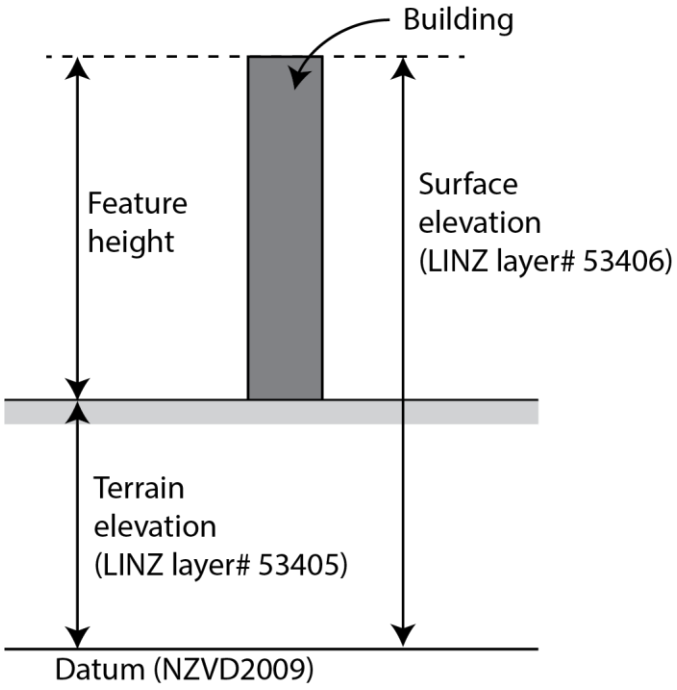

Figure 75: Terrain and urban surface elevation data obtained from the Land and Information New Zealand (LINZ) data service

The use of the LINZ data service is explained here in terms of finding the height of the ANZ Centre (36.84569 ºS, 174.7644 ºE), which is one of the tallest buildings in the heart of Auckland's City Centre, as shown in Figure 76.

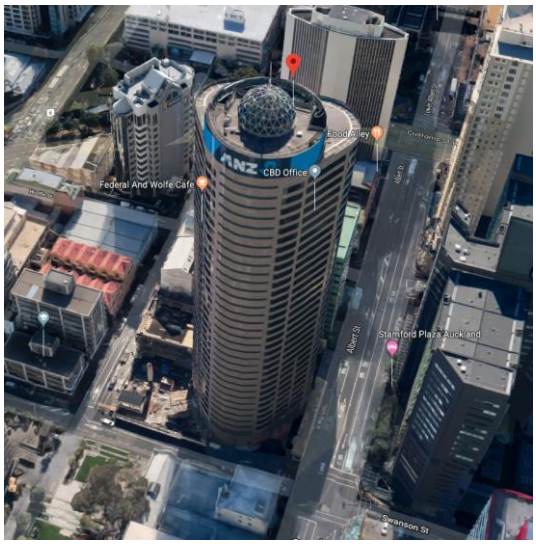

Figure 76: ANZ Centre in Auckland (36.84569 ºS, 174.7644 ºE) [194]

The height can be obtained by subtracting the terrain elevation from the urban surface elevation. So, for the terrain elevation, the API call is:

https://data.linz.govt.nz/services/query/v1/raster.json?key=KEY&layer=53406&x=174.7644&y=-36.84569

which returns a result of 17.1361m, as can be seen in Figure 77.

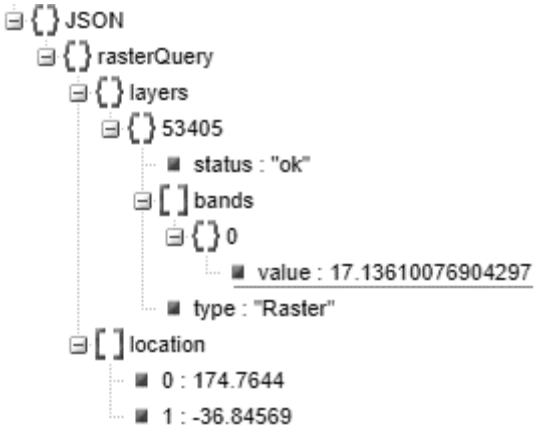

Figure 77: The JSON response showing terrain elevation of the ANZ tower

And for the surface elevation, the API call is:

https://data.linz.govt.nz/services/query/v1/raster.json?key=KEY&layer=53405&x=174.7644&y=-36.84569

which returns a result of 153.7478m, as can be seen in Figure 78.

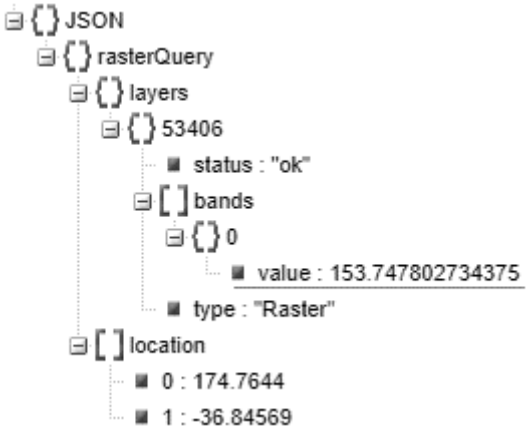

Figure 78: The JSON response showing surface elevation of ANZ tower

Hence, the height of the ANZ centre is 136.6m. This is very close to the reported height of the tower, which is 143m [195].

After accessing the elevation data, the next most important information required the details about the buildings' façades and their angles. The OpenStreetMap [196], which is again an interactive portal, can be used for extracting this information. It involves three steps:

1. Open OpenStreetMap.org and zoom in to the region of interest.
2. Manually select the area for which the information is required.
3. Export the information.

The information can be downloaded in Extensible Markup Language (XML) [197], which requires further processing yielding:

1. Name and ID of building
2. Latitude and longitude of each corner of building (treated as a polygon)

From this, the LINZ APIs can be called to obtain the elevation information, which can be converted into raster DSM. By manipulating the slope of each line segment of the building's polygon, the normal to that line (hence the façade), can be obtained [198].

Finding information from OpenStreetMap and LINZ is handy, but the results come with some precautions and assumptions:

1. The 2.5D DEM produced after the procedure described above does not provide any details about the façade fabric, or the position and sizes of windows, doors, awnings etc.
2. The updates of both the databases may differ, and they may be different from the current situation (e.g. due to recent construction). Hence, it is recommended to do a manual check before use.

REFERENCES

[1] International Energy Agency, "World Energy Outlook," 2012. [Online]. Available: http://www.worldenergyoutlook.org/weo2012/. [Accessed 1 Mar 2019].

[2] U.S. Energy Information Administration, "International Energy Outlook," 2016. [Online]. Available: https://www.eia.gov/outlooks/ieo/pdf/0484(2016).pdf. [Accessed 1 Mar 2019].

[3] R. Prăvălie, C. Patriche and G. Bandoc, "Spatial assessment of solar energy potential at global scale. A geographical approach," *Journal of Cleaner Production*, vol. 209, pp. 692-721, 2019.

[4] E. Kabir, P. Kumar, S. Kumar, A. Adelodun and K. Kim, "Solar energy: Potential and future prospects," *Renewable and Sustainable Energy Reviews*, vol. 82, pp. 894-900, 2018.

[5] D. Sun and L. Wang, "Research on heat transfer performance of passive solar collector-storage wall system with phase change materials," *Energy and Buildings*, vol. 119, pp. 183-188, 2016.

[6] H. Chan, S. Riffat and J. Zhu, "Review of passive solar heating and cooling technologies," *Renewable and Sustainable Energy Reviews*, vol. 14, no. 2, pp. 781-789, 2010.

[7] M. Nair, K. Ramamurthy and A. Ganesan, "Classification of indoor daylight enhancement systems," *Lighting Research & Technology*, vol. 46, no. 3, pp. 245-267, 2014.

[8] P. Mohanty, T. Muneer, E. Gago and Y. Kotak, "Solar Radiation Fundamentals and PV System Components," in *Solar Photovoltaic System Applications*, SP Mohanty, T. Muneer and M.

Kolhe ed., Cham, Switzerland, Springer, 2016, pp. 7-47.

[9] International Energy Agency, "Power - Market analysis and forecast from 2018 to 2023," 2018. [Online]. Available: https://www.iea.org/renewables2018/power/. [Accessed 1 Mar 2019].

[10] S. Seddegh, X. Wang, A. Henderson and Z. Xing, "Solar domestic hot water systems using latent heat energy storage medium: a review," *Renewable and Sustainable Energy Reviews,* vol. 49, pp. 517-533, 2015.

[11] M. Ali, H. Fath and P. Armstrong, "A comprehensive techno-economical review of indirect solar desalination," *Renewable and Sustainable Energy Reviews,* vol. 15, no. 8, pp. 4187-4199, 2011.

[12] V. Reddy, S. Kaushik, K. Ranjan and S. Tyagi, "State-of-the-art of solar thermal power plants—A review," *Renewable and Sustainable Energy Reviews,* vol. 27, pp. 258-273, 2013.

[13] International Energy Agency, "Solar Heat Worldwide," [Online]. Available: https://www.iea-shc.org/solar-heat-worldwide. [Accessed 1 Mar 2019].

[14] M. Hoogwijk, "On the global and regional potential of renewable energy sources," Utrecht University, Utrecht, The Netherlands, 2004.

[15] J. A. Duffie and W. A. Beckman, Solar engineering of thermal processes, 3rd ed., Wiley New York, 2013.

[16] E. Marques Filho, A. Oliveira, W. Vita, F. Mesquita, G. Codato, J. Escobedo, M. Cassol and J. França, "Global, diffuse and direct solar radiation at the surface in the city of Rio de Janeiro: Observational characterization and empirical modeling," *Renewable Energy,* vol. 91, pp. 64-74,

2016.

[17] D. Stanciu, C. Stanciu and I. Paraschiv, "Mathematical links between optimum solar collector tilts in isotropic sky for intercepting maximum solar irradiance," *Journal of Atmospheric and Solar-Terrestrial Physics,* vol. 137, pp. 58-65, 2016.

[18] J. Widén, "Distributed Photovoltaics in the Swedish Energy System. Model Development and Simulations," Uppsala University, Uppsala, Sweden, 2009.

[19] R. Temps and K. Coulson, "Solar radiation incident upon slopes of different orientations," *Solar energy,* vol. 19, no. 2, pp. 179-184, 1977.

[20] S. A. Kalogirou, Solar energy engineering: processes and systems, 2nd ed., Cambridge, MA: Academic Press, 2013.

[21] F. Tymvios, C. Jacovides, S. Michaelides and C. Scouteli, "A Comparative study of Ångström's and artificial neural networks' methodologies in estimating global solar radiation," *Solar Energy,* vol. 78, no. 6, pp. 752-762, 2005.

[22] X. Xu, H. Du, G. Zhou, F. Mao, P. Li, W. Fan and D. Zhu, "A method for daily global solar radiation estimation from two instantaneous values using MODIS atmospheric products," *Energy,* vol. 111, pp. 117-125, 2016.

[23] K. Zakšek, T. Podobnikar and K. Oštir, "Solar radiation modelling," *Computers & Geosciences,* vol. 31, no. 2, pp. 233-240, 2005.

[24] J. Chen, L. He, Q. Chen, M. Lv, H. Zhu, Z. Wen and S. Wu, "Study of monthly mean daily diffuse and direct beam radiation estimation with MODIS atmospheric product," *Renewable*

Energy, vol. 132, pp. 221-232, 2019.

[25] M. El-Metwally, "Sunshine and global solar radiation estimation at different sites in Egypt," *Journal of Atmospheric and Solar-Terrestrial Physics*, vol. 67, no. 14, pp. 1331-1342, 2005.

[26] H. Li, X. Bu, Z. Long, L. Zhao and W. Ma, "Calculating the diffuse solar radiation in regions without solar radiation measurements," *Energy*, vol. 44, no. 1, pp. 611-615, 2012.

[27] B. Liu and R. Jordan, "The interrelationship and characteristic distribution of direct, diffuse and total solar radiation," *Solar energy*, vol. 4, no. 3, pp. 1-19, 1960.

[28] C. Pandey and A. Katiyar, "A comparative study to estimate daily diffuse solar radiation over India," *Energy*, vol. 34, no. 11, pp. 1792-1796, 2009.

[29] A. El-Sebaii and A. Trabea, "Estimation of horizontal diffuse solar radiation in Egypt," *Energy Conversion and Management*, vol. 44, no. 15, pp. 2471-2482, 2003.

[30] S. Khahro, K. Tabbassum, S. Talpur, M. Alvi, X. Liao and L. Dong, "Evaluation of solar energy resources by establishing empirical models for diffuse solar radiation on tilted surface and analysis for optimum tilt angle for a prospective location in southern region of Sindh, Pakistan," *International Journal of Electrical Power & Energy Systems*, vol. 64, pp. 1073-1080, 2015.

[31] S. Shamshirband, K. Mohammadi, H. Khorasanizadeh, L. Yee, M. Lee, D. Petković and E. Zalnezhad, "Estimating the diffuse solar radiation using a coupled support vector machine–wavelet transform model," *Renewable and Sustainable Energy Reviews*, vol. 56, pp. 428-435, 2016.

[32] B. Jamil and N. Akhtar, "Estimation of diffuse solar radiation in humid-subtropical climatic region of India: Comparison of diffuse fraction and diffusion coefficient models," *Energy,* vol. 131, pp. 149-164, 2017.

[33] Y. Jiang, "Estimation of monthly mean daily diffuse radiation in China," *Applied Energy,* vol. 86, no. 9, pp. 1458-1464, 2009.

[34] M. Gul and T. Muneer, "Solar diffuse irradiance: estimation using air mass and precipitable water data," *Building Services Engineering Research and Technology,* vol. 19, no. 2, pp. 79-85, 1998.

[35] S. Rehman and M. Mohandes, "Artificial neural network estimation of global solar radiation using air temperature and relative humidity," *Energy Policy,* vol. 36, no. 2, pp. 571-576, 2008.

[36] K. Bakirci, "Models of solar radiation with hours of bright sunshine: a review," *Renewable and Sustainable Energy Reviews,* vol. 13, no. 9, pp. 2580-2588, 2009.

[37] H. Li, X. Bu, Y. Lian, L. Zhao and W. Ma, "Further investigation of empirically derived models with multiple predictors in estimating monthly average daily diffuse solar radiation over China," *Renewable energy,* vol. 44, pp. 469-473, 2012.

[38] V. Badescu, C. A. Gueymard, S. Cheval, C. Opera, M. Baciu, A. Dumitrescu, F. Iacobescu, I. Milos and C. Rada, "Computing global and diffuse solar hourly irradiation on clear sky. Review and testing of 54 models," *Renewable and Sustainable Energy Reviews,* vol. 16, no. 3, pp. 1636-1656, 2012.

[39] B. Jamil and N. Akhtar, "Comparison of empirical models to estimate monthly mean diffuse solar radiation from measured data: Case study for humid-subtropical climatic region of India,"

Renewable and Sustainable Energy Reviews, vol. 77, pp. 1326-1342, 2017.

[40] "National Solar Radiation Data Base," National Renewable Energy Laboratory, [Online]. Available: http://rredc.nrel.gov/solar/old_data/nsrdb/. [Accessed 1 Oct 2016].

[41] The Satel-Light Starter, "The European Database of Daylight and Solar Radiation," [Online]. Available: http://www.satel-light.com/core.htm. [Accessed 1 Mar 2019].

[42] Natural Resources Canada, "RETScreen," [Online]. Available: https://www.nrcan.gc.ca/energy/software-tools/7465. [Accessed 1 Mar 2019].

[43] Meteotest, "Meteonorm," [Online]. Available: https://meteotest.ch/en/product/meteonorm. [Accessed 1 Mar 2019].

[44] OpenSolarDB, "Extracting Solar data," [Online]. Available: http://www.opensolardb.org/db/extractcopypaste. [Accessed 1 Mar 2019].

[45] G. O. Löf, J. A. Duffie and C. O. Smith, "World distribution of solar radiation," *Solar Energy*, vol. 10, no. 1, pp. 27-37, 1966.

[46] N. R. E. Laboratory, "RE Atlas," [Online]. Available: https://maps.nrel.gov/re-atlas/. [Accessed 1 Oct 2016].

[47] SOLEMI, "Solar Energy Mining," [Online]. Available: https://www.dlr.de/tt/en/desktopdefault.aspx/tabid-2885/4422_read-6581/. [Accessed 1 Mar 2019].

[48] Solar Energy Laboratory, "TRNSYS 17: A transient system simulation program," University of Wisconsin, 2010.

[49] M. Danandeh, "Solar irradiance estimation models and optimum tilt angle approaches: A comparative study," *Renewable and Sustainable Energy Reviews,* vol. 92, pp. 319-330, 2018.

[50] J. Kern and I. Harris, "On the optimum tilt of a solar collector," *Solar Energy,* vol. 17, no. 2, pp. 97-102, 1975.

[51] H. Gunerhan and A. Hepbasli, "Determination of the optimum tilt angle of solar collectors for building applications," *Building and Environment,* vol. 42, no. 2, pp. 779-783, 2007.

[52] K. Ulgen, "Optimum tilt angle for solar collectors," *Energy Sources, Part A: Recovery, Utilization, and Environmental Effects,* vol. 28, no. 13, pp. 1171-1180, 2006.

[53] Y. Lv, P. Si, X. Rong, J. Yan, Y. Feng and X. Zhu, "Determination of optimum tilt angle and orientation for solar collectors based on effective solar heat collection," *Applied Energy,* vol. 219, pp. 11-19, 2018.

[54] M. Iqbal, An introduction to solar radiation, Academic Press, 1983.

[55] Y. Tian, R. Davies-Colley, P. Gong and B. Thorrold, "Estimating solar radiation on slopes of arbitrary aspect," *Agricultural and Forest Meteorology,* vol. 109, no. 1, pp. 67-74, Aug 2001.

[56] G. Paltridge and C. Platt, Radiative processes in meteorology and climatology, New York, NY: Elsevier, 1976.

[57] A. El-Sebaii, F. Al-Hazmi, A. Al-Ghamdi and S. Yaghmour, "Global, direct and diffuse solar radiation on horizontal and tilted surfaces in Jeddah, Saudi Arabia," *Applied Energy,* vol. 87, no. 2, pp. 568-576, 2010.

[58] B. Liu and R. Jordan, "Daily insolation on surfaces tilted towards equator," *ASHRAE Transactions,* vol. 67, p. 526–541, 1961.

[59] J. Rakovec and K. Zaksek, "On the proper analytical expression for the sky-view factor and the diffuse irradiation of a slope for an isotropic sky," *Renewable Energy,* vol. 37, no. 1, pp. 440-444, Jan 2012.

[60] N. Rehman and M. Uzair, "The proper interpretation of analytical sky view factors for isotropic diffuse solar irradiance on tilted planes," *Journal of Renewable and Sustainable Energy,* vol. 9, no. 5, p. 053702, 2017.

[61] A. G. Siraki and P. Pillay, "Study of optimum tilt angles for solar panels in different latitudes for urban applications," *Solar Energy,* vol. 86, no. 6, pp. 1920-1928, 2012.

[62] V. Badescu, "3D isotropic approximation for solar diffuse irradiance on tilted surfaces," *Renewable Energy,* vol. 26, no. 2, pp. 221-233, Jun 2002.

[63] E. Sakonidou, T. Karapantsios, A. Balouktsis and D. Chassapis, "Modeling of the optimum tilt of a solar chimney for maximum air flow," *Solar Energy,* vol. 82, no. 1, pp. 80-94, 2008.

[64] V. Badescu, "Optimal control of flow in solar collector systems with fully mixed water storage tanks," *Energy Conversion and Management,* vol. 49, no. 2, pp. 169-184, 2008.

[65] V. Badescu, "Optimum fin geometry in flat plate solar collector systems," *Energy Conversion and Management,* vol. 47, no. 15-16, pp. 2397-2413, 2006.

[66] S. Jeyaprabha and A. Selvakumar, "Optimal sizing of photovoltaic/battery/diesel based hybrid system and optimal tilting of solar array using the artificial intelligence for remote houses in India," *Energy and Buildings,* vol. 96, pp. 40-52, 2015.

[67] A. Noorian, I. Moradi and G. Kamali, "Evaluation of 12 models to estimate hourly diffuse irradiation on inclined surfaces," *Renewable energy,* vol. 33, no. 6, pp. 1406-1412, 2008.

[68] C. Pandey and A. Katiyar, "A note on diffuse solar radiation on a tilted surface," *Energy,* vol. 34, no. 11, pp. 1764-1769, 2009.

[69] C. Pandey and A. Katiyar, "A comparative study of solar irradiation models on various inclined surfaces for India," *Applied energy,* vol. 88, no. 4, pp. 1455-1459, 2011.

[70] R. A. e Silva, J. M. Baptista and M. C. Brito, "Data-driven estimation of expected photovoltaic generation," *Solar Energy,* vol. 166, pp. 116-122, 2018.

[71] J. J. Roberts, A. A. M. Zevallos and A. M. Cassula, "Assessment of photovoltaic performance models for system simulation," *Renewable and Sustainable Energy Reviews,* vol. 72, pp. 1104-1123, 2017.

[72] Y. Xie, M. Sengupta and M. Dooraghi, "Assessment of uncertainty in the numerical simulation of solar irradiance over inclined PV panels: New algorithms using measurements and modeling tools," *Solar Energy,* vol. 165, pp. 55-64, 2018.

[73] N. Kamphuis, C. Gueymard, M. Holtzapple, A. Duggleby and K. Annamalai, "Perspectives on the origin, derivation, meaning, and significance of the isotropic sky model," *Solar Energy,* vol. 201, pp. 8-12, 2020.

[74] C. Demain, M. Journée and C. Bertrand, "Evaluation of different models to estimate the global solar radiation on inclined surfaces," *Renewable Energy,* vol. 50, pp. 710-72, 2013.

[75] J. E. Hay, "Calculation of monthly mean solar radiation for horizontal and inclined surfaces," *Solar Energy,* vol. 23, no. 4, pp. 301-307, 1979.

[76] J. E. Hay and J. A. Davies, "Calculation of the solar radiation incident on an inclined surface," in *1st Canadian Solar Radiation Data Workshop, Ministry of Supply and Services*, Canada, 1980.

[77] D. T. Reindl, W. A. Beckman and J. A. Duffie, "Evaluation of hourly tilted surface radiation models," *Solar Energy,* vol. 45, no. 1, pp. 9-17, 1990.

[78] R. Perez, R. Stewart, C. Arbogast, R. Seals and J. Scott, "An anisotropic hourly diffuse radiation model for sloping surfaces: description, performance validation, site dependency evaluation," *Solar Energy,* vol. 36, no. 6, pp. 481-497, 1986.

[79] A. Brunger and F. Hooper, "Anisotropic sky radiance model based on narrow field of view measurements of shortwave radiance," *Solar Energy,* vol. 51, no. 1, pp. 53-64, 1993.

[80] P. Fu and P. Rich, "Design and implementation of the Solar Analyst: an ArcView extension for modeling solar radiation at landscape scales," in *19th annual ESRI user conference*, San Diego ,USA, 1999.

[81] J. Buffo, L. Fritschen and J. Murphy, "Direct solar radiation on various slopes from 0 to 60 degrees north latitude," Res. Pap. PNW-RP-142. Portland, OR: US Department of Agriculture, Forest Service, Pacific Northwest Research Station, 1972.

[82] E. Frank and R. Lee, "Potential solar beam irradiation on slopes: Tables for 30 degrees to 50 degrees," U. S. Forest Services Rocky Mountain Forest Range Experimental Station Paper RM-18, 1966.

[83] K. Kondratyev, Radiation in the Atmosphere, New York, NY: Academic Press, 1969.

[84] L. Swift Jr, "Algorithm for solar radiation on mountain slopes," *Water Resources Research,* vol. 12, no. 1, pp. 108-112, 1976.

[85] A. Flint and S. Childs, "Calculation of solar radiation in mountainous terrain," *Agricultural and Forest Meteorology,* vol. 40, no. 3, pp. 233-249, 1987.

[86] P. Rich, "A manual for analysis of hemispherical canopy photography (No. LA-11733-M)," Los Alamos National Lab, USA, 1989.

[87] P. Rich, "Characterizing plant canopies with hemispherical photographs," *Remote Sensing Reviews,* vol. 5, no. 1, pp. 13-29, 1990.

[88] P. Rich, J. Wood, D. Vieglais, K. Burek and N. Webb, "Guide to HemiView: software for analysis of hemispherical photography," Delta-T Devices, Ltd. Cambridge, England, 1999.

[89] W. Hetrick, P. Rich, F. Barnes and S. Weiss, "GIS-based solar radiation flux models," in *ACSM ASPRS ANNUAL CONVENTION*, 1993.

[90] W. Hetrick, P. Rich and S. Weiss, "Modeling insolation on complex surfaces," in *13th Annual ESRI User Conference*.

[91] R. Dubayah and M. Rich, "Topographic solar radiation models for GIS," *International Journal of Geographic Information Systems,* vol. 9, pp. 405-413, 1995.

[92] L. Kumar, A. Skidmore and E. Knowles, "Modelling topographic variation in solar radiation in a GIS environment," *International Journal of Geographical Information Science,* vol. 11, no. 5, pp. 475-497, 1997.

[93] K. Zakšek, K. Oštir and Ž. Kokalj, "Sky-View Factor as a Relief Visualization Technique," *Remote Sensing,* vol. 3, no. 12, pp. 398-415, 2011.

[94] J. Bosch, F. Batlles, L. Zarzalejo and G. López, "Solar resources estimation combining digital terrain models and satellite images techniques," *Renewable Energy,* vol. 35, no. 12, pp. 2853-2861, 2010.

[95] J. Polo and R. Perez, "Solar Radiation Modeling from Satellite Imagery," in *Solar Resources Mapping: Fundamentals and applications,* L Polo. L. Martin-Pomares and A, Sanfilippo ed., Cham, Springer, 2019, pp. 183-197.

[96] C. Hirt, "Digital terrain models," *Encyclopedia of Geodesy,* pp. 1-6, 2014.

[97] N. Haala, M. Rothermel and S. Cavegn, "Extracting 3D urban models from oblique aerial images," in *2015 Joint Urban Remote Sensing Event,* 2015.

[98] Z. Li, Q. Zhu and C. Gold, Digital terrain modeling: Principles and methodology, New York,

NY: CRC Press, 2005.

[99] R. F., "Do You Know LiDAR and IfSAR," [Online]. Available: https://fatwaramdani.wordpress.com/2008/12/02/do-you-know-lidar-and-ifsar/. [Accessed 1 Mar 2019].

[100] J. Hofierka and M. Suri, "The solar radiation model for Open source GIS: implementation and applications," in *Proceedings of the Open source GIS-GRASS users conference*, Trento, Italy, 2002.

[101] W. Solecki, C. Rosenzweig, S. Dhakal, D. Roberts, A. Barau, S. Schultz and D. Ürge-Vorsatz, "City transformations in a 1.5 C warmer world. Nature Climate Change," *Nature Climate Change,* vol. 8, no. 3, pp. 177-180, 2018.

[102] B. Mattoni, F. Pagliaro, L. Gugliermetti, F. Bisegna and L. Cellucci, "A territorial based strategy for the distribution of sensor networks in smart cities," in *IEEE 15th International Conference on Environment and Electrical Engineering (EEEIC)*, 2015.

[103] D. Groppi, L. de Santoli, F. Cumo and D. Garcia, "A GIS-based model to assess buildings energy consumption and usable solar energy potential in urban areas," *Sustainable Cities and Society,* vol. 40, pp. 546-558, 2018.

[104] A. Lepik and C. Shuttleworth, Skyscrapers, New York, NY: Prestel, 2004.

[105] X. Zhai, R. Wang, Y. Dai, J. Wu and Q. Ma, "Experience on integration of solar thermal technologies with green buildings," *Renewable Energy,* vol. 33, no. 8, pp. 1904-1910, 2008.

[106] H. Curtius, "The adoption of building-integrated photovoltaics: barriers and facilitators," *Renewable Energy,* vol. 126, pp. 783-790, 2018.

[107] C. Lamnatou, J. Mondol, D. Chemisana and C. Maurer, "Modelling and simulation of Building-Integrated solar thermal systems: Behaviour of the coupled building/system configuration," *Renewable and Sustainable Energy Reviews,* vol. 48, pp. 178-191, 2015.

[108] Y. Lu, X. Zhang, Z. Huang, J. Lu and C. Wang, "Definition and Design of Zero Energy Buildings," in *Green Energy Advances,* E. Enescu ed., London, Uk, IntechOpen, 2019.

[109] U. Stritih, V. Tyagi, R. Stropnik, H. Paksoy, F. Haghighat and M. Joybari, "Integration of passive PCM technologies for net-zero energy buildings," *Sustainable cities and society,* vol. 41, pp. 286-295, 2018.

[110] J. Lizana, R. Chacartegui, A. Barrios-Padura and J. Valverde, "Advances in thermal energy storage materials and their applications towards zero energy buildings: a critical review," *Applied Energy,* vol. 203, pp. 219-239, 2017.

[111] C. Hachem, A. Athienitis and P. Fazio, "Energy performance enhancement in multistory residential buildings," *Applied Energy,* vol. 16, pp. 9-19, 2014.

[112] S. Kesler, H. G. S. Kivrak, F. Dincer, S. Yilmaz and H. R. Ozcalik, "A Low Cost Shading Analyzer and Site Evaluator Design to Determine Solar Power System Installation Area," *International Journal of Photoenergy,* vol. 2015, p. Article ID 126373, 2015.

[113] Solar Pathfinder, "Solar Pathfinder," [Online]. Available: http://www.solarpathfinder.com/PF. [Accessed 1 Mar 2019].

[114] R. Perez, B. Schultze and J. Pryor, "Things that work: home power tests the solar pathfinder," *Home Power Magazine,* vol. 16, pp. 44-45, 1990.

[115] M. Dennis, "Automated solar shading analysis," in *ISES Solar World Congress 2003: Solar Energy for a Sustainable Future,* Göteborg, Sweden, 2003.

[116] S. Wakter and F. Wikerman, "A novel shade analysis technique for solar photovoltaic systems," KTH School of Industrial Engineering and Management, 2014.

[117] Derekr Corporation, "AngleCam Lite - Angular Camera - Android Apps on Google Play," [Online]. Available: https://play.google.com/store/apps/details?id=com.derekr.AngleCam&hl=en. [Accessed 1 Mar 2019].

[118] Y-Design, "Camera Angle on the App Store," [Online]. Available: https://itunes.apple.com/us/app/camera-angle/id701650924?mt=8. [Accessed 2019].

[119] C. Cleveland and C. Morris, "Vol 1: Diagrams, Charts and Tables," in *Handbook of Energy,* New York, NY, Elsevier, 2013.

[120] E. Melo, M. Almeida, R. Zilles and J. Grimoni, "Using a shading matrix to estimate the shading factor and the irradiation in a three-dimensional model of a receiving surface in an urban environment," *Solar Energy,* vol. 92, pp. 15-25, 2013.

[121] V. Quaschning and R. Hanitsch, "Irradiance calculation on shaded surfaces," *Solar Energy,* vol. 62, no. 5, pp. 369-375, 1998.

[122] S. Ivanova, "Estimation of solar radiation for buildings with complex architectural layouts," in *5th International Conference Solaris*, Czech Republic, 2011.

[123] S. Ivanova, "Estimation of background diffuse irradiance on orthogonal surfaces under partially obstructed anisotropic sky. Part II–Horizontal surfaces," *Solar Energy,* vol. 100, pp. 234-250, 2014.

[124] S. Ivanova, "Estimation of background diffuse irradiance on orthogonal surfaces under partially obstructed anisotropic sky: Part I–Vertical surfaces," *Solar Energy,* vol. 95, pp. 376-391, 2013.

[125] D. Robinson and A. Stone, "Solar radiation modelling in the urban context," *Solar Energy,* vol. 77, no. 3, pp. 295-309, 2004.

[126] A. Roberts and A. Marsh, "ECOTECT: environmental prediction in architectural education," in *19th eCAADe Conference*, Helsinki, Finland, 2001.

[127] J. Kämpf and D. Robinson, "Optimisation of building form for solar energy utilisation using constrained evolutionary algorithms," *Energy and Buildings*, vol. 42, no. 6, pp. 807-814, 2010.

[128] P. R. Tregenza and S. Sharples, "New daylight algorithms," 1995. [Online]. Available: http://naturalfrequency.com/Tregenza_Sharples/Daylight_Algorithms/intro.htm. [Accessed 1 May 2017].

[129] S. Ivanova and C. Gueymard, "Simulation and applications of cumulative anisotropic sky radiance patterns," *Solar Energy*, vol. 178, pp. 278-294, 2019.

[130] N. Rehman and M. Siddiqui, "A novel method for determining sky view factor for isotropic diffuse radiations for a collector in obstacles-free or urban sites," *Journal of Renewable and*

Sustainable Energy, vol. 7, no. 3, p. 033110, 2015.

[131] C. Carneiro, E. Morello, G. Desthieux, F. Golay and others, "Urban environment quality indicators: application to solar radiation and morphological analysis on built area," in *Proceedings of the 3rd WSEAS international conference on Visualization, imaging and simulation*, 2010.

[132] MathWorks, "MATLAB and Simulink," [Online]. Available: https://www.mathworks.com/products/matlab.html. [Accessed 1 10 2019].

[133] J. Hofierka, "Direct solar radiation modelling within an open GIS environment," in *Proceedings of JEC-GI'97 conference, IOS Press Amsterdam*, Vienna, Austria, 1997.

[134] S. Tabik, A. Villegas, E. Zapata and L. Romero, "A fast GIS-tool to compute the maximum solar energy on very large terrains," *Procedia Computer Science*, vol. 9, pp. 364-372, 2012.

[135] J. A. Jakubiec and C. F. Reinhart, "A method for predicting city-wide electricity gains from photovoltaic panels based on LiDAR and GIS data combined with hourly Daysim simulations," *Solar Energy*, vol. 93, pp. 127-143, Jul 2013.

[136] R. Perez, R. Seals and J. Michalsky, "All-weather model for sky luminance distribution—preliminary configuration and validation," *Solar Energy*, vol. 50, no. 3, pp. 235-245, 1993.

[137] G. J. Ward, "The RADIANCE lighting simulation and rendering system," in *94 SIGGRAPH Conference*, Orlando, Florida, 1994.

[138] P. Redweik, C. Catita and M. Brito, "Solar energy potential on roofs and facades in an urban

landscape," *Solar Energy*, vol. 97, pp. 332-341, Nov 2013.

[139] J. Liang, J. Gong, J. Zhou, A. Ibrahim and M. Li, "An open-source 3D solar radiation model integrated with a 3D Geographic Information System," *Environmental Modelling & Software*, vol. 64, pp. 94-101, 2015.

[140] D. Lingfors, S. Killinger, N. Engerer, J. Widén and J. Bright, "Identification of PV system shading using a LiDAR-based solar resource assessment model: An evaluation and cross-validation," *Solar Energy*, vol. 159, pp. 157-172, 2018.

[141] G. Desthieux, C. Carneiro, R. Camponovo, P. Ineichen, E. Morello, A. Boulmier, N. Abdennadher, S. Dervey and C. Ellert, "Solar Energy Potential Assessment on Rooftops and Facades in Large Built Environments Based on LiDAR Data, Image Processing, and Cloud Computing. Methodological Background, Application, and Validation in Geneva (Solar Cadaster)," *Frontiers in Built Environment*, vol. 4, p. 14, 2018.

[142] M. Oh and H. Park, "A new algorithm using a pyramid dataset for calculating shadowing in solar potential mapping," *Renewable Energy*, vol. 126, pp. 465-474, 2018.

[143] M. Kapoor and R. Garg, "Cloud computing for energy requirement and solar potential assessment," *Spatial Information Research*, vol. 26, no. 4, pp. 369-379, 2018.

[144] G. Quesada, D. Rousse, Y. Dutil, M. Badache and S. Hallé, "A comprehensive review of solar facades. Opaque solar facades," *Renewable and Sustainable Energy Reviews*, vol. 16, no. 5, pp. 2820-2832, 2012.

[145] C. Schill, S. Brachmann and M. Koehl, "Impact of soiling on IV-curves and efficiency of PV-

modules," *Solar Energy*, vol. 112, pp. 259-262, 2015.

[146] C. Hsieh, Y. Chen, H. Tan and P. Lo, "Potential for installing photovoltaic systems on vertical and horizontal building surfaces in urban areas," *Solar Energy*, vol. 93, pp. 312-321, 2013.

[147] M. Hummon, P. Denholm and R. Margolis, "Impact of photovoltaic orientation on its relative economic value in wholesale energy markets," *Progress in Photovoltaics: Research and Applications*, vol. 21, no. 7, pp. 1531-1540, 2013.

[148] G. Lobaccaro and F. Frontini, "Solar energy in urban environment: how urban densification affects existing buildings.," *Energy Procedia*, vol. 48, pp. 1559-1569, 2014.

[149] M. Probst and C. Roecker, "Criteria for architectural integration of active solar systems IEA Task 41, Subtask A," *Energy Procedia*, vol. 30, pp. 1195-1204, 2012.

[150] D. Attoye, T. Adekunle, K. Tabet Aoul, A. Hassan and S. Attoye, "A conceptual framework for a building integrated photovoltaics (BIPV) educative-communication approach.," *Sustainability*, vol. 10, no. 10, p. 3781, 2018.

[151] C. Koo, T. Hong, H. Park and G. Yun, "Framework for the analysis of the potential of the rooftop photovoltaic system to achieve the net-zero energy solar buildings," *Progress in Photovoltaics: Research and Applications*, vol. 22, no. 4, pp. 462-478, 2014.

[152] P. Littlefair, "Passive solar urban design: ensuring the penetration of solar energy into the city," *Renewable and Sustainable Energy Reviews*, vol. 2, no. 3, pp. 303-326, 1998.

[153] S. Freitas, C. Catita, P. Redweik and M. Brito, "Modelling solar potential in the urban environment: State-of-the-art review," *Renewable and Sustainable Energy Reviews*, vol. 41,

pp. 915-931, Jan 2015.

[154] J. Ruiz-Arias, J. Tovar-Pescador, D. Pozo-Vázquez and H. Alsamamra, "A comparative analysis of DEM-based models to estimate the solar radiation in mountainous terrain," *International Journal of Geographical Information Science,* vol. 23, no. 8, pp. 1049-1076, 2009.

[155] Ž. Kokalj, K. Zakšek and K. Oštir, "Application of sky-view factor for the visualisation of historic landscape features in lidar-derived relief models," *Antiquity,* vol. 85, no. 327, pp. 263-273, 2011.

[156] J. de Boer, "Modelling indoor illumination by complex fenestration systems based on bidirectional photometric data," *Energy and Buildings,* vol. 38, no. 7, pp. 849-868, 2006.

[157] B. Semlitsch, "Advanced Ray Tracing Techniques for Simulation of Thermal Radiation in Fluids," Institut für Strömungsmechanik und Wärmeübertragung, Wien, Austria, 2010.

[158] Google, "Google SketchUp - 3D modeling for everyone," [Online]. Available: https://www.sketchup.com/. [Accessed 28 May 2018].

[159] A. B. Bondi, "Characteristics of scalability and their impact on performance," in *2nd international Workshop on Software and Performance*, Ottawa, ON, 2000.

[160] W. F. McColl, "Scalable computing," in *Computer Science Today*, Berlin, Heidelberg, Springer, 1995, pp. 46-61.

[161] M. Michael, J. Moreira, D. Shiloach and R. Wisniewski, "Scale-up x scale-out: A case study using nutch/lucene," in *IEEE International Parallel and Distributed Processing Symposium*,

2007.

[162] "Amazon Web Services (AWS)," [Online]. Available: https://aws.amazon.com/. [Accessed 1 Mar 2019].

[163] "Google Cloud Platform," [Online]. Available: https://cloud.google.com/. [Accessed 1 Mar 2019].

[164] "Microsoft Azure," [Online]. Available: https://azure.microsoft.com/. [Accessed 1 Mar 2019].

[165] "Amazon EC2," [Online]. Available: https://aws.amazon.com/ec2/. [Accessed 1 Mar 2019].

[166] "EC2Instances.info Easy Amazon EC2 Instance Comparison," [Online]. Available: https://www.ec2instances.info/. [Accessed 1 Mar 2019].

[167] "Amazon EC2 Instance Types," [Online]. Available: https://aws.amazon.com/ec2/instance-types/. [Accessed 1 Mar 2019].

[168] "Amazon EC2 Pricing," [Online]. Available: https://aws.amazon.com/ec2/pricing/. [Accessed 1 Mar 2019].

[169] sqa.org.uk, "File Locking," [Online]. Available: https://www.sqa.org.uk/e-learning/COS101CD/page_10.htm. [Accessed 1 Mar 2019].

[170] Auckland University of Technology, "City Campus," [Online]. Available: https://www.aut.ac.nz/about/campuses-and-locations/city-campus?nav=inthissection. [Accessed 1 Mar 2019].

[171] OpenStreetMap, "AUT city campus," [Online]. Available: https://www.openstreetmap.org/#map=17/-36.85386/174.76646. [Accessed 1 Mar 2019].

[172] V. Cheng, K. Steemers, M. Montavon and R. Compagnon, "Urban form, density and solar potential," in *The 23rd Conference on Passive and Low Energy Architecture*, Geneva, Switzerland, 2006.

[173] R. Compagnon, "Solar and daylight availability in the urban fabric," *Energy and Buildings,* vol. 36, no. 4, pp. 321-328, 2004.

[174] R. Machete, A. Falcão, M. Gomes and A. Rodrigues, "The use of 3D GIS to analyse the influence of urban context on buildings' solar energy potential," *Energy and Buildings,* vol. 177, pp. 290-302, 2018.

[175] D. Robinson and A. Stone, "A simplified radiosity algorithm for general urban radiation exchange," *Building Services Engineering Research and Technology,* vol. 26, no. 4, pp. 271-284, 2005.

[176] M. Fogl and V. Moudrý, "Influence of vegetation canopies on solar potential in urban environments," *Applied Geography,* vol. 66, pp. 73-80, 2016.

[177] L. French, M. Camilleri, N. Isaacs and A. Pollard, "Winter temperatures in New Zealand houses," in *Proc. Comfort and Energy Use in Buildings–Getting them Right*, 2006.

[178] M. Montavon, J. Scartezzini and R. Compagnon, "Solar energy utilisation potential of three different Swiss urban sites," in *Energie und Umweltforschung im Bauwesen*, Zurich, 2004.

[179] D. Chemisana, J. Lopez-Villada, A. Coronas, J. Rosell and C. Lodi, "Building integration of concentrating systems for solar cooling applications," *Applied Thermal Engineering*, vol. 50, no. 2, pp. 1472-1479, 2013.

[180] G. Quesada, D. Rousse, Y. Dutil, M. Badache and S. Hallé, "A comprehensive review of solar facades. Opaque solar facades," *Renewable and Sustainable Energy Reviews*, vol. 16, no. 5, pp. 2820-2832, 2012.

[181] G. Quesada, D. Rousse, Y. Dutil, M. Badache and S. Hallé, "A comprehensive review of solar facades. Transparent and translucent solar facades.," *Renewable and Sustainable Energy Reviews*, vol. 16, no. 5, pp. 2643-2651, 2012.

[182] L. C., R. A. and S. A., "Types of Ray Tracing," 1997 Sophomore College Ray Tracing Site, [Online]. Available: https://cs.stanford.edu/people/eroberts/courses/soco/projects/1997-98/ray-tracing/types.html. [Accessed 1 Mar 2019].

[183] ESRI, "Esri Products," [Online]. Available: https://www.esri.com/en-us/arcgis/products/index. [Accessed 1 Mar 2019].

[184] QGIS, "QGIS," [Online]. Available: https://www.qgis.org/en/site/. [Accessed 1 Mar 2019].

[185] GRASS GIS, "GRASS GIS," [Online]. Available: https://grass.osgeo.org/. [Accessed 1 Mar 2019].

[186] Y. A. Cengel, Heat Transfer: A Practical Approach., New York, NY: McGraw-Hill Higher Education, 2002.

[187] T. L. Bergman and F. P. Incropera, Introduction to heat transfer, Hoboken, NJ: John Wiley and Sons, 2011.

[188] J. R. Howell, M. P. Menguc and R. Siegel, Thermal radiation heat transfer., Boca Raton, FL: CRC Press, 2010.

[189] F. Lindberg, P. Jonsson, T. Honjo and D. Wästberg, "Solar energy on building envelopes–3D modelling in a 2D environment," *Solar Energy*, vol. 115, pp. 369-378, 2015.

[190] Land Information New Zealand, "LINZ Data Service," [Online]. Available: https://www.linz.govt.nz/about-linz. [Accessed 1 Mar 2019].

[191] Land Information New Zealand, "Auckland Lidar 1m DEM (2013)," [Online]. Available: https://data.linz.govt.nz/layer/53405-auckland-lidar-1m-dem-2013/. [Accessed 1 Mar 2019].

[192] Land Information New Zealand, "Auckland Lidar 1m DSM (2013)," [Online]. Available: https://data.linz.govt.nz/layer/53406-auckland-lidar-1m-dsm-2013/. [Accessed 1 Mar 2019].

[193] Land Information New Zealand, "New Zealand Vertical Datum 2009 (NZVD2009)," [Online]. Available: https://www.linz.govt.nz/data/geodetic-system/datums-projections-and-heights/vertical-datums/new-zealand-vertical-datum-2009-nzvd2009. [Accessed 1 Mar 2019].

[194] Koordinates, "Raster query," [Online]. Available: https://help.koordinates.com/api/query-api/raster-query/. [Accessed 1 Mar 2019].

[195] D. Crockford, "Introducing JSON," [Online]. Available: https://www.json.org/. [Accessed 1 Mar 2019].

[196] Google Maps, "ANZ Centre, 23 Albert St, Auckland, New Zealand (1010)," [Online]. Available: https://www.google.com/maps/place/36°50'44.5"S+174°45'51.8"E/@-36.8456944,174.7622002. [Accessed 1 Mar 2019].

[197] SkyscraperPage.com, "Drawings of ANZ Centre," [Online]. Available: http://skyscraperpage.com/diagrams/?buildingID=975. [Accessed 1 Mar 2019].

[198] OpenStreetMap, "About OpenStreetMap," [Online]. Available: https://www.openstreetmap.org/about. [Accessed 1 Mar 2019].

[199] w3.org, "Extensible Markup Language (XML)," [Online]. Available: https://www.w3.org/XML/. [Accessed 1 Mar 2019].

[200] C. Clapham and J. Nicholson, "Oxford Concise Dictionary of Mathematics," [Online]. Available: https://web.archive.org/web/20131029203826/http://web.cortland.edu/matresearch/OxfordDictionaryMathematics.pdf. [Accessed 1 Mar 2019].